NONLINEAR FREQUENCY CONVERSION OF A CONTINUOUS-WAVE, LASER DIODE-PUMPED ND:YLF LASER

Jun Zhang

A Thesis Submitted for the Degree of PhD
at the
University of St Andrews

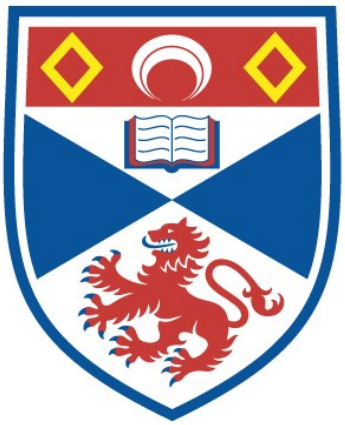

1996

Nonlinear Frequency Conversion of a Continuous-Wave, Laser Diode-Pumped Nd:YLF Laser

Thesis submitted for the degree of Doctor of Philosophy

to the University of St. Andrews

by

Jun ZHANG, B.Sc.

The J. F. Allen Physics Research Laboratories
Department of Physics and Astronomy
University of St. Andrews
St. Andrews
Fife KY16 9SS
Scotland, United Kingdom

September 1995

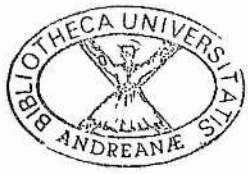

Declaration

I, Jun Zhang, hereby certify that this thesis has been composed by myself, that it is a record of my own work and that it has not been accepted in partial or complete fulfilment of any other degree or professional qualification.

I was admitted to the Faculty of Science of the University of St. Andrews as a candidate for the degree of Ph.D under the General Ordinance No. 12 on 1st October, 1991.

Signed

Jun Zhang

September 1995

Certificate

I hereby certify that the candidate has fulfilled the conditions of the Resolution and Regulations appropriate to the Degree of Ph.D.

M. H. Dunn

Signature of Supervisor

September 1995

Copyright

In submitting this thesis to the University of St. Andrews I understand that I am giving the permission for it to be made available for use in accordance with the regulations of the University Library for the time being in force, subject to any copyright vested in the work not being affected thereby. I also understand that the title and abstract will be published, and that a copy of the work may be made and supplied to any bona fide library or research worker.

Acknowledgements

I would like to thank my supervisor, Professor Malcolm Dunn, for giving me the opportunity, encouragement, support, and patient help throughout the course of this work.

I am indebted to Dr. Bruce Sinclair for his helpful suggestions and infectious enthusiasm for physics, Dr. Angus Henderson for his expertise in CW OPO works, Cameron Rae for the advice in development of all-solid-state lasers. The useful discussion with Dr. Jun-hua Hong, Dr. Finally Colville, Dr. Miles Padgett during my study has been invaluable. Also, I would like to thank Dr. Majid Ebrahimzadeh, Dr. Miles Padgett, and Dr. David Burns for their proof reading of this thesis.

The assistance of the technical support staff in the mechanical workshop and electronics workshop is greatly appreciated with special thanks going to Mr. Jim Clark and Mr. Jimmy Lindsay for manufacturing optics mounts.

I am grateful to the University of St. Andrews for the postgraduate studentship and the Oversea Research Student Award.

Finally, I owe a great debt of gratitude to my wife for the support, encouragement she provided during the days in St. Andrews.

Abstract

A continuous-wave, frequency-doubled, diode-pumped Nd:YLF laser, capable of generating 1-W of single-frequency radiation at 523.5 nm, with a linewidth of 10 kHz and frequency tunability of 9 GHz has been developed. By using the tunable green laser as pump source, 4.5 GHz continuous smooth tuning in the range of 1020 - 1070 nm has been demonstrated in a low threshold doubly-resonant optical parametric oscillator.

The investigation of thermal effect in the end-pump Nd:YLF laser crystal and the consideration of diode array end-pump geometry have led to an optimum folded-cavity design. Such an optical resonator can eliminate the astigmatism in the laser output, which is induced by the cavity folding on a curved mirror and the anisotropic thermal effect in Nd:YLF, resulting in a circular fundamental laser mode. In addition, a tightly focused beam waist is produced inside the cavity so that efficient intracavity SHG can be achieved. Over 30% optical conversion efficiency from diode to TEM_{oo} 1047 nm laser output and 10% conversion efficiency from diode to single-frequency SHG green radiation has been demonstrated. A novel intracavity birefringent filter frequency selection technique has been applied in the standing-wave laser resonator to achieve the single-frequency operation. The performances of the laser in the fundamental wave and in second harmonic generation are investigated in detail in this thesis.

The tuning behaviour and stability requirements of type-I and type-II CW doubly-resonant OPO have been compared by using the above green laser as the pump source and LBO, KTP as nonlinear crystals. Through utilisation of a simple cavity length servo, type-II phase matching allows single signal-idler mode-pair operation. By means of pump frequency tuning, and cavity length servo control, the output of signal and idler frequency can be tuned continuously over the KTP crystal phase-matching range.

Theoretical analyses on diode-end-pumped Nd:YLF lasers, intracavity frequency doubling, the novel intracavity birefringent filter, and the tuning behaviour and stability requirements of single cavity DRO are also presented in this work.

Contents

Chapter 1

INTRODUCTION

1.1 Background

Nonlinear frequency conversion techniques such as harmonic generation and parametric oscillation provide a means of extending the frequency of available laser sources. Harmonic generators are widely used to provide a single harmonic from a given fundamental source. Optical parametric oscillators (OPOs) can generate two waves of lower frequency from a single-frequency pump laser, and they are capable of providing coherent radiation with potentially very large and truly continuous tuning ranges.

Unlike efficient harmonic generators, the development of continuous-wave OPOs has long been hampered by the lack of desired nonlinear materials and laser sources due to either the over-constrained single-mode-pair operating condition in doubly resonant optical parametric oscillators (DROs) or the substantially high pump power requirement for singly resonant optical parametric oscillators (SROs). The recent improvements in crystal quality, laser sources, and cavity designs have overcome some of the technical difficulties of stabilising and tuning CW OPOs. Continuous-wave operation with tunable single-mode-pair output has been demonstrated in both low-threshold DRO [1] and high-threshold SRO [2]. These developments are enabling CW OPOs to live up to their decades-old promise of efficient, narrow-linewidth, and widely tunable light source.

The use of single-frequency diode-pumped solid-state lasers (DPSSLs) as a CW OPO pump source can also be considered as reproducing the frequency stability of DPSSLs in a tunable output. Due to the fact that DPSSLs are capable of providing the required pump frequency stability for doubly resonant OPO, which is almost always used in continuous-wave operation, the complexity of stability and tuning behaviour of DROs are greatly reduced. Thus, single-mode-pair oscillation, with potential large

tunability, can be easily achieved in low threshold DROs. In addition, diode-pumped solid-state lasers are efficient, compact source of coherent radiation with a high degree of beam quality. They can be efficiently frequency-converted into the green or ultraviolet (UV) spectrum by harmonic generation. The combination of DPSSL and OPO can result in an all-solid-state widely tunable coherent light source.

The generation of continuous-wave, widely tunable, highly coherent optical radiation from all-solid-state OPOs is of great interest for applications of high-resolution laser spectroscopy [3] and optical frequency division [4]. These applications take advantage of unique properties of all-solid-state CW OPOs. Typically, OPO devices reproduce the frequency stability of the pump source in the tunable output. The narrow linewidth radiation with a continuous frequency tuning ability can provide a high-resolution optical measurement. On the other hand, the wide tuning range of many OPOs opens up prospects for laser spectroscopy in otherwise inaccessible spectral region, such as the near and mid-infrared. As for the application of optical frequency division, since a correlated frequency chain can be set up through a series of efficient nonlinear frequency conversions (including SHG and OPO process), it is possible to measure, compare, and synthesise optical frequencies with precision and accuracy.

1.2 Parametric Frequency Conversion Processes

The fundamental physics of three-wave light interaction in nonlinear optical crystal is now largely understood. The origin of this optical nonlinear process is the nonlinear response of optical material to the propagating optical electric field. In this section, we briefly introduce the principle of frequency conversion processes of second-harmonic generation and optical parametric oscillation.

A. Three-Wave Nonlinear Interaction

In any real atomic system, polarisation induced in the medium is not proportional to the optical electric field, but can be expressed as

$$P = \varepsilon_o(\chi^{(1)}E + \chi^{(2)}E^2 + \chi^{(3)}E^3 + \ldots..) \qquad (1.1)$$

where ε_o is the permittivity of free space; $\chi^{(1)}$, $\chi^{(2)}$, $\chi^{(3)}$ refer to the linear susceptibility, second-, and third-order nonlinear optical susceptibility, which describe the linear, quadratic, and cubic dependence of the polarisation on the applied field, respectively. The second-order nonlinearity $P = \varepsilon_o\chi^{(2)}E^2$ is responsible for second-harmonic generation, sum- and difference-frequency generation, and parametric amplification and oscillation. These second-order effects are primarily parametric processes in nature. Considering the nonlinear coupling of two optical fields at frequencies ω_1 and ω_2, the presence of these two frequency components can give rise to nonlinear polarisation (in the $\chi^{(2)}$ dominant regime) at frequencies $n\omega_1 \pm m\omega_2$, where $n(\text{or } m) = 0, 1$. These non-zero frequency components describe the SHG, the sum-frequency generation, and the difference-frequency generation. The above processes take place simultaneously in the nonlinear medium with their potential parametric gain. However, in actual nonlinear interaction, phase-matching selects the process of interest to the exclusion of other possible processes.

The second-order nonlinear susceptibility predominately relates second-order effects with the applied optical electric fields. It is expressed as a third-rank tensor which generally has 27 components. As a result of crystal symmetry, many of the components of $\chi^{(2)}$ will be zero or equal to other components of the tensor. An immediate consequence is that the nonlinear polarisation tensor $\chi^{(2)}$ vanish in crystals that have a centre of symmetry. In addition to the crystal symmetry restriction, two symmetry conditions have to apply to $\chi^{(2)}$ in the nonlinear interaction process. The first is an intrinsic symmetry relation which can be derived for a lossless medium from general energy conservation considerations. The second symmetry relation is based on a conjecture by Kleinman [5] that in a lossless medium the permutation of the frequencies is irrelevant and therefore $\chi^{(2)}$ is symmetric under any permutation of its indices. In

practice, the nonlinear coefficient tensor d_{ijk} is used instead of tensor $\chi^{(2)}$, the two tensors being interrelated by the equation

$$\chi_{ijk}^{(2)} = 2d_{ijk} \tag{1.2}$$

The d_{ijk} coefficients of particular nonlinear crystal are measured most often in second-harmonic generation experiments. Applying the contracted notation $d_{i(jk)} = d_{in}$, the resulting d_{in} components form a 3 x 6 matrix that operates on the E^2 column tensor to yield P according to

$$\begin{bmatrix} P_x \\ P_y \\ P_z \end{bmatrix} = 2 \cdot \begin{bmatrix} d_{11} & d_{12} & d_{13} & d_{14} & d_{15} & d_{16} \\ d_{21} & d_{22} & d_{23} & d_{24} & d_{25} & d_{26} \\ d_{31} & d_{32} & d_{33} & d_{34} & d_{35} & d_{36} \end{bmatrix} \cdot \begin{bmatrix} E_x^2 \\ E_y^2 \\ E_z^2 \\ 2E_zE_y \\ 2E_zE_x \\ 2E_xE_y \end{bmatrix} \tag{1.3}$$

The effective nonlinearity coefficients d_{eff} is a measure of the coupling between the three fields that a wave of a given polarisation and propagation direction will experience on travelling through a material in the presence of two other intense fields. Once the crystal class, the non-zero nonlinear coefficients, and the geometry are known, the value of d_{eff} can be calculated. It is an important parameter for evaluating the efficiency of the nonlinear process and choosing propagating direction.

Equations that describe three electromagnetic field interaction via nonlinear driving polarisation are derived by Yariv [6], Armstrong *et al.* [7], and Smith [8]. These are:

$$\begin{aligned} \frac{dE_1}{dz} + \alpha_1 E &= j\kappa_1 \cdot E_3 E_2^* \cdot e^{j\Delta k \cdot z} \\ \frac{dE_2}{dz} + \alpha_2 E &= j\kappa_2 \cdot E_3 E_1^* \cdot e^{j\Delta k \cdot z} \\ \frac{dE_3}{dz} + \alpha_3 E &= j\kappa_3 \cdot E_1 E_2 \cdot e^{j\Delta k \cdot z} \end{aligned} \tag{1.4}$$

where E_i is used to abbreviate $E(\omega_i)$ and

$$\kappa_i = \frac{\omega_i d_{\text{eff}} \varepsilon_o}{n_i \cdot c}; \qquad \alpha_i = \mu_o \sigma_i c/2;$$
$$\omega_3 = \omega_1 + \omega_2; \qquad \Delta k = k_3 - k_1 - k_2. \tag{1.5}$$

Above coupled-wave equations give the phase relationships, governing the direction of energy flow between any three interaction waves. Under the appropriate boundary conditions the coupled wave equation can be used to predict several characteristic features of nonlinear interaction.

B. Optical Second Harmonic Generation

In second-harmonic generation, radiation at an incident frequency ω_1 is converted to radiation at twice the frequency: $\omega_2 = 2\omega_1$. In this interaction, two of the three fields that figure in Eq. (1.4) are of the same frequency. From the coupled equations, exact solution can be found [9] for plane wave in the two cases of low and high conversion efficiency. As for low conversion efficiencies, the ratio of the power generated at the second-harmonic frequency to that incident at the fundamental frequency is approximated by [9]

$$\frac{P_{2\omega}}{P_\omega} = 2 \cdot \left(\frac{\mu}{\varepsilon_0}\right)^{3/2} \cdot \frac{\omega^2 d_{eff}^2 l^2}{n^3} \cdot \frac{\sin^2(\Delta k \cdot l/2)}{(\Delta k \cdot l/2)^2} \cdot \frac{P_\omega}{A} = l^2 K \frac{P_\omega}{A} \tag{1.6}$$

where l is the length of nonlinear crystal, A is the area of the fundamental beam, and $K = 2 \cdot \left(\frac{\mu}{\varepsilon_0}\right)^{3/2} \cdot \frac{\omega^2 d_{eff}^2}{n^3}$. For a given wavelength and a given nonlinear material, the conversion efficiency depends on the length of the crystal, the power density, and the phase mismatch term $\frac{\sin^2(\Delta k l/2)}{(\Delta k l/2)^2}$.

According to Eq. (1.6), a prerequisite for efficient second-harmonic generation is that $\Delta k = k(2\omega) - k_1(\omega) - k_2(\omega) = 0$ or $k(2\omega) = k_1(\omega) + k_2(\omega)$. This is termed phase-matching condition which describes the momentum conservation in the process. Similarly, in other second-order processes, the phase-matching condition $\Delta k = 0$ also dictates the nonlinear conversion efficiency and even frequency tuning behaviour in the parametric process. The most common approach to satisfying the condition is to make use of the birefringence in an anisotropic medium to compensate for material dispersion. In an uniaxial crystal, the dependence of refractive index of the extraordinary wave on the angle between the propagation direction and the crystal optics (z) axis is given by

$$\frac{1}{n_e^2(\theta)} = \frac{\cos^2\theta}{n_o^2} + \frac{\sin^2\theta}{n_e^2} \tag{1.7}$$

If $n_e^{2\omega} < n_o^{\omega}$, phase matching may be obtained in a wave normal direction such that $n_e^{2\omega}(\theta) = n_o^{\omega}$; so, if the fundamental beam is launched along θ_m as an ordinary ray, the second-harmonic beam will be generated along the same direction as an extraordinary ray. The above situation applies to a negative uniaxial crystal as type-I phase-matching. In general, SHG phase-matching can be achieved in uniaxial or biaxial crystals for type-I or type-II geometry. The so called "coherence length" defined by $l_c = 2\pi / \Delta k$ is a measure of the maximum crystal length that is useful in producing the second-harmonic power considering the absence of a complete phase match (i.e. $\Delta k \neq 0$). Phase-matching at an angle θ_m other than 0^o and 90^o is termed "critical phase-match". In such a geometry, the direction of power flow (Poynting vector) of fundamental and second harmonics will not be completely collinear but occur at a small angle. This effect can lead to a significant reduction in second-harmonic generation efficiency, especially with focused beams due to the larger linear dependence of $\Delta k(\delta\theta)$. However, in the case of "non-critical phase-matching", when $\theta_m = 90^o$, there are no walk-off effect. Thus, the dependence of Δk on angular misalignment $\delta\theta$ is due to a much smaller quadratic term. "Noncritical phase-

matching" can be achieved by temperature tuning the crystal for some specific wavelengths.

In practice, high-efficiency second-harmonic conversion depends on parameters of laser spectral brightness [W/cm^2 sterad Å] (in terms of power density, beam divergence, and frequency linewidth) and parameters associated with the harmonic generator (such as the value of the nonlinear coefficient, crystal length, angular and thermal deviation from the optimum operation point, absorption, and inhomogeneties in the crystal).

An analysis of optical SHG inside the laser resonator has been presented in references [10] and [11]. The steady-state condition for intracavity doubling can be determined if we equal the round-trip saturated gain of the laser to the sum of the linear and nonlinear losses

$$\frac{2g_o l^*}{1+I/I_s} = L + K'I \tag{1.8}$$

where g_0 is the unsaturated gain coefficient, l^* is the length of the laser medium, I is the circulating power density in the laser rod, and I_s is the saturation power density of the active material. All linear losses occurring at fundamental frequency are lumped together into the parameter L; the quantity $K'I$ is the nonlinear loss. The nonlinear coupling factor K' defined by $I(2\omega) = K' \cdot I^2(\omega)$ is related to K in Eq. (1.6); it is $K' = \kappa \cdot l^2 K$, where κ accounts for different power densities in the gain medium and nonlinear crystal in the case of focused beams and l is the crystal length. The optimum desired nonlinear coupling is given by

$$K'_{\max} = \frac{L}{I_s}. \tag{1.9}$$

This is quite different from the case of optimum coupling in ordinary laser where the optimum nonlinear coupling is dependent on the pump strength. Once K' is adjusted to it optimum value L/I_s, it remains optimal at any pumping level.

C. Optical Parametric Oscillation

As illustrated in Fig. 1.2.1, the optical parametric process is a nonlinear optical process in which a pump photon, when propagating in a nonlinear optical crystal, spontaneously or by stimulated emission breaks down into two lower-energy photons of frequencies (signal ω_s and idler ω_i) with the total photon energy conserved, i.e. $\omega_p = \omega_s + \omega_i$. The gain mechanism is based upon the stimulation emission process. That is, the rate of emission through the nonlinear optical parametric process is proportional to the photon present; thus the larger the number of photons emitted, the more likely photons will be emitted leading to parametric gain. Since the optical resonator provides resonance for the signal or idler waves (or both), the parametric gain will, at some threshold pumping intensity, cause simultaneous oscillation at the signal and idler frequencies. Once above threshold, the parametric oscillator efficiently converts the pump radiation to signal and idler frequencies. Two important parametric oscillator cavity configurations are the DRO, where both the signal and idler wave are resonated, and the SRO, where only one wave is resonant. Different operation characteristics including threshold, frequency stability and tunability, and pump laser requirements are possessed by the two configurations.

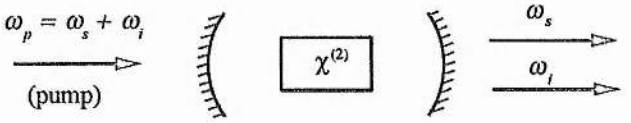

Fig. 1.2.1. The optical parametric oscillator. The cavity end mirrors have high reflectivity at frequencies ω_s and ω_i (DRO); ω_s or ω_i (SRO).

It is clear that the frequencies of signal and idler can not be solely determined on the basis energy conservation condition. This is in fact the basic source of tunability of the OPOs. The specific pair of frequencies that will result from any given situation is dictated by the phase-matching condition, $k_p = k_s + k_i$ (or $\omega_p n_p = \omega_s n_s + \omega_i n_i$), that must also be satisfied. Similar to the SHG phase-matching condition, the refractive index

matching can be achieved by either type-I or type-II phase-matching geometry. However, in an anisotropic medium, the index of refraction, and hence the magnitude of k-vector, of extraordinary wave continuously varies with the direction of propagation. For a negative uniaxial crystal, if the birefringence is sufficiently large to compensate for the dispersion, and if the pump beam is introduced as an extraordinary wave while the signal and idler waves are ordinary waves, a particular pair of frequencies of emitted ordinary photons will satisfy the type-I phase-matching condition for each orientation of the crystal relative to the direction of propagation of the pump photon. As the crystal is rotated or crystal temperature changes, the magnitude of the k-vector or the momentum of the pump photon changes. The frequencies of the resulting pair of emitting photons will change accordingly, and they continuously satisfy the phase-matching condition. These are the basic tuning schemes of OPO, termed "angle tuning" and "temperature tuning"

A variety of theoretical and experimental studies of DRO and SRO have been carried out [12][13][14][15]. Continuous-wave DROs have the advantage of low threshold and narrow linewidth. But it is offset by the necessity for overlapping the signal and idler cavity resonance in a single optical cavity which places server tolerance limit on the cavity length and causes the complexity of continuous frequency tuning. Single-frequency, narrow-linewidth pump laser is desired as pump source in double resonance OPO. In a single-pass CW pumped DRO, the threshold of pump power required for oscillation is given by

$$P_{th} = K \cdot \frac{\lambda_p^2 \alpha_s \alpha_i}{d^2 l \cdot \bar{h}_m} \tag{1.10}$$

where λ_p is the pump wavelength, α_s and α_i are the fractional round-trip power losses at signal and idler wavelengths, d is the effective nonlinearity of the crystal, l is the phase-matched interaction length, $\bar{h}_m$ is a generalised Boyd-Kleinman gain reduction factor, and

$$K = \frac{\varepsilon_0 c \cdot n_p^2}{8\pi^2 (1-\delta^2)^2} \tag{1.11}$$

is a slowly varying function of frequency near degeneracy, since $\delta = (\omega_s - \omega_i)/\omega_p$. The Boyd-Kleinman $\bar{h}_m$ factor represents a reduction in effective parametric gain because of poor pump-signal-idler mode overlap. Above the operation threshold, the conversion efficiency is simply given by [9]

$$\eta = \frac{P_s + P_i}{P_p} = \frac{2}{N}(\sqrt{N} - 1) \tag{1.12}$$

where N is the number of times above threshold, defined by $g^2 \cdot l^2 = \alpha_s \cdot \alpha_i$ (g^2 is the parametric gain coefficient). This relationship give a general rule for the design of an efficient CW OPO, that is to pump at least approximately 4 times above threshold for maximum efficiency.

1.3 All-Solid-State Frequency Conversion Devices

The progress in solid-state lasers, especially in linewidth control and frequency stability, has brought about rapid advances in CW OPO devices. This is largely due to the fact that the high spectral brightness of such pump sources can match itself into the over-constrained single-mode-pair oscillation condition of DRO and such laser sources are also capable of providing enough power for SRO. Through efficient harmonic generation, the frequency stability and narrow linewidth of the pump lasers can be extended into the visible and ultraviolet (UV) spectrum. They can further be used as pump sources for OPOs to down-convert their frequencies in a widely tunable visible or infrared range. In addition, the new high quality nonlinear materials, various resonant cavity designs, and servo control techniques enable CW OPOs to operate in a truly continuously tuning manner. Good-quality nonlinear-optical crystals with low material absorption are now available and new crystals have been developed for use over a wide spectral range. For

example, we have demonstrated the operation of a CW OPO using Lithium Triborate (LBO) crystal pumped by 364 nm UV light with type-II noncritical phase-matching [16] and pumped by 514.5 nm green light with type-I noncritical phase-matching geometry [17]. New cavity designs such as a monolithic ring DRO [1][18] have shown dramatically better mechanical stability. Recently, Colville *et al.* [19] developed a dual-cavity device in which two resonant fields are split into two separate cavities by a low-loss Brewster-angled plate. The independent control of the two cavities makes wideband and continuous tuning of the device theoretically possible.

As discussed before, two fundamental approaches in achieving widely tunable highly coherent radiation through nonlinear frequency conversion techniques in the continuous-wave operation regime are DRO and SRO. Both approaches have been demonstrated by employing the frequency-stable single-mode solid-state lasers and then frequency-doubled output as pump sources. It is suggested that the use of diode-pumped solid-state lasers in conjunction with CW OPO devices can realise efficient, compact, and frequency tunable CW radiation sources in all-solid-state configurations.

Nabors *et al.* [1] demonstrated stable, efficient CW single-mode operation of a monolithic Mg:O:$LiNbO_3$ DRO, pumped by frequency-doubled diode-pumped Nd:YAG laser. The device was tuned from 1007 to 1129 nm and exhibited a 34% conversion efficiency from 532 nm pump light to signal and idler power. A similar pump and OPO configuration was used by Gerstenberger and Wallace [20], where CW parametric oscillation with the tunability over the 965 - 1185 nm spectral range and 100 mW of output power was demonstrated. Operation over most of the spectral range consisted of single signal and idler pairs with low-amplitude noise. Lee and Wong [21] analysed the stability issue of type-II phase-matched Potassium Titanyl Phosphate (KTP) DRO. They systematically stabilised and tuned this device at frequency degeneracy. With four different tuning elements, the DRO signal-idler difference frequency was tuned discretely over a range of ~ 1-3 THz and continuously over a ~ 0.5-GHz range. The pump source used was a frequency-stabilised krypton-ion laser with a residual laser frequency noise of

~ 100 kHz rms. However, such a frequency stability can be provided by a diode-pumped solid-state laser. Schiller and Byer [22] combined doubly resonant harmonic generator and DRO into a single monolithic total-internal-reflection resonator (MOTIRR) and realised a quadruply resonant OPO with 0.4 mW pump threshold.

Yang *et al.* [2] first demonstrated a CW singly resonant OPO based on KTP. The pump source used was a single-frequency frequency-doubled Nd:YAG laser. The minimum oscillation threshold was 1.4 W with pump light double passed. With 3.2 W of incident pump power, a maximum 1.07 W tunable power was generated. They [23] further demonstrated similar operation in a ring configuration with 1.9 W of sing-axial-mode output. Recently, Robertson *et al.* [24] used pump-enhanced technique to overcome the difficulty of the high SRO operation threshold. They obtained single-frequency output of 500 mW with a 14 nm OPO tuning range. The pump threshold was 1 W of single frequency argon pump power at 514.5 nm .

1.4 Research Overview

This thesis describe the author's research work on the design and construction of a diode-pumped Nd:YLF laser and the nonlinear frequency conversion of this laser in the continuous-wave regime. The wavelength diversity of the device has accessed the 523.5 nm green spectrum with 9 GHz continuous tuning capability and the 1020 - 1070 nm (potential 950 - 1150 nm) infrared spectral range with 4.5 GHz smooth tuning capability in the single-frequency signal and idler mode pair output. The frequency conversion techniques of the Nd:YLF laser have involved SHG process (via intracavity SHG) and OPO process (via doubly resonant OPO). Potassium Titanyl Phosphate (KTP) has been employed as the nonlinear material in these processes. The efficient diode-pumping configuration not only gives a 30% optical efficiency of laser operation, but also enables the efficient frequency conversion due to the high beam quality. 50% intracavity SHG conversion efficiency and 60% pump depletion in doubly resonant OPO have been

demonstrated. In the course of this research, the following continuous-wave, highly coherent radiation sources have been developed:

1. *Diode-pumped Nd:YLF laser* generating 2.5 W TEM_{00} laser output at 1047 nm with 30% optical-to-optical conversion efficiency (see Chapter 3).

2. *Intracavity-frequency-doubled Nd:YLF green laser* producing 1 W single-frequency TEM_{00} SHG output with linewidth of less than 10 kHz and frequency tunability of 9 GHz (see Chapter 4).

3. *Single-frequency green laser pumped CW doubly resonant KTP OPO* providing continuous operation of tunable single-frequency mode-pair output at around degeneracy frequency range. Smooth tuning of 4.5 GHz in the 1020 - 1070 nm of the KTP phase matching wavelength range have been achieved (see Chapter 5).

Detailed considerations in relation with the design and construction of above devices are discussed in the relevant chapters.

The construction of diode-pumped Nd:YLF laser and the frequency-doubled Nd:YLF laser are based on a folded standing wave cavity design. This cavity design is subject to the available end-pumped geometry and the requirement for efficient intracavity second harmonic generation. In the laser cavity, an elliptical 1.5 x 0.5 mm^2 cross-section laser mode is produced in the gain medium to match with the appropriate size of diode pump profile, and an 80 μm diameter circular focused laser mode is produced in the intracavity KTP crystal offering the desired photon density. The novel intracavity birefringent filter formed by birefringent KTP crystal and intracavity Brewster plate are used in the Nd:YLF laser for the first time in achieving the high power single-frequency SHG operation. Multi-axial-modes at fundamental wavelength which are subject to the spatial hole burning effect in the standing-wave cavity are separated by the birefringent KTP crystal with different polarisation in the oscillation process. Different losses on these modes are applied by the Brewster plate providing a longitudinal modes

selection mechanism. These techniques employed in this frequency-doubled Nd:YLF laser to achieve the high power single-frequency SHG, demonstrate a new approach in frequency doubled solid-state laser designs. Chapters 3 & 4 will discuss and analyse these design and techniques in detail. The laser performance are further characterised in terms of laser threshold, slope efficiency, second harmonic conversion efficiency, mode quality, amplitude and frequency noise, linewidth, and frequency tunability.

The generation of single-frequency, continuous-wave tunable radiation in IR region has been demonstrated in a single cavity doubly resonant KTP OPO. Smooth frequency tuning of 4.5 GHz is achieved by tuning the green pump source. The stable single axial mode-pair operation of the device has been obtained by using the "side of fringe" locking technique to control the length of the OPO cavity so as to maintain the doubly resonant condition. The stability requirements for type-I LBO OPO and type-II KTP OPO, both of which operate near degeneracy, have been compared in the experiments. Evidence from both sources indicates that, for the single-mode-pair operation, type-II phase-matched geometry is superior to type-I phase matched geometry. This is brought about by the extreme sensitivity to mode hoping for a type-I DRO in which the free spectral ranges of signal and idler oscillation are nearly identical.

The rate equations of diode-end-pumped Nd:YLF laser have been developed in the section § 2.9, and theoretical analyses of laser performance are further discussed in the experiment chapters. Section § 4.4 theoretically analyses the mode selection behaviour of the novel intracavity birefringent filter. The tuning behaviour and stability requirements of single-cavity type-I and type-II doubly resonant OPO are studied. A good agreement between theoretical predictions and experimental results has been reached.

References

[1] C. D. Nabors, R. C. Eckardt, W. J. Kozlovsky, and R. L. Byer, "Efficient single-axial-mode operation of a monolithic MgO:$LiNbO_3$ optical parametric oscillator", *Opt. Lett.*, vol. 14, pp. 1134-1136, 1989.

[2] S. T. Yang, R. C. Eckardt, and R. L. Byer, "Continuous-wave singly resonant optical parametric oscillator pumped by a single-frequency resonant doubled Nd:YAG laser" *Opt. Lett.*, vol. 18, pp. 971-973, 1993.

[3] E. S. Polzik, J. Carri, and H. H. Kimble, "Spectroscopy with squeezed light", *Phys Rev, Lett.*, vol. 68, pp. 3020-3023, 1992.

[4] N. C. Wong, "Optical frequency division using an optical parametric oscillator" *Opt. Lett.*, vol. 15, pp. 1129-1131, 1990.

[5] D. A. Kleinman, "Nonlinear dielectric polarisation in optical media", *Phys. Rev.*, vol. 126, pp. 1977, 1962.

[6] Amnon Yariv, "Optical Electronics", *Saunders College Publishing*. 4th Ed., pp. 270.

[7] J. A. Armstrong, N. Bloembergen, J. Ducing, and P. S. Pershan, "Interactions between lightwaves in a nonlinear dielectric" *Phys. Rev.*, vol. 127, pp. 1918, 1962.

[8] R. G. Smith, "Effects of momentum mismatch on parametric gain", *J. Appl. Phys.*, vol. 41, pp. 4421, 1970.

[9] R. L. Byer, "Parametric oscillator and nonlinear materials", in *Nonlinear Optics*, P. G. Harper and B. S. Wherret, Eds., Academic Press: London. 1977.

[10] J. E. Geusic, H. J. Levinstein, S. Singh, R. G. Smith, L. G. Van Uitert, "Continuous 0.532-μm solid-state source using $Ba_2NaNb_5B_{15}$", *Appl. Phys. Lett.*, vol. 12, pp. 306, 1968.

[11] R. G. Smith, "Theory of intracavity optical second-harmonic generation", *IEEE J. Quant. Electron.*, vol. 6, pp. 215, 1970.

[12] R. L. Byer, "Optical parametric oscillator" in *Treatise in Quantum Electronics*, vol. 1, Nonlinear optics, Pts. A and B, H. Rabin and C. L. Tang Eds., New York Academic.

[13] C. L. Tang, "Spontaneous and stimulated parametric processes", in *Treatise in Quantum Electronics*, vol. 1, Nonlinear optics, Pts. A and B, H. Rabin and C. L. Tang Eds., New York Academic.

[14] R. G. Smith, "A study of factors affecting the performance of a continuously pumped doubly resonant optical parametric oscillator", *IEEE J. Quant. Electron.*, vol. 9, pp. 530-541, 1973.

[15] R. C. Eckardt, C. D. Nabors, W. J. Kozlovsley and R. L. Byer, "Optical parametric oscillator frequency tuning and control", *J. Opt. Soc. Am. B*, vol. 8, pp. 646-667, 1991.

[16] F. G. Colville, M. J. Padgett, A. J. Henderson, J. Zhang, and M. H. Dunn, "Continuous-wave parametric oscillator pumped in the ultraviolet", *Opt. Lett.*, vol. 18, pp. 1065-1067, 1993.

[17] F. G. Colville, M. J. Padgett, A. J. Henderson, J. Zhang, and M. H. Dunn, "Continuous-wave parametric oscillation in lithium triborate", *Opt. Lett.*, vol. 18, pp. 205-207, 1993.

[18] C. D. Nabors, S. T. Yang, T. Day, and R. L. Byer, "Coherence properties of a doubly resonant monolithic optical parametric oscillator", *J. Opt. Soc. Am. B*, vol. 7, pp. 815-820, 1990.

[19] F. G. Colville, M. J. Padgett, and M. H. Dunn, "Continuous-wave, dual-cavity, doubly resonant, optical parametric oscillator", *Appl. Phys. Lett.*, vol. 64, pp. 1490-1492, 1994.

[20] D. C. Gerstenberger and R. W. Wallace, "Continuous-wave operation of a doubly resonant lithium niobate optical parametric oscillator system tunable from 966 to 1185 nm", *J. Opt. Soc. Am. B*, vol. 10, pp. 1681-1683, 1993.

[21] D. Lee and N. C. Wong, "Stabilisation and tuning of a doubly resonant optical parametric oscillator", *J. Opt. Soc. Am. B*, vol. 10, pp. 1659-1667, 1993.

[22] S. Schiller and R. L. Byer, "Quadruply resonant optical parametric oscillation in a monolithic total-internal-reflection resonator", *J. Opt. Soc. Am. B*, vol. 10, pp. 1696-1707, 1993.

[23] S. T. Yang, R. C. Eckardt and R. L. Byer, "1.9-W ring-cavity KTP singly resonant optical parametric oscillator", *Opt. Lett.*, vol. 19, pp. 475-477, 1994.

[24] G. Robertson, M. J. Padgett, and M. H. Dunn, "Continuous-wave singly resonant pump-enhanced type II LiB_3O_5 optical parametric oscillator", *Opt. Lett.*, vol. 19, pp. 1735-1737, 1994.

Chapter 2

DIODE-PUMPED SOLID-STATE LASERS AND THEIR FREQUENCY DOUBLING

2.1 Introduction

The advances in semiconductor diode lasers have caused a resurgence in solid-state laser technology. This is mainly because with efficient diode laser pumping, the potential of solid-state laser materials can be fully utilised for laser performance. Remarkable improvements in terms of higher slope efficiency, narrower frequency linewidth, ultrashort pulses, and higher peak powers, have been brought about by diode pumping in recent years. Based on the long lifetime and inherent stability of the diode laser and solid-state gain medium, the realisation of all-solid-state lasers has become possible. These all-solid-state devices provide stable output with high efficiency, ease of operation, long lifetime, reliability and robustness in compact forms. Combined with the techniques of nonlinear frequency conversion or direct pumping of tunable solid-state laser materials, all-solid-state lasers can be envisaged to allow complete optical spectral coverage and wavelength tunability [1][2]. These advantages of diode-pumped devices have led to the development of new lasers which are impossible or impractical to realise in other ways, and are making a great impact on new technologies.

This chapter briefly introduces the basic physical process of diode pumping solid-state materials, and describes the historical works and recent developments on diode-pumped solid-state lasers. After the comparison of diode-pumped solid-state lasers with other devices, we concentrate on the continuous-wave (CW) diode-pumped lasers by describing the design and engineering criteria, and analysing the single frequency operation and frequency doubling schemes. There follows a discussion of rate equation models to describe CW end-pumped Nd:YLF lasers. Expressions of diode-pumped laser

threshold and optical slope efficiency are given for the analyses of experiments in following chapters.

2.2 Basic Concept and Historical Overview

The early work on the use of semiconductor diode lasers as pump sources for solid-state laser started in the early 1960's. Soon after the advent of diode laser, Newman [3] recognised that the spectral overlap of the GaAs diode laser emission wavelength with absorption band of Nd^{3+} could lead to an efficient, compact, all-solid-state laser. Keyes and Quist [4] tested the idea and demonstrated the first diode-laser-pumped Uranium-doped CaF_2 laser in 1964. They noted that the use of GaAs diode lasers should be ideal for the pumping of Nd^{3+} laser and that such a device should be more efficient than lamp pumping. This would induce less heating in the gain medium and reduce the thermal problems of high-power lasers. However, the low power and the cryogenic cooling requirement of early diode laser devices halted the development of all-solid-state lasers in 60's and 70's. Most initial works had concentrated on designing and demonstrating simple Nd^{3+} doped devices, because the Nd^{3+} doped material possessed strong absorption in the emission band of GaAs, GaAlAs, and GaAsP diode lasers, and they had many narrow fluorescent transitions in the infrared region.

A. Optical Pumping Process in Nd^{3+} Doped Materials

To examine the physical processes of diode pumping which leads to the high efficiency displayed by all-solid-state lasers, we take the widely used neodymium doped materials as an example. Fig. 2.2.1 shows the energy level diagram of the Nd^{3+} ion. Each of the $^{2s+1}L_J$ manifolds of Nd in the figure is split by the crystal field into J+1/2 doubly degenerate energy levels. The positions of these levels are different for each host, although the centre of gravity of each manifold is approximately the same. These representative Stark splittings of the manifolds are also shown in the figure, and actual laser transitions occur between these individual Stark splittings. The strong absorption

spectra of Nd^{3+} doped materials like Nd:YAG and Nd doped phosphate are around 800 nm. Under the illumination of diode light at this wavelength, the Nd^{3+} ions are excited into pump bands and then relax efficiently to the upper laser level.

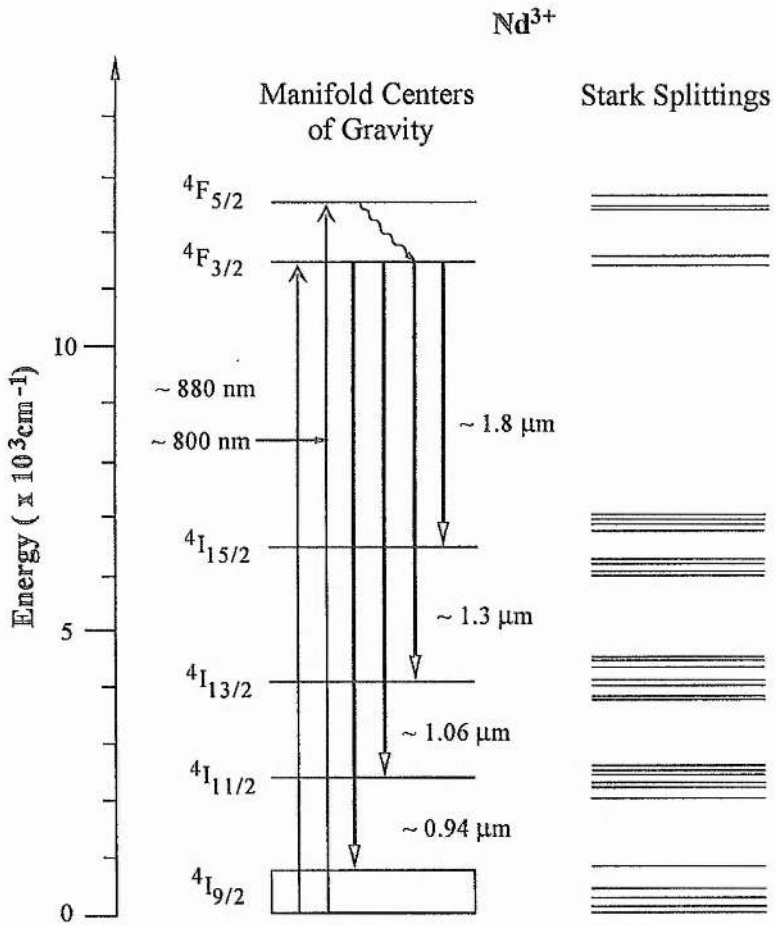

Fig. 2.2.1. Energy level diagram of Nd^{3+}. The laser transitions are shown in heavy lines, diode pump transitions in light lines, and relaxations in wavy lines. The open box for the ground-state manifold indicates that the laser transition to this manifold is to an energy level above the ground state.

From this upper laser level $^4F_{3/2}$, there are two four-level transitions with high gain, the $^4F_{3/2}$ - $^4I_{11/2}$ and $^4F_{3/2}$ - $^4I_{13/2}$ which correspond to emissions at 1.06 μm and 1.3 μm. Since both terminal transition levels are not thermally populated, laser action can be easily achieved with low lasing thresholds. The three-level transition $^4F_{3/2}$ - $^4I_{9/2}$ produces emission at 0.94 μm, but usually with poor efficiency due to the thermally

populated terminal level. Since the neodymium ions are excited into the pump bands that lie only slightly above the upper laser level by diode light, the non-radiation waste energy generated is much lower than that of the same-power lamp pumping, which means higher quantum efficiency for the laser transition. Together with the efficient absorption of narrow bandwidth diode light, high optical conversion from the diode light to the 1.06 μm high-gain line of Nd^{3+} can be obtained.

B. Early Work on Diode-Pumped Solid-State Laser

Ross [5] demonstrated the first Nd:YAG laser side-pumped by a single GaAs diode. He noted that solid-state laser could produce high peak power in a short pulse due to the long upper state lifetime of the material, with a narrower spectral bandwidth and higher spatial brightness. Both laser diode and LED-pumped Nd:YAG lasers in side-pumping and end-pumping geometries were investigated. Side-pumping geometry appeared to be convenient when using a number of sources with poor beam quality, while the end-pump approach had the advantage of minimising the laser threshold and the disadvantage of limited power scaling due to the problem of coupling the output of many diode sources into the gain medium. It was recognised that the high brightness of diode light could be absorbed in a small volume in the gain medium, thus leading to lower threshold and higher gains. Ostermayer *et al.* [6] demonstrated the $GaAs_{1-x}P_x$ diode-arrays-pumped Nd:YAG laser operating at room temperature in continuous-wave. Illuminated by diode laser and LEDs respectively, CW operation of Nd:YAG lasers were demonstrated in side-pumping [7][8] and end-pumping geometry [9][10].

In the mid-70's, diode and LED pumping were also applied to a class of materials called stoichiometric in which Nd^{3+} was a chemical component of the crystal itself. Due to the fact that concentration of active ions could be much higher in stoichiometric materials than that in the dopant host, a shorter absorption length for the pump radiation was available. Most of the work reported in this field had employed $LiNdP_4O_{12}$ (LNP) crystal with LED pump [11]. Fibre optic wave-guided devices had been transversely or longitudinally pumped by diode lasers and LEDs. The first fibre laser pumped with a

diode was the Nd-doped silica fibre laser with 1 mW laser threshold and 1.088 μm lasing wavelength [12]. Besides the Nd-doped gain media, there were also reports on diode and LED pumping of other ions such as Yb:YAG and Tm,HO:$LiYbF_4$. Frequency conversion of diode-pumped lasers, driving of spiking oscillations, and the Q-switching and the mode-locking to generate higher peak powers had also been investigated.

2.3 Laser Diode Array Pumps

As Newman first recognised, the major advantage of diode pumps is the spectral overlap of the diode emission wavelength with the absorption peak of trivalent Neodymium doped materials. But only after the availability of reliable diode lasers can this advantage be practically realised. Today diode lasers are compact, efficient, robust, and potentially inexpensive, with long room-temperature lifetime. We review the present status of diode laser arrays as solid-state laser pump sources.

The conventional (GaAl)As laser light is generated in an active region via the recombination of electron-hole pairs after charge injection across a forward biased p-n junction. With different percentages of Ga and Al, the output wavelength of (GaAl)As laser diode is in the vicinity of 800 nm, ranging from approximately 700 to 900 nm. These emission wavelengths coincide very well with the strong absorption bands of trivalent rare earth (RE) lasing ions. A single diode stripe typically can provide a few milliwatts of output power in a single spatial mode. To increase the output power, configurations such as multiple quantum wells (MQW) (or active-region-enlarged single quantum wells) and separate confinement heterostructures (SQW-SCH) are usually employed [13]. Fig. 2.3.1 illustrates a multiple quantum well (multiple-stripe) laser. As shown in the figure, a number of diode stripes are fabricated in a single device to obtain a wider emitting aperture, thus much higher output powers can be achieved. True arrays of diode stripes tend to be partially coherent and many exhibit the two-lobe structure in the far-field characteristic of a π change due to the evanescent coupling between adjacent stripes. As the output power and number of stripes increase, this feature appears less obvious. The

broad stripe arrays are multi-transverse mode devices and the beam quality is dependent on the drive current. Both types of diode arrays have been used in end-pumped geometries. Since the emitting region may be overall 500 μm wide by 1 μm deep, the divergence is different in the two emitting planes. Diode light coupling optics are often used.

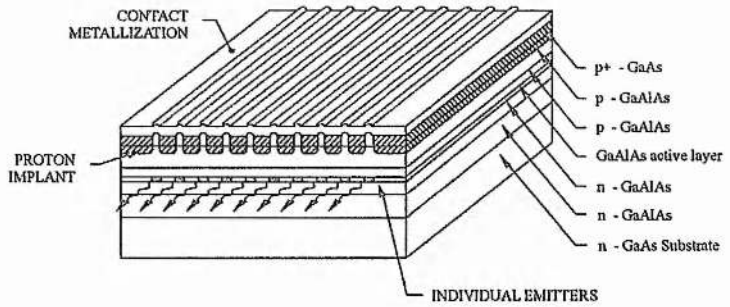

Fig. 2.3.1. Schematic diagram of a gain-guided multistripe diode array

The scaling of CW arrays to higher powers is normally achieved by using a bar structure. The commercial 5 - 20 W bar devices which are grown on single 1-cm substrate are composed of a number of individual arrays with an aperture of ~ 100 μm and periodical spacing of ~ 500 μm. Since the diode bar is made up of a number of independent source, the wavelength change along a bar may be 2 - 3 nm due to small material variations. The output of these devices is difficult to couple into solid-state materials particularly in end-pumping geometry. Presently, many diode array package architectures are available ranging from low array/package level to high level integration. They are capable of achieving 5 kW/cm^2 peak power and 1 kW/cm^2 average power for applications with low duty cycle (< 1%) and high duty cycle (20%) requirements. To achieve high pump brightness (W/cm^2/sr^2), various diode light coupling and beam shaping techniques have also been developed. CW fibre-coupled bar can provide as high as 10 kW/cm^2 CW pump density with 80% efficiency using 400 μm fibres. Fibre and other coupling schemes are expected to continually increase pump brightness above the levels currently attainable.

Depending on the type of semiconductor material, the wavelength range from 630 to 1020 nm can be accessed. The GaAlAs devices have a spectral coverage of 780 - 860 nm. Longer wavelengths are available with InGaAs devices (900 - 1020 nm). AlGaInP diode lasers cover the red end of visible spectrum (630 - 670 nm). This broad range of pump wavelengths provides an opportunity for new applications such as pumping of Er:glass, Er:YAG, and Yb:YAG lasers (long-wavelength pumps), as well as Cr:$LiCaAlF_6$ and Cr:$LiSrAlF_6$ lasers (short-wavelength pumps). While a given diode with a particular semiconductor composition will emit at one specific wavelength, the variation in its operating temperature allows the wavelength to be tuned by typically ~ 0.3 nm/^oC (GaAlAs). Efficiency and long lifetime are fundamental advantages of diode laser arrays. The commercial diode arrays have electrical to optical conversion efficiency of around 30 - 50%; and room-temperature lifetime of 3 x 10^4 h for CW devices, and around 10^9 pulses for pulsed diodes. Improved material quality has been combined with high aluminium cladding structures to produce Q-CW bars with excellent performance at high junction temperatures (exceeding 75 ^oC).

However, there are a few drawbacks of diode pumps. Firstly, typical diode laser arrays have an emission aperture of ~ 1 μm x ~ 100 μm with beam divergence angles of ~ 40^o x 10^o (FWHM). It is difficult to collect and effectively utilise this rapidly divergent and asymmetric emission pattern, especially in the end-pumped geometry. Secondly, diode laser are susceptible to damages caused by electro-static discharge, voltage transients, or photon induce facet damage. Thirdly, these devices are still fairly expensive.

2.4 Present Progress of Diode-Pumped Solid-State Lasers

With continuous improvements of the semiconductor diode laser since the early 1980's, solid-state laser technology has shown a tremendous growth. In parallel, it has been complemented by the development of new laser material, new diode light delivery schemes, and new concepts in crystal geometry and laser design.

A. Diode-Pumped Nd-doped Lasers

Apart from Nd:YAG, various Nd-doped gain materials have been employed in diode-pumped laser systems. They have slightly different spectroscopic properties due to the host atomic structure and the concentration level of active element, although the laser transitions are achieved by the same processes. Three important properties are upper state lifetime, absorption spectra and output wavelength. The different characteristics of these gain media may dictate their particular applications. Most of the recent research on diode-pumped Nd-doped lasers have concentrated on the high-gain four-level $^4F_{3/2}$ - $^4I_{11/2}$ transition, although laser performance at $^4F_{3/2}$ - $^4I_{13/2}$ transition and three-level $^4F_{3/2}$ - $^4I_{9/2}$ transition has also been reported. Table 2.1 lists some optical properties of commonly used Nd-doped gain materials.

Table 2.1. Comparison of some commonly used Neodymium (Nd) doped materials

Material	*Formula*	τ	σ	λ_p	λ_l	*special features*
YAG	$Y_3Al_2(AlO_4)_3$	220	2.8	807.5	1064.2	good thermal, mechanical, and optical quality
YLF (π) (σ)	$YLiF_4$	460	1.87 1.25	792.5 806.0	1047.0 1053.0	long fluorescence lifetime for Q-switch, mode locked operation
YVO_4	YVO_4	100	15.6 (π)	809	1064.3	strong absorption and wide emission band width
Glass	LG760 phosphate glass	350	2.0	801	1053.0	large gain bandwidth smaller gain cross section
$YAlO_3$	$YAlO_3$	150		800.0	1079	can operate on 6 lines around 1.06 μm
YAB	$Nd_xY_{1-x}Al_3(BO_3)_4$	60	2	808	1063	nonlinear host crystal for self-frequency doubling

τ: lifetime at 1 at % (μs); σ: effective laser cross section (10^{-19} cm^2); λ_p: peak of absorption wavelength in 800 nm region (nm); λ_l: lasing wavelength for the $^4F_{3/2}$ - $^4I_{11/2}$ transition (nm)

Nd:YAG is noted for its hardness, high thermal conductivity and good optical quality. It has been widely used in various laser designs of side-pumping and end-pumping schemes for CW or pulsed operations. Low thresholds and high slope

efficiencies are exhibited due to its strong pump absorption and narrow emission spectrum. Berger *et al.* [14] have reported an overall efficiency of 10.8% and an output power of 415 mW from a Nd:YAG laser end-pumped by a diode array. In fact, diode-pumped Nd:YAG lasers have already become important commercial devices for the full range of laser operations from CW single-frequency to Q-switched and mode-locked. Efficient and high power Nd:YAG systems have also been developed in recent years using different crystal geometries and diode pump schemes. Improved beam quality has been achieved in these systems due to efficient heat removal and reduction of thermal effects. The research group in Lawrence Livemore National Laboratory (LLNL) has obtained 4 kW average output power [15] from a Nd:YAG slab laser system. The slab dimensioned 200 x 25 x 6 mm^3 is pumped by two arrays each incorporating 150 diode packages. Golla *et al.* have demonstrated 300 W CW output power from a 1100-W side-pumped Nd:YAG laser [16].

Nd:YLF has a few distinct advantages for diode-pumped laser performance. Efficient Nd:YLF laser with polarised output at 1.047 μm and 1.053 μm has been demonstrated [17]. Thermally induced birefringence can be swamped by its natural birefringence. Since Nd:YLF has longer upper level lifetime and relatively low emission cross-section, it is an attractive medium for the generation of high peak power Q-switched pulses. Baer *et al.* [18] have obtained as high as 70 kW peak power in a pulse of duration less than 10 ns from a 10-W diode-pumped Nd:YLF laser.

Nd:glass has a wide absorption spectrum and can be doped at very high concentrations. However, the main disadvantage is its low thermal conductivity which makes the Nd:glass laser susceptible to thermal effects. A pump power threshold of 2 mW and a slope efficiency of 42% have been obtained when pumped with a low-power diode [19]. By using a spinning glass disc as the gain medium to overcome the thermal problem, Fan [20] has obtained 550 mW output power from 2 W diode pumps. Basu and Byer have predicted that 20 kW of average power could be achieved by using Nd:glass laser in the zig-zag slab and rotating geometry [21].

Other Nd-doped laser materials, e.g. Nd:BEL, Nd:GSGG, Nd:LNA, Nd:YVO_4, Nd:YAP, have also been developed with advantages in some respects of laser performance. Scheps [22] has reported 635 mW output from an diode-pumped Nd:BEL laser. It is noted that Nd:BEL has greater energy storage capacity and higher active ion concentration ability than Nd:YAG. Nd:YVO_4 has a broad absorption band in 800 nm region and exhibits a very high slope efficiency. Fields *et al.* [23] have reported an end-pumped YVO_4 laser with 750 mW output power, 64% optical slope efficiency, and an overall efficiency of 15.8 % [23]. It is suggested that Nd:GSGG could be a useful laser material for high average Q-switched operation. Caffey *et al.* [24] have reported an optical slope efficiency of 41.5% for Nd:GSGG in the rod geometry when side pumped. Nd:YAP laser can be operated at both 1.34 μm [25] and 1.083 μm [26] with high slope efficiency. By using a Lyot filter, laser emission on six of the laser lines of the $^4F_{3/2}$ - $^4I_{11/2}$ transmission has been achieved [26]. Self-frequency-doubling operation has been demonstrated in the diode pumped Nd:YAB laser. Lin *et al.* [27] have obtained more than 80 mW of green radiation with 1 W of diode pump power from a monolithic YAB device.

B. Diode-Pumped Rare-Earth-Doped Lasers

Trivalent rare earth ions other than neodymium also have significant absorption in the 750 - 850 nm and around 900 nm diode pump region. They provide additional wavelengths and different spectroscopic properties for laser performance. Recently, there has been great interest in diode-pumped eyesafe lasers in the 1.5 μm, 2 μm and 3 μm wavelength regions. In particular, the high pump rate of diode array provides a great advantage for the quasi-three-level laser schemes, such as erbium laser at 1.5 μm and thulium or holmium laser in the 2 μm region.

Fan *et al.* [28] have demonstrated single-stripe diode-pumped 2-μm Ho:YAG laser, where the Ho^{3+} ion is sensitised with Tm^{3+} at room temperature. In this laser, the pump radiation is absorbed by Tm^{3+} ions. This is followed by a cross-relaxation process and energy transfer to the Ho^{3+}. Threshold of 4.4 mW in absorbed pump power with 19 percent slope efficiency has been shown. Hemmati [29] has reported 30% slope efficiency

and a pump power threshold of 108 mW in Tm,Ho:YLF laser on the same transition. Both Ho:YAG and Ho:YLF have long fluorescence lifetimes, so they are promising media for Q-switched operation. Tm:YAG at the $^3F_4$ - $^3H_6$ transition is also a good candidate for high-energy Q-switched operation due to the same reason. Suni and Henderson [30] have reported both CW and Q-switched operation, obtaining CW output power of 530 mW for 1.37 W diode pump power. This correspond to an optical slope efficiency of 4%. They have further obtained pulse energies of 2.5 mJ at 50 Hz repetition rate from a diode-pumped Tm:YAG [31].

The recent development of strained layer InGaAs diode operating between 870 nm and 1.1 μm has opened the way for pumping erbium and ytterbium doped laser operating at 1.5 μm, and 3 μm (for Er^{3+} transitions), and 1.03 μm for (Yb^{3+} transition). Hutchinson *et al.* [32] have reported Yb sensitised Er:glass laser operating at 1.535 μm in an InGaAs diode laser end-pumped geometry. The optical slope efficiency obtained was 7.1% and the pump power threshold was 0.9 mJ. Denker *et al.* [33] have obtained diode-pumped slope efficiency of 14% and output energies up to 18 mJ from highly concentrated Yb,Er:boro-silico-phosphate glass laser. Yb^{3+} has a broader absorption spectrum in diode pump region and longer fluorescence lifetime than Nd:YAG. Efficient laser performance at 1 μm has been demonstrated in diode-pumped Yb:YAG laser [34].

C. Other Diode-Pumped Lasers

Visible (670 - 680 nm) AlGaInP diode lasers have recently been used to pump metal ion Cr^{3+} doped solid state lasers. Tunability of the emission in the metal ion doped material can be achieved when the stimulated emission of photons is intimately coupled to the emission of vibrational quanta (phonons) in a crystal lattice. In these "vibronic" lasers, the total energy of the lasing transition is fixed, but can be partitioned between photons and phonons in a continuous fashion, giving a broad wavelength tunability of the laser output [35]. Scheps *et al* [36] have successfully pumped the highly tunable (from 700 nm to 800 nm) alexandrite ($Cr:BeAl_2O_4$) laser. Other tunable chromium lasers including

Cr:LiCAF and Cr:LiSAF have also been operated by using diode arrays as the pump source.

Stoichiometrics are of interest for miniature lasers because of their high concentration of active ions. Kubodera *et al* [37] have reported diode-pumped operation of LNP laser at both 1.05 μm and 1.32 μm. The optical slope efficiency of 18.2% (threshold 0.6 mW, output power 2 mW) at 1.05 μm and 6.5% (threshold 2.7 mW, output power 0.5 mW) at 1.32 μm have been obtained. Single transverse and longitudinal mode was achieved by using the 300 μm thick active crystal.

In addition to bulk lasers, progress has been made in waveguide devices. Low threshold optical fibre laser operation has been demonstrated in a variety of rare earth ions and glass fibre hosts. Diode-pumped Nd-doped silica fibre laser operating at 0.905, 1.06 and 1.4 μm [38], and Er-doped silica fibre laser operating at 1.553 μm [39] have also been demonstrated. By using fluorozirconate fibres as the host medium, laser action has been achieved in thulium-doped fibre (operating at 2.3 μm [40] and 1.97 μm [41]), erbium-doped fibre (operating at 2.7 μm) [42], and neodymium-doped fibre (operating at 1.345 μm) [43]. Only recently diode-pumped upconversion fibre lasers have been demonstrated in erbium-doped glass fibre laser [44]. Piehler *et al.* [45] have obtained 11 mW of green light from 0.03 NA, 2.0-μm core erbium-doped fluoride fibre laser pumped by a 150 mW fibre pigtailed InGaAs diode laser operating at 971 nm. Waveguide lasers have also been fabricated in bulk glasses and in a variety of crystals [46]. Aoki *et al* [47] have reported 150 mW output power from a diode-pumped Nd:glass waveguide laser. More recently, by using ion implantation waveguide fabrication technique, ion-implanted channel waveguide laser operation has been achieved in Nd:GGG [48], and Nd:YAG[49].

D. Mode-Locked Diode-Pumped Nd-doped Lasers

Both active and passive mode-locking techniques are used in diode-pumped solid-state lasers. Active mode locking employs intra-cavity modulators which can be either an acousto-optic amplitude modulator (AM mode-locking) or an electro-optic phase modulator (FM mode-locking). By using amplitude mode-locking method which is

achieved by an intracavity acousto-optic modulator, active mode-locking of diode-pumped Nd:glass, Nd:YAG and Nd:YLF have been demonstrated [50][51][52]. As short as 4 ps has been produced in Nd:glass laser [50]. Nd:YAG, Nd:YLF and Nd:glass have all been mode-locked by FM techniques using electro-optic phase modulators. Pulses of 12 ps, 9 ps and 9 ps, respectively have been achieved [53][54][55]. Compared with active mode-locking methods, passive coupled-cavity mode-locking has been demonstrated to be an effective technique for ultrashort pulse generation. Diode-pumped Nd:YAG, Nd:YLF and Nd:glass have been mode-locked by this process producing pulses with durations of 1.7 ps, 1.5 ps and 380 fs, respectively [56][57][58]. Recently the use of frequency doubling crystals or multiple quantum well (MQW) structures in novel coupled-cavity have also been investigated. Combining the mode-locked diode-pumped laser with Q-switched operation, Keen and Ferguson [59] have obtained a peak power of 170 kW from a 2-W diode-pumped Nd:YAG laser operating at 1.3 μm. Without Q-switching, mode-locked pulses 19 ps were obtained.

2.5 Comparison of Diode-Pumped Lasers with Other Devices

A. Diode-Pumped Versus Lamp-Pumped Solid-State Lasers

Solid-state lasers have traditionally been pumped by pulsed flashlamps or CW arc lamps. These pump sources have broadband emission, which has poor overlap with the discrete absorption bands of the dopant trivalent ion in the crystal. Despite some lamps possessing high electrical-to-optical conversion efficiency, typically only 5% of the energy supplied to the lamp is emitted in the region of absorption line. In contrast, diode lasers are efficient (25% - 50% electrical-to-optical) pump sources with narrowband emission. Their wavelengths may be adjusted by varying the diode material composition during wafer growth and be further tuned to coincide with the absorption band of a particular laser material by controlling the operating temperature. Furthermore, because diode pumps have much higher spatial brightness than lamps, their output beams may be efficiently spatially coupled into the solid-state laser mode. These pump characteristics

can result in highly efficient pump absorption and utilisation of the pump energy in achieving an overall efficient laser system. Another advantage of using diode as pump source is its longer lifetime (tens of thousands of hours compared to a few hundred to a couple of thousands hours for arc lamps), which gives diode pumped lasers reliability and operational convenience. Based on these inherent advantages of diode pumps, diode pumped devices can exhibit a new regime of laser operation which is unattainable with lamp pumping. To our knowledge, the highest electrical-to-optical or "wall plug" efficiency of diode pumped solid-state lasers have reached 20% [60]. In contrast, a good flashlamp pumped Nd:Gr:GSGG laser only has a wall-plug efficiency on the order of 5%. In our laboratory we have demonstrated a 5 W diode-pumped Nd:YLF laser with 11.5% wall-plug efficiency. In the future, because the diode laser efficiency has the potential to approach 65 ~ 70 %, the overall electrical-to-optical efficiency of diode-pumped solid-state laser can be further increased.

Efficient and stable diode pumping also provides better frequency stability and narrow linewidth than that of lamp-pumping. This is due to the decreases of technical noise by reducing specific thermal loading in laser gain media. Compared with the frequency stability of lamp-pumped lasers in the region of 30-40 MHz, less than 3 kHz linewidth has been obtained in a free-running diode-pumped lasers [61]. By applying frequency stabilisation techniques, the laser linewidth can be further reduced to sub-hertz levels. Efficient pump source also means much less requirements for cooling systems for either the diode laser or the solid state material. By combining their high stability with the long life time and robustness, design and fabrication of high-stability, high spatial and spectral optical quality monolithic and conventional solid-state lasers are already a reality [62][63]. Even in the regime of high power operation, approaching 4 kW, diode array pumping has been used to obtain several hundred watts of average output power [15].

In comparison with the mature flashlamp-pumped technology, the field of diode-pumped solid-state laser is moving forward rapidly and improved laser performance are further expected. There are two driving forces in this development. Firstly,

semiconductor laser industry will provide more efficient, better beam quality, and higher power diode array pump sources at a lower cost and with self-contained cooling system. Secondly, the combination of the diode pumps and solid-state laser material provides many opportunities for new optical delivery schemes and innovative crystal geometry designs. While diode-pumped solid-state lasers offer the possibility of greatly improved performance over lamp-pumped solid-state lasers, they also provide the basis for many innovative laser designs which are impossible with lamp pumps, such as erbium-doped fibre amplifier and miniature lasers.

B. Diode-Pumped Lasers and Diode Lasers

The diode-pumped solid-state laser can be considered as a "mode converter" that improves the quality of diode laser output to achieve much better spatial and spectral mode and various temporal performance. Although diode lasers are one of the most efficient devices for generating coherent radiation from electrical energy, and although looking into the future, some of the disadvantages in the beam quality and output power of the diode laser may well be overcome, the basic physical property and the quantum well structure of the diode laser prevent such devices from providing a high degree of coherent radiation and various temporal performances which are necessary for many applications such as coherent optical radar, interferometric sensing, and holography. The spatial beam quality of current commercial high-power diode arrays is typically non-uniform with strong astigmatism. The spectral output of diode arrays is nanometers wide. The frequency is temperature- and drive current-dependent (which are considered as important factors in the spectral instabilities). Since the diode lasers are CW devices in nature, the peak power of diode lasers enhanced by pulsing is limited to about an order of magnitude of their CW output level. Another limitation to this peak powers is their low facets damage thresholds. The fundamental limit on the laser linewidth lies in the Schawlow-Townes equation, given by [64]:

$$\Delta\nu = h\nu / (2\pi \cdot \delta^2 P) \qquad (2.1)$$

where $\Delta\nu$ is the linewidth in hertz, δ is the cavity decay time, P is the output power, and $h\nu$ is the output photon energy. Due to the short cavity and the low reflectivity of the facets, a small δ is given. Compared with the δ of a diode-pumped Nd:YAG laser [65], this figure is on the order of 10^3 smaller. Therefore, the fundamental linewidth limit is 10^6 greater than that of a diode-pumped Nd:YAG laser. On the contrary, the linewidth of diode-pumped lasers could be much narrower than that of both diode lasers and lamp-pumped lasers. Other disadvantages of beam quality inherent with diode can also be overcome in diode-pumped lasers. (a) Single frequency output has been obtained from diode-pumped solid-state lasers by applying different frequency selection schemes. (b) In an end-pumped geometry the diode arrays can be spatially coupled into a TEM_{00} diffraction-limited solid-state laser mode by optical fibre or a set of lens. (c) Since solid-state laser materials have longer upper state lifetime, diode-pumped lasers are capable of producing high peak power in a Q-switched or mode-locked manner. For example, a 10-J, 100-Hz laser system has been developed in an all-solid-state form [66].

In brief, diode-pumped solid-state lasers take advantage of long life-time, efficiency and compactness of diode pumps and offer significant improvements in laser performance over lamp-pumped devices and the diode itself. They are capable of every type of laser operation: ultralow-noise continuous output; short pulse, high repetition rate by using Q-switching; ultrashort pulse by using mode-locking; and even in the high power regime. Improved laser performance of these laser systems is expected in the future.

2.6 Design of High Efficiency Diode-Pumped Lasers

Diode pumps present new challenges to the solid-state laser design. The basic principle of using diodes as pump source for solid-state materials is to make an optimal matching in their optical, mechanical and thermal properties. Since both the diode laser and the solid-state material are efficient, reliable, and robust with long lifetime, careful design is required

to obtain an overall optimum system. As a pump source, the diode output can be spectrally tuned on the absorption line of trivalent rare earth ion doped materials. The key element in optimising the efficiency of a solid-state laser is maximising the overlap of the region excited by the pumping source with the volume in the active medium occupied by the desired laser mode. Various pump geometries with diode array coupling techniques have been developed for this purpose.

A. Pump Schemes

Most pumping schemes may be categorised as either side- (transversely) pumped or end- (longitudinally) pumped, as shown schematically in Fig. 2.6.1 (a) and (b) respectively. End-pumped lasers use appropriate optics to couple and focus the diode light into the laser crystal in a small volume normally at the end of the crystal. The influence of the pump and laser mode size on laser threshold and output power has been investigated by various authors. It has been shown that the size of the pump distribution with respect to the size of the Gaussian laser mode is usually more important than the form of the pump distribution. Assuming that there is a continuous-wave power P incident on the laser material of a length l_{rod}, and the pump light is substantially absorbed inside the material, the steady state population inversion ΔN, in the absence of the stimulated emission, is [35]

$$\Delta N = \frac{P}{h\nu_p} \cdot \frac{\tau}{A \cdot l_a} \tag{2.2}$$

where τ is the fluorescence lifetime of the upper laser level, $h\nu_p$ is the pump photon energy, A is the cross section of the pump beam distribution, and l_a is the pump absorption length. The steady state gain, in this case, may be estimated to be

$$G = \exp(\Delta N \sigma_e l_a) = \exp(\frac{P}{h\nu_p} \cdot \frac{\tau\sigma_e}{A}) \tag{2.3}$$

where σ_e is the stimulated emission cross section at laser wavelength. The gain has no dependence on the absorption length of the material when $l_a < l_{rod}$. If the pump beam brightness is high enough, high efficiency can be attained due to the fact that good spatial mode overlap and high pump density improve the pump absorption. By ensuring a pump volume inside the TEM_{00} laser mode volume, a TEM_{00} output can be produced. This geometry is extensively used in many applications for the high conversion efficiency (typically over 30%) and excellent beam quality. However, end-pumped systems are generally restricted to low- and moderate-power regime due to the limitations of poor spatial beam quality of diode laser pumps. In addition, the strong thermal lensing and thermal stress in the small pump region, and the high pump density may also reach the crystal fracture threshold.

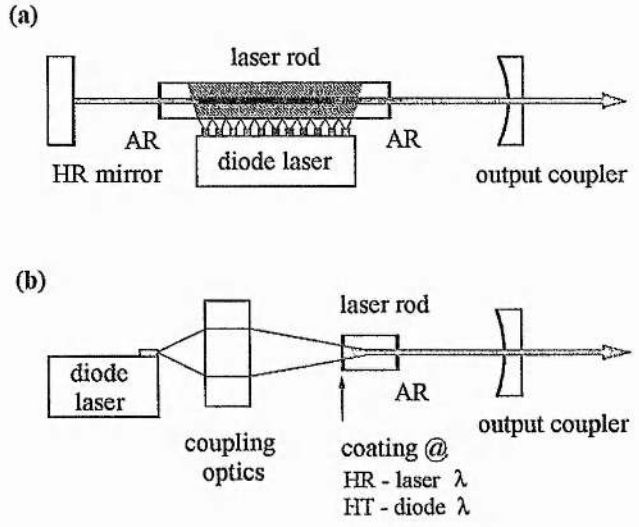

Fig. 2.6.1. Schematic diagrams of (a) side-pumped and (b) end-pumped solid-state lasers. HR: highly reflective coating, AR: anti-reflection coating.

In side-pumped geometry, the diode array is closely coupled into the laser mode volume through the side of laser crystal with minimal or no optics. Laser material absorbs a significant fraction of the pump light in a short length. The gain may be similarly estimated to be [35]

$$G = \exp[\frac{P}{h\nu_p} \cdot \frac{\tau\sigma_e}{(\eta l_a)^2}] \quad (2.4)$$

where η is the absorption coefficient and ηl_a is the effective absorption length for the laser gain. Gain profile in side-pumped configuration can be achieved in a large volume within the laser crystal. However, side-pumped lasers have lower efficiency (typically ~10%) since the laser mode only uses certain portion of the pumped volume.

In order to achieve a good matching between the pump volume and the laser mode, techniques such as the multiple diode lasers incorporated pumping, laser mode multi-passing in the pump volume (e.g. zig-zag resonator geometry [1][66], and tightly folded resonator (TFR) [67]) are used. High average output powers can also be obtained in these configurations because multiple pump sources can be incorporated and the pump energy can be coupled into a relative large volume of laser mode.

In general, end-pumped lasers have a higher efficiency than side-pumped lasers, especially for TEM_{00} operation, because of the improved overlap of pump volume and laser mode. Side-pumped lasers are more readily scaled to higher powers because of the large volume of the gain medium available for pumping [35]. However, due to the availability of high power diode arrays and various diode light coupling schemes, the differences between end pumping and side pumping have gradually diminished. End-pumped systems have reached 90 W output power [68], while the efficiency of side-pumped systems has increased to 30% [69][70].

B. The Nonplanar Ring Oscillator - A Design Example

To fully realise the reliability and utility of diode-pumped lasers, other issues concerning the stability and lifetime of laser components should also be taken into account. Kane and Byer's nonplanar ring oscillator (NPRO) [62], as shown schematically in Fig. 2.5.2, sets such an example. The NPRO consists of an integrated element that combines the function of the active medium, the ring resonator and the unidirectional element. It is fabricated from a single Nd:YAG crystal in the form of a multi-faceted

prism. The closed laser mode path is provided by total internal reflection and a coated spherical surface within the crystal. End-pumped by a diode laser, a good spectral and spatial mode match is achieved. Unidirectional oscillation is realised by using the Faraday effect in the active element. Stability of the component mounting and the element temperature are also incorporated in the NPRO design. Unique characteristics are manifested in this design in terms of high stability in the frequency (150 kHz/sec jitter) and output intensity (0.2% rms), extremely small spectral linewidth (less than 10 kHz), high efficiency (60% optical conversion efficiency) and small dimensions. However, being an integrated optical device, it is very sensitive to thermal effects inside the crystal. Even though good spectral and spatial match is achieved by diode laser pumping, there is still a certain amount of non-radiation heat that is dissipated. Thermal effects prevent NPRO from being a high power device [71].

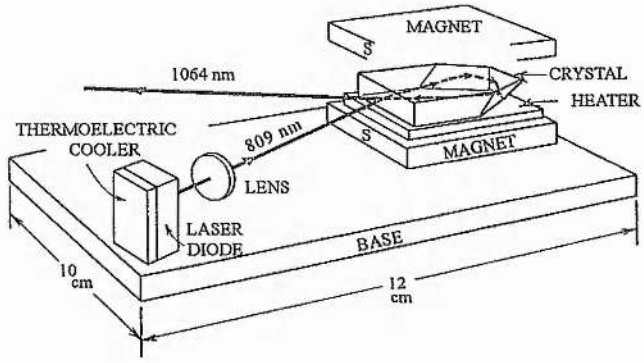

Fig. 2.6.2. Schematic diagram of non-planar ring oscillator (Kane and Byer 1985)

Other approaches in achieving high efficiency in moderate and high power regime are also quite successful [72][73]. In order to achieve the high amplitude and frequency stability of the NPRO in high-power regime, the technique of injection seeding is used to control the temporal mode behaviour of solid-state lasers. The NPRO is used as a master oscillator. By seeding a CW beam into a slave oscillator, a stable single-line output is converted into a powerful Q-switched pulse or high power CW output.

2.7 Single-Frequency Operation

CW single-frequency operation is not normally associated with solid-state lasers. In a standing wave cavity, spatial hole-burning in the homogeneous active medium allows several longitudinal modes to oscillate, and higher pump powers encourage this oscillation. A simple approach for obtaining single-longitudinal-mode (SLM) operation of a laser is to reduce the length of the gain medium and cavity length so that there is only one longitudinal mode in the range of gain spectrum. Up to 20 mW SLM output have been obtained using this method [74]. Another variation is that the cavity is long enough to support several longitudinal modes but the pump power is controlled below the multi-mode operation threshold [75]. Intracavity etalons are also used in some systems to obtain SLM operation [76], but with a reduced efficiency. As alternatives, both twisted mode resonators and travelling wave resonators can eliminate spatial hole burning effects in the gain medium. Wallmeroth and Peuser have obtained 255 mW SLM output from a diode-pumped twisted-mode laser [77]. By using a monolithic twisted mode cavity [63], they have obtained 80 mW SLM output with a linewidth of 10 kHz under the free-running operating condition. A successful travelling wave resonator has been designed by Kane and Byer [62] as discussed before. The ring resonator and the unidirectional mechanism are integrated inside the monolithic crystal without any additional loss. Up to 900 mW have been obtained from this configuration [78]. Recently, by applying a new pump geometry, over 2 W of single-frequency output with a slope efficiency of 60% has been obtained from a monolithic ring device [71]. However, the output power is limited to values below 3 W in this design due to the thermal lensing limitation.

In the high-power regime, single-frequency operation has also been realised in a ring [79] or master/slave configuration using the injection locking-technique [80]. As high as 15 W single-frequency output has been achieved by injection-locking a high-power diode-pumped solid-state laser to a NPRO [81]. This is a promising technique to realise stable single-frequency operation in the high-power regime.

Another method to achieve SLM operation is based on the use of a birefringent filter inside the laser cavity [82]. It has been demonstrated in our intracavity frequency doubling system that by using a birefringent KTP crystal and a Brewster plate as a novel intracavity birefringent filter, SLM can be attained in the SHG output from a standing wave cavity. When we place the KTP crystal away from the beam waist in the cavity to reduce the SHG conversion efficiency, 1 W SLM fundamental output can be obtained [83], as will be described in section § 3.9.

2.8 Frequency Doubling

Efficient harmonic generation can be attained in diode-pumped solid-state lasers due to their higher spatial and spectral brightness. This nonlinear frequency conversion technique can extend the emission spectrum of diode-pumped lasers from the infrared into the visible and ultraviolet region. The high-peak-power output from Q-switched or mode-locked Q-switched diode-pumped lasers can be efficiently frequency doubled in a single pass through a nonlinear crystal. However, efficient frequency doubling of CW lasers requires resonant enhancement techniques. One obvious approach is to place the nonlinear crystal inside the laser cavity so as to take advantage of the high internal circulating power. While fundamental power is resonating inside the laser cavity, SHG is coupled out of the resonator by nonlinear crystal. High conversion efficiencies have been attained using this scheme. Baer has discovered that large intensity fluctuations of SHG output and longitudinal-mode instabilities are exhibited in a diode-pumped Nd:YAG laser with KTP as an intracavity doubling crystal [84]. He has suggested that these instabilities arise from coupling of the longitudinal modes of the laser oscillator by sum-frequency generation in the nonlinear crystal. The so called "green problem" is exhibited in many other intracavity doubled systems. However, these intensity fluctuations can be eliminated by reducing the longitudinal-mode coupling factors [85] or by single-frequency operation [84][86].

A. External Resonant Frequency Doubling

An alternative to resonant doubling is external resonant doubling, in which the fundamental beam is mode-matched into a second cavity with a nonlinear crystal inside. The external cavity can be resonant at either the SHG or at the fundamental wavelength. This method requires a highly stable, narrow linewidth and single-frequency diode-pumped laser as the input source and active tuning of the external cavity. The system developed by Kozlovsky *et al.* [86] has combined the advantages of the single-frequency NPRO with the stability of a monolithic resonator fabricated onto a lithium niobate nonlinear crystal. By locking the external resonator to the laser frequency, 30 mW of green output has been generated with 56% optical conversion efficiency. This design offers the advantages of keeping optical elements out of the laser oscillator, independently optimising the harmonic generation process, and yielding stable and single-frequency second-harmonic output. Using external resonant cavity for frequency doubling, as high as 6.5 W has been obtained in an 18 W, CW injection-locked sing-frequency Nd:YAG laser system [87].

B. Intracavity Frequency Doubling

Back to the intracavity frequency doubling, this scheme is attractive for its simplicity, high conversion efficiency, and less stringent requirements on the laser performance in the fundamental wavelength. Stable operation has been observed in various designs. Liu and Oka have used an intracavity quarter-wave plate to eliminate longitudinal-mode coupling and achieved 3.5 W stable green output [88]. An alternative way of avoiding intensity fluctuations is to use a single-frequency laser. Ring resonant configurations have been employed [89]. Combining the unidirectional device and the nonlinear crystal in the cavity, single-frequency fundamental wave can be converted into single-frequency SHG. In standing-wave cavities, twisted mode technique [90] or intracavity etalon [84] has been used to achieve single-frequency operation in the frequency-doubling scheme. A disadvantage of above methods is that the laser outputs are highly sensitive to the losses introduced by the insertion of intracavity elements.

Diode-pumped microchip laser has also been used for frequency doubling [91] with limited output power.

We have taken the novel birefringent filter technique first proposed by Nagai and et.al [92] and extended its implementation to higher powers. It has proved to be an efficient way to achieve single-frequency operation in second harmonic generation. The intracavity birefringent filter may be formed by a Brewster plate and a birefringent nonlinear crystal. In a standing-wave cavity, it allows SLM oscillation by providing minimal loss for a selected mode, while providing much higher additional losses on other adjacent modes. Using this technique, a few milliwatts of intracavity frequency-doubled SHG have been previously obtained in diode-pumped Nd:YAG lasers [92][93] and Nd:YVO_4 laser [94]. In our laboratory, we have demonstrated over 1 W of SLM green output from a diode-pumped Nd:YLF laser. Although the long-term stability of the SHG output remains to be improved, this technique is a reliable and efficient method to generate low-noise SLM green light and needs to be fully exploited.

2.9 Rate Equations for End-Pumped Lasers

To analyse Nd:YLF laser action, we start with the rate equations in which the spatial variation of both the pump beam and the cavity mode are taken into account. Expressions for the population inversion within the laser material as well as the gain of a particular cavity mode are developed. Further, the threshold and the slope efficiency of four-level end-pumped laser are derived and analysed. This approach essentially follows that of Kubodera and Otsuka [95] as well as others [96] [97], and the following assumptions are made in deducing expressions for the lasing transition of $^4F_{3/2}$–$^4F_{11/2}$ (see Fig. 2.2.1). (1) All pump atoms relax rapidly from pump band to the $^4F_{3/2}$ manifold. (2) The relative populations of the Stark splittings within a manifold can be given by a Boltzmann distribution at all times. (3) The lower laser level has a very short lifetime (< 10 ns) and so has no significant population. (4) Losses are low so that the low gain approximation is valid. However, this approach is in general for four-level laser systems.

A. The Four-Level End-Pumped Laser Model

Considering a four-level laser operating in a single TEM_{00} mode, we have rate equations for the upper and lower laser levels with spatial hole burning included [97]:

$$\frac{dN_2(r,z)}{dt} = f_2 R r_p(r,z) - \frac{N_2(r,z) - N_2^0}{\tau_2} - f_2 \frac{\sigma \cdot c \cdot [N_2(r,z) - N_1(r,z)]}{n} \cdot S \cdot s_o(r,z) \tag{2.5a}$$

and

$$\frac{dN_1(r,z)}{dt} = -\frac{f_1 N_2(r,z)}{f_2 \tau_{21}} - \frac{N_1(r,z) - N_1^0}{\tau_1} + f_1 \frac{\sigma \cdot c \cdot [N_2(r,z) - N_1(r,z)]}{n} \cdot S \cdot s_o(r,z) \tag{2.5b}$$

where f_i is the fraction of ions in the energy manifold actually found in level N_i, σ is the stimulated emission cross-section, n is the index of refraction at the laser wavelength, c is the speed of light in vacuum, S is the total cavity photon number, τ_i is the decay rate from the i_{th} level, N_1^0 and N_2^0 are the populations of the lower laser level and the upper laser level manifold at thermal equilibrium, respectively. $s_o(r,z)$ and $r_p(r,z)$ are the spatial distribution functions for the fundamental cavity mode and the pump beam, respectively. Here, the fundamental cavity mode simply refers to the mode that is nearest in frequency to the line centre of the laser material. R is the rate at which pump photons enter the laser cavity to excite ions into the upper laser manifold and is given by [95]

$$R = \eta_p P_p / h\nu_p \tag{2.6}$$

where P_p is the optical pump power, $h\nu_p$ is the pump photon energy, and $\eta_p = 1 - \exp(-\alpha_p \cdot l_{rod})$ is the fraction of incident pump power absorbed in a crystal of length l_{rod} with pump absorption coefficient α_p. Factor f_1 and f_2 account for the thermal distribution of atoms in the upper and lower manifolds at equilibrium. The fractional

population of a given level within a given manifold is given by the Boltzmann distribution expression

$$f_j = \frac{\exp(-\Delta E_j/kT)}{1+\sum_i \exp(-\Delta E_i/kT)} \tag{2.7}$$

For the R_2 level of Nd^{3+} ions in YAG, this gives $f_2 = 0.40$; and for the lower Y_3 level, $f_1 = 0.187$. On the right hand side of Eq. (2.5a), the first term describes the pump relation to populate the upper laser level, the second term describes spontaneous emission, and the third term accounts for the stimulation emission and absorption process between the upper and the lower laser level. Similar arguments can be used to derive all of the terms in Eq. (2.5b).

The pumping process in this model is assumed to have unity quantum efficiency. The spatial distribution of the pump beam and fundamental laser cavity mode are given by $r_p(r,z)$ and $s_o(r,z)$, respectively. These terms are normalised such that [97]

$$\int_{rod} r_p(r,z)\cdot dV = \int_{cavity} s_o(r,z)\cdot dV = 1 \tag{2.8}$$

For a Gaussian beam entering a medium with absorption coefficient α_p, and where the intracavity mode is a standing wave, it follows that [97]

$$r_p(r,z) = \frac{2\alpha_p}{\pi\cdot w_p^2(z)\cdot\left[1-\exp(-\alpha_p l_{rod})\right]}\cdot\exp\left(\frac{-2r^2}{w_p^2(z)} - \alpha_p\cdot z\right) \tag{2.9}$$

$$s_i(r,z) = \frac{4}{\pi\cdot w_l^2(z)\cdot l_{cav}}\cdot\exp\left(\frac{-2r^2}{w_l^2(z)}\right)\cdot\sin^2(k_i z). \tag{2.10}$$

Here, l_{rod} is the geometrical length of the laser rod, l_{cav} is the optical length of the laser cavity, k_i is the propagation constant for mode i, and $w_p(z)$ and $w_l(z)$ are Gaussian

beam spot sizes for the pump beam and laser cavity mode, respectively. Both the pump beam and cavity modes are modelled as Gaussian beams. The pump beam decays along the z-axis as it is absorbed by the laser crystal, and there is a standing wave intensity variation along the z-axis for the cavity field. The period of the standing-wave is dependent upon the propagation constant of the cavity mode k_i. It is possible to account for different pump distributions, higher-order transverse modes, non-collinear pump beam and cavity mode, or diffraction of the beams within the gain medium by assuming the proper forms for $r_p(r,z)$ and $s_o(r,z)$. However, these end-pumped devices typically operate in a TEM_{oo} mode, and the threshold is not highly dependent on the exact form for $r_p(r,z)$ as long the power can be described as being within some radius $r = w_p$ [98].

The corresponding rate equation for the total number S of photons in the cavity is

$$\frac{dS}{dt} = 0 = \frac{\sigma \cdot c \cdot S}{n} \int_{rod} \Delta N(r,z) \cdot s_0(r,z) dV - \frac{S}{\tau_q} \qquad (2.11)$$

[97], where $\tau_q = 2nl_{cav}/c\delta$ is the un-pumped cavity photon lifetime ($\delta = L + T$ represents the total cavity losses where L is the round-trip loss and T is the output transmission). Note that the gain integral of Eq. (2.11) is carried out over the pumped volume of the laser material rather than the cavity volume. This is done because the population inversion, $\Delta N(r,z)$, is zero outside the pumped volume. Eq. (2.11) describes the cavity photon number which is proportional to the circulating power and the output power. The first term on the right hand side of the equation is an increase in photon number due to stimulated emission and the second term is a decrease in photon number due to losses. An assumption in Eq. (2.11) is that only one transverse mode is considered. This is reasonable for end-pumped systems. As long as the pumped volume lies within the volume of the TEM_{oo} cavity mode, single transverse mode operation is easily achievable.

B. Threshold

In the steady state, $dN_1/dt = dN_2/dt = 0$, and Eq. (2.5a) and (2.5b) can be combined to form the population inversion density $\Delta N(r,z) = N_2(r,z) - N_1(r,z)$:

$$\Delta N(r,z) = \frac{f_2(B + AN_1^0)}{Af_2 + \gamma_2} - N_1^0 \tag{2.12}$$

where $A = \frac{\sigma \cdot c}{n} S \cdot s_o(r,z)$, $B = R \cdot r_p(r,z)$ and $\gamma_i = 1/\tau_i$. Here, we have used the approximation that $\gamma_2 \approx \gamma_{21}$ and $Af_1 << \gamma_1$. The general expression for $\Delta N(r,z)$ derived from the rate equations is given by [97]

$$\Delta N(r,z) = \frac{f_2[(f_1A + \gamma_1) + A\gamma_1 N_1^0] \cdot [f_1A + \gamma_1 - f_1(A + \gamma_{21}/f_2)]}{(f_1A + \gamma_1) \cdot [(f_1A + \gamma_1)(f_2A + \gamma_2) - f_1A(f_2A + \gamma_{21})]} - \frac{\gamma_1 N_1^0}{(f_1A + \gamma_1)} \tag{2.13}$$

Equation (2.12) can be substituted into Eq. (2.11) to determine the amount of pump power needed to sustain a given laser output power. At threshold, the cavity photon number is $S = 0$, and the expression for ΔN_{th} is

$$\Delta N(r,z)_{th} = \frac{f_2 B}{\gamma_2} - N_1^0 \tag{2.14}$$

The threshold pump power can then be found by solving Eq. (2.11)

$$P_{th} = \frac{\pi \cdot h\nu_p \gamma_2}{2f_2\eta_p} \cdot \left(w_l^2 + w_p^2\right) \cdot \left(\frac{\delta}{2\sigma} + l_{rod} N_1^0\right) \tag{2.15}$$

The round-trip cavity loss δ can also be written in terms of $T + \delta_f + \alpha_i l_{rod}$ where T is the output transmission loss, δ_f is the rest of extrinsic loss not dependent on the length of the gain medium such as scattering at interfaces and Fresnel reflections, and $\alpha_i l_{rod}$

represents losses which are proportional to the gain medium length such as impurity absorption and bulk scattering. The term $l_{rod}N_1^0$ is the re-absorption loss of gain material due to the lower laser level population. However, in the four-level laser this term is approximately 0 and Eq. (2.15) reduces to

$$P_{th} = \frac{\pi \cdot h\nu_p \cdot \delta}{2 \cdot \sigma_e \tau_2 \eta_p \cdot 2} \cdot \left(w_l^2 + w_p^2\right) \tag{2.16}$$

where $\sigma_e = f_2\sigma$ represents the effective emission cross-section. For minimum threshold, it is desirable to make the pump beam waist small in order to maximise the peak inversion at $r = 0$, where the laser intensity is highest, and it is desirable to make the laser waist small so that photons that are spontaneously emitted into the laser mode will encounter a high pump excitation over the entire laser mode. Eq. (2.16) also shows that the threshold power is dependent on spectroscopic and material properties $\left(h\nu_p, \eta_p, \sigma_e, \tau_2, \delta\right)$, and geometry factors through the overlap integral and design choices $\left(l_{rod}, T\right)$. The geometry factors and design choices are not independent of each other nor independent of the spectroscopic properties. It would be useful to find the scaling of minimum threshold with spectroscopic and material dependence so that a figure of merit for threshold can be formulated which allows side-by-side comparison of laser materials. Threshold is inversely proportional to the quantity $\sigma_e \eta_p \tau_2$; thus, these spectroscopic properties need to be included in a figure of merit. Spectroscopic properties also ultimately determine the minimum value for the geometry factor in Eq. (2.16). It is obvious that Eq. (2.16) gives a non-physical answer of a minimum threshold of 0 for infinitely tight focusing. To account for diffraction, the average of values of w_o^2 and w_p^2 in the gain medium can instead be used [99]. These minimum average values are proportional to l_{rod}. The value of l_{rod} is a design choice, but to absorb a reasonable fraction of the pump radiation, l_{rod} should be on the order of or greater than $1/\alpha_p$. On the other hand, if l_{rod} is too long, the average spot sizes in the crystal increase which consequently increase threshold. Hence, there is an optimum

crystal length l_0 that minimises the threshold in terms of incident pump power and can be obtained by solving

$$\alpha_p \exp(-\alpha_p l_0)\cdot\left(\delta_f + T + \alpha_i l_0\right) - \alpha_i = 0 \qquad (2.17)$$

As a numerical example, when we use the values $\delta_f = 0.005$, $T = 0.05$, $\alpha_p = 32\ cm^{-1}$ (a value of Nd:YLF material absorption coefficient at 797 nm // c polarised light), and $\alpha_i = 0.005$ (a value of characteristics of Nd:YLF crystal), the optimum crystal length l_0 is 1.9 mm.

In standing-wave cavity, the gain of additional cavity mode may be calculated by replacing the spatial distribution of the fundamental mode, $s_o(r,z)$, with that of an adjacent longitudinal mode. The spatial distribution of these additional modes will have a modified cross-section coefficient σ_i which is determined by the bandwidth of the laser material. Also, the propagation constant k_i will change because of the change in wavelength from the fundamental mode. The new wavelength will differ by a multiple of the cavity free spectral range, $\Delta\nu_{cav} = c/2l_{cav}$, where l_{cav} is the optical length of the laser cavity. Thus, the threshold for a cavity mode with frequency $\nu_m = \nu_o \pm m\cdot\Delta\nu_{cav}$ will be reached when the following equation holds true [97]:

$$\frac{c\cdot\sigma_m}{n}\int_{rod}\Delta N(r,z)\cdot s_m(r,z)\cdot dV = \frac{1}{\tau_q}. \qquad (2.18)$$

Considering the spatial hole burning effect in the homogeneous gain medium and the effect of energy diffusion, the additional possible cavity modes can attain certain spatial gain distribution. For $l_{cav} >> l_{rod}$ where l_{rod} is in the order of pump absorption length, it is obvious that the phase relation between the expected longitudinal modes are

$$\nu_m = \nu_o \pm \frac{m\cdot c}{2\cdot n\cdot l_{rod}} \qquad (2.19)$$

However, such a phase relationship is true only if the laser material has larger gain bandwidth such as that of Nd:YLF, and the FWHM of the lasing transition determines the number of longitudinal modes.

C. Slope Efficiency

Operation above threshold can also be treated by a rate equation analysis. Above threshold, the rate equations must account for stimulated emission and the circulating intensity in the cavity. In steady state, the population inversion density is described by Eq. (2.12). Substituting Eq. (2.12) into Eq. (2.11), we have

$$f_2 R\tau_2 \cdot \int \frac{r_p(r,z)\cdot s_o(r,z)\cdot dV}{1+\frac{f_2 c\sigma\cdot\tau_2}{n}Ss_o(r,z)} = \frac{1}{2\sigma\cdot l_{rod}}\left[\delta + 2\alpha_l l_{rod}\int \frac{s_o(r,z)\cdot dV}{1+\frac{f_2 c\sigma\cdot\tau_2}{n}Ss_o(r,z)}\right] \tag{2.20}$$

where the substitution $-\sigma N_1^0 = \alpha_l$ has been made. The left-hand-side of this equation represents the gain terms and the right-hand-side represents the loss terms. There are two components to the loss term. One is the round-trip total cavity loss δ, and the other is the re-absorption at the laser wavelength due to lower laser level population. In the four-level laser, since $N_1^0 = 0$, Eq. (2.20) can be reduces to

$$f_2 R\tau_2 \cdot \int \frac{r_p(r,z)\cdot s_o(r,z)\cdot dV}{1+\frac{f_2 c\sigma\cdot\tau_2}{n}Ss_o(r,z)} = \frac{\delta}{2\sigma\cdot l_{rod}} \tag{2.21}$$

We consider only the case where $w_p \le w_o$, since for $w_p > w_o$ the slope efficiency and therefore overall efficiency decrease rapidly. For this case, the integral in the equation can be solved analytically if $\left(w_o/w_p\right)^2$ is an integer:

$$\frac{-2f_2R_2\tau_2 p}{\pi\cdot w_o l_{rod}}\cdot\left[\sum_{k=1}^{p}\frac{(-1)^k}{(p-k+1)(2S/S')^k}+\frac{(-1)^{p+1}}{(2S/S')^{p+1}}\cdot\ln\left(1+\frac{2S}{S'}\right)\right]=\frac{\delta}{2\cdot\sigma\cdot l_{rod}} \tag{2.22}$$

where $p=\left(w_o/w_p\right)^2$ and $S'=\frac{n\pi\cdot w_o^2 l_{rod}}{f_2 c\sigma\tau_2}$ which is equivalent to a saturation photon number.

To obtain the output power in terms of the input power, S needs to be solved in terms of R from Eq. (2.22). The number of output photons per unit time, S_0, and the output power P_0 are given by [95]

$$P_0=h\nu\cdot S_0=h\nu\cdot\frac{TSc}{2nl_{rod}}. \tag{2.23}$$

Thus, the output power versus pump power near the threshold in the fundamental transverse-mode oscillation is [95]

$$P_{out}=\frac{(1-R)}{\delta}\cdot\frac{h\nu}{h\nu_p}\eta_p\left(P-P_{th}\right) \tag{2.24}$$

where $(1-R)=T$ and R is the reflectivity of the output mirror. The slope efficiency is

$$\eta=\eta_p\frac{h\nu}{h\nu_p}\frac{T}{\delta} \tag{2.25}$$

For high slope efficiency, one needs to maximise η_p and minimise $\delta_f+\alpha_i l_{rod}$. High slope efficiency can still be achieved by increasing T if other losses are not low, but this is undesirable because it increases threshold.

Reference

[1] R. L. Byer, "Diode laser pumped solid-state lasers", *Science*, vol. 239, pp. 742-747, 1988.

[2] T. Y. Fan and R. L. Byer, "Diode laser-pumped solid-state lasers", *IEEE J. Quant. Electron.*, vol. 24, pp. 895-912, 1988.

[3] R. Newman, "Excitation of the Nd^{3+} fluorescence in $CaWO_4$ by recombination radiation in GaAs", *J. Appl. Phys. Lett.*, vol. 34, pp. 437, 1963.

[4] R. J. Keyes and T. M. Quist, "Injection luminescent pumping of $CaF_2:U^{3+}$ with GaAs diode lasers", *Appl. Phys. Lett.*, vol. 4, pp. 50-52, 1964.

[5] M. Ross, "YAG laser operation by semiconductor laser pumping", *Proc. IEEE*, vol. 56, pp. 196-197, 1968.

[6] F. W. Ostermayer, Jr., R. B. Allen, and E. G. Dierschke, "Room-temperature cw operation of a $GaAs_{1-x}P_x$ diode-pumped YAG:Nd laser", *Appl. Phys. Lett.*, vol. 19, pp. 289-292, 1971.

[7] L. C. Conant and C. W. Reno, "GaAs laser diode pumped Nd:YAG laser", *Appl. Opt.*, vol. 13, pp. 2457-2458, 1974.

[8] H. G. Danielmeyer and F. W. Ostermayer, Jr., "Diode-pump-modulated Nd:YAG laser", *J. Appl. Phys.*, vol. 43, pp. 2911-2913, 1972.

[9] K. Washio, K. Iwamoto, K. Inoue, and F. Saito, "Room temperature cw operation of an efficient miniaturised Nd:YAG laser end-pumped by a superluminescent diode", *Appl. Phys. Lett.*, vol. 29, pp. 720-722, 1976.

[10] F. W. Ostermayer, Jr., "LED end-pumped Nd:YAG lasers", *IEEE J. Quant. Electron.*, vol. 13, pp. 1-6, 1977.

[11] M. Saruwatari, T. Kimura, T. Yamada, and J. Nakano, "$LiNdP_4O_{12}$ laser pumped with an $Al_xGa_{1-x}As$ electroluminescent diode", *Appl. Phys. Lett.*, vol. 27, pp. 682-684, 1975.

[12] J. Stone and C. A. Burrus, "Neodymium-doped fibre lasers: room temperature cw operation with an injection laser pump", *Appl. Opt.*, vol. 13, pp. 1256-1258, 1974.

[13] W. Streifer, D. R. Scifres, G. L. Harnagel, D. F. Welch, J. Berger, and M. Sakamoto, "Advances in diode laser pumps", *IEEE J. Quant. Electron.*, vol. 24, pp. 883-894, 1988.

[14] J. Berger, D. F. Welch, D. R. Scifres, W. Streifer, and P. S. Cross, "High power, high efficiency neodymium:ytterbium aluminium garnet laser end pumped by a laser diode array", *Appl. Phys. Lett.*, vol. 51, pp. 1212, 1987.

[15] L. E. Zapata, R. J. Beach, C. Brent Dane, P. Reichert, L. A. Hackel, "Advanced diode-pumped, Nd:YAG slab laser for soft X-ray projection lithography", *Tech. Dig. CLEO'94*, paper CThC4.

[16] D. Golla, S. Knoke, W. Schone, G. Ernst, M. Boale, A. Tunnermann, H. Welling, "300-W cw diode laser side-pumped Nd:YAG rod laser", *Opt. Lett.*, vol. 20, pp. 1148-1150, 1995.

[17] T. Y. Fan, G. J. Dixon, and R. L. Byer, "Efficient GaAlAs diode-laser-pumped operation of Nd:YLF at 1.047 μm with intracavity frequency doubling", *Opt. Lett.*, vol. 11, pp. 204, 1986.

[18] T. M. Baer, D. F. Head, and P. Gooding, " High peak power Q-switched Nd:YLF laser using a tightly folded resonator", *Tech. Dig. CLEO'90*, paper CMF2.

[19] W. J. Kozlovsky, T. Y. Fan, and R. L. Byer, "Diode-pumped continous wave Nd:glass laser", *Opt. Lett.*, vol. 11, pp. 788-790, 1986.

[20] T. Y. Fan, "Solid-state laser pumped by advanced diode laser source", *Tech. Dig. OSA Annual Meeting*, 1990, paper TVV4.

[21] S. Basu, and R. L. Byer, "Average power limits of diode laser-pumped solid state lasers", *Appl. Opt.*, vol. 29, pp. 1765, 1990.

[22] R. Scheps, "Efficient laser diode pumped Nd lasers", *Appl. Opt.*, vol. 28, pp. 89, 1989.

[23] R. A. Fields, M. Birnbaum, and C. L. Fincher, "15.8% efficient diode laser end pumped Nd:YVO_4 laser", *Tech. Dig. CLEO'88*, paper PD3.

[24] D. P. Cafey, R. A, Utano, and T. H. Allik, "Diode array side-pumped neodymium-doped gadolinium scandium gallium garnet rod and slab lasers", *Appl. Phys. Lett.*, vol. 56, pp. 808, 1990.

[25] D. Scarl, R. Burnham, S. R. Bowman, and D. J. Feldman, "Diode-pumped 1.34 μm Nd^{3+}:$YAlO_3$ laser", *Appl. Opt.*, vol. 27, pp. 5005, 1988.

[26] L. D. Schearer, P. Tin, "Laser performance and tuning characteristics of a diode-pumped Nd:$YAlO_3$ laser at 1083 nm", *Opt. Commun.*, vol. 71, pp. 170, 1989.

[27] J. T. Lin, M. Y. Hwang, S. Rowe, "Close-coupled diode-pumped NYAB green laser", *OSA Annual Meeting 1990*, paper PDP26.

[28] T. Y. Fan, G. Huber, R. L. Byer, and P. Mitzscherlich, "Spectroscope and diode-laser-pumped operation of Tm,Ho:YAG", *IEEE J. Quant. Electron.*, vol. 24. pp. 924. 1988.

[29] H. Hemmati, "2.07 μm cw diode-laser-pumped Tm,Ho:$YLiF_4$ room-temperature laser", *Opt. Lett.*, vol. 14, pp. 435, 1989.

[30] P. J. M. Suni and S. W. Henderson, "1 mJ/pulse Tm:YAG laser pumped by a 3 W diode laser", *Opt. Lett.*, vol. 16, pp. 817-819, 1991.

[31] P. J. M. Suni and G. H. Gates, "Damage-free operation of a 2.5 mJ Tm:YAG laser pumped by 3 W room-temperature diode laser", *Tech. Dig. CLEO'91*, paper CPDP12.

[32] J. A. Hutchinson, D. P. Caffey, C. F. Schaus, and C. W. Trussel, "Diode pumped eyesafe erbium glass laser", *Tech. Dig. CLEO'90*, paper CPDP19.

[33] B. I. Denker, A. A. Korchangin, V. V. Osiko, S. E. Sverchkov, T. H. Allik, and J. A. Hutchinson, "Diode-pumped and FTIR Q-switched laser performance of novel Yb-Er glass", *OSA Proce. on Advanced Solid-state lasers,* vol. 20, pp. 148-150, 1994.

[34] P. Lacovara, C. A. Wang, H. K. Choi, R. I. Aggarwal, and T. Y. Fan, "Room-temperature InGaAs diode-pumped Yb:YAG laser", *Opt. Lett.*, vol. 16, pp. 1089-1091, 1991.

[35] Walter Koechner, "Solid-State Laser Engineering", *Springer-Verlag, Third Revised Edition,* 1992.

[36] R. Scheps, B. M. Gately, J. F. Myers, J. S. Krasinski, and D. F. Heller, "Alexandrite laser pumped by semiconductor lasers", *Appl. Phys. Lett.*, vol. 56, pp. 2288, 1990.

[37] K. Kubodera and K. Otsuka, "Efficient $LiNdP_4O_{12}$ laser pumped with a laser diode", *Appl. Opt.*, vol. 18, pp. 3882, 1979.

[38] H. Po, F. Hakimi, R. J. Mansfield, R. P. Tumminelli, B. C. McCollum and E. Snitzer, "Neodymium fibre lasers at 0.905, 1.06, and 1.4 μm", *J. Opt. Soc. Am. A3*, pp. 103, 1986.

[39] M. Nakazawa, Y. Kimura, and K. Suzuki, "Efficient Er^{3+}-doped optical fibre amplifier pumped by a 1.48 μm InGaAsP laser diode", *Appl. Phys. Lett.*, vol. 54, pp. 295, 1989.

[40] R. Allen and L. Esterowitz, "CW diode pumped 2.3 μm fiber laser", *Appl. Phys. Lett.*, vol. 55, pp. 721, 1989.

[41] J. N. Carter, R. G. Smart, D. C. Hanna, and A. C. Tropper, "CW diode-pumped operation of 1.97 μm thulium doped fluorozirconate fibre laser", *Electron. Lett.*, vol. 26, pp. 599, 1990.

[42] R. Allen, L. Esterowitz, and R. J. Ginther, "Diode-pumped single-mode fluorozirconate fibre laser from the $^4I_{11/2}$ - $^4I_{13/2}$ transition in erbium", *Appl. Phys. Lett.*, vol. 56, pp. 1635, 1990.

[43] C. A. Millar, S. C. Fleming, and M. H. Hunt, "Single transverse mode operation at 1345 nm wavelength of a diode laser pumped neodymium ZBLAN multimode fiber laser", *IEEE Photon. Tech. Lett.*, vol. 2, pp. 415, 1990.

[44] D. Pichler, D. Craven, N. Kwong, and H. Zarem, "Laser-diode-pumped red and green up-conversion fibre lasers", *Electron. Lett.*, vol. 29, pp. 1857, 1993.

[45] D. Piehler, D. Craven, "InGaAs laser-pumped green upconversion fibre laser" *Tech. Dig. CLEO'94*, paper CMK4.

[46] E. K. Mwarania, L. Reekie, J. Wang, and J. S. Wilkinson, "Low-threshold monomode ion-exchanged waveguide lasers in neodymium-doped BK-7 glass", *Electron. Lett.* vol. 26, pp. 1317, 1990.

[47] H. Aoki, O. Maruyana, and Y. Asahara, "Glass waveguide laser", *IEEE Photon. Tech. Lett.*, vol. 2, pp. 459, 1990.

[48] S. J. Field, D, C. Hanna, A. C. Large, D. P. Shepherd, A. C. Tropper, P. J. Chandler. P. D. Townsend, and L. Zhang, "An efficient, diode-pumped, ion implanted Nd:GGG planar waveguide laser", *Opt. Commun.*, vol. 86, pp. 161-166, 1992.

[49] S. J. Field, D, C. Hanna D. P. Shepherd, A. C. Tropper, P. J. Chandler. P. D. Townsend, and L. Zhang, "Ion implanted Nd:YAG crystal waveguide lasers", *IEEE J. Quant. Electron.*, vol. 27, pp. 428-433, 1992.

[50] F. Krausz. L. Turi, C. Kuti, and A. J. Schmidt, "Active mode-locking of laser by piezoelectrically induced diffraction modulation", *Appl. Phys. Lett.*, vol. 56, pp. 1415, 1990.

[51] S. Basu and R. L. Byer, "Continuous-wave mode-locked Nd:glass laser pumped by a laser diode", *Optics Lett.*, vol. 13, pp. 458-460, 1988.

[52] S. J. Walker, H. Avramopoulos, and T. Sizer, "Compact mode-locked solid-state laser at 0.5 GHz and 1 GHz repetition rates", *Optics Lett.*, vol. 15, pp. 1070-1072, 1990.

[53] G. T. Maker and A. I. Ferguson, "Frequency-modulation mode-locking of a diode pumped Nd:YAG laser", *Optics Lett.*, vol. 14, pp. 788-790, 1989.

[54] G. T. Maker and A. I. Ferguson, "Mode-locking and Q-switching of a diode-pumped neodymium-doped Yttrium Lithium-fluoride laser", *Appl. Phys.*, vol. 54, pp. 403-405, 1989.

[55] D. W. Hughes, J. R. M. Barr, and D. C. Hanna, "Mode-locking of a diode-laser-pumped Nd:glass laser by frequency-modulation", *Optics Lett.*, vol. 16. pp. 147-149, 1991.

[56] J. Goodberlet, J. Jacobson, J. G. Fujimoto, P. A. Schulz, and T. Y. Fan, "Self-starting additive-pulse mode-locked diode-pumped Nd:YAG laser", *Optics Lett.*, vol. 15, pp. 504-506, 1990.

[57] G. P. A. Malcolm, P. F. Curley, and A. I. Ferguson, "Additive-pulse mode-locking of a diode pumped Nd:YLF laser", *Optics Lett.*, vol. 15, pp. 1303-1305, 1990.

[58] F. Krausz, Ch. Speilmann, T. Brabec, E. Wintner, and A. J. Schmidt, "Self-starting additive-pulse mode locking of a Nd:glass laser", *Optics Lett.*, vol. 15. pp. 1082-1084, 1990.

[59] S. J. Keen and A. I. Ferguson, "Subpicosecond pulse generation from an all solid-state laser", *Appl. Phys. Lett.*, vol. 55, pp. 2164, 1989.

[60] C. L. Fincher and R. Fields, Research work in Aerospace Corp. (El Segundo, CA), 1994

[61] T. J. Kane, A. C. Nilsson, R. L. Byer, "Frequency stability and offset locking of a laser diode-pumped Nd:YAG monolithic nonplanar ring oscillator," *Optics Lett.*, vol. 12, pp. 175-177, 1987.

[62] T. J. Kane and R. L. Byer, "Monolithic, unidirectional single mode Nd:YAG ring laser", *Optics Lett.*, vol. 10, pp. 65-67, 1985.

[63] K. Wallmeroth, "Monolithic integrated Nd:YAG laser", *Optics Lett.*, vol. 15, pp. 903-905, 1990.

[64] A. L. Schawlow and C. H. Townes, "Infrared and optical masers", *Phys. Rev.*, vol. 112, pp. 1940-1949, 1958.

[65] B. Zhou, T. J. Kane, G. J. Dixon, and R. L. Byer, "Efficient, frequency-stable laser-diode-pumped Nd:YAG laser", *Opt. Lett.*, Vol. 10, pp. 62-64, 1985.

[66] H. Injeyan, R. J. St. Pierre, J. G. Berg, R. C. Hilyard M. E. Weber, M. G. Wickham, R. Senn, G. Harpole, C. Florentino, F. Groark, and M. Farey, "Diode array-pumped kilowatt laser development" *Tech. Dig. CLEO'94*, paper CThC1

[67] T. M. Baer, D. F. Head, P. Gooding, G. J. Kintz, and S. Hutchison, "Performance of diode-pumped Nd:YAG and Nd:YLF laser in a tightly folded resonator configuration", *IEEE J. Quant. Electron.*, vol. 28, pp. 1131-1138, 1992.

[68] S. C. Tidwell, J. G. Seamans, M. S. Bowers, "Highly efficient 60 W TEM_{00} CW diode-end-pumped Nd:YAG laser", *Opt. Lett.*, vol. 18, pp. 116-118, 1993.

[69] D. Welford, D. M. Rines, B. J. Dinerman, "Efficient TEM_{00}-mode operation of a laser-diode side-pumped Nd:YAG laser", *Opt. Lett.*, vol. 16, pp. 1850-1852, 1991.

[70] U. J. Greiner, H. H. Klingenberg, D. R. Walder, C. J. Flood, H. M. van Driel, "Diode-pumped Nd:YAG laser using reflective pump optics", *Appl. Phys. B*, vol. 58, pp. 393-395, 1994.

[71] I. Freitag, P. Rottengatter, A. Tunnermann, H. Welling, "Amplitude and frequency stabilisation of diode-pumped miniature ring lasers oscillating at high output power", *Tech. Dig. CLEO'94,* paper CTuP1.

[72] C. Rahlff, M. H. Dunn, B. D. Sinclair, and W. Sibbert, "High-power, end-pumped effects and application in Nd:YLF at 1047 and 1321 nm", *Tech. Dig. CLEO'94*, paper CThG4.

[73] M. D. Selker, R. S. Afzal, J. L. Dallas, A. W. Yu, "Diode laser pumped, diode laser seeded Nd:YLF regenerative amplifier" *Tech. Dig. CLEO'94*, paper CThC7

[74] J. J. Zayhowski and A. Mooradian, "Single-frequency microchip Nd lasers", *Opt. Lett.*, vol. 14, pp. 24-26, 1989.

[75] C. Pedersen, P. L. Hansen, T. Skettrup, and P. Buchhave, "Diode-pumped single-frequency Nd:YVO_4 laser with a set of coupled resonatros", *Opt. Lett.*, vol. 20, pp. 1389-1391, 1995.

[76] P. Nachman, J. Munch, and R. Yee, "Diode-pumped frequency-stable, tuneable continuous-wave Nd:glass laser", *IEEE J. Quant. Electron.*, vol. 26, pp. 317, 1990.

[77] K. Wallmeroth and P. Peuser, "High power, CW, single-frequency TEM_{00}, diode-laser-pumped Nd:YAG laser", *Electron. Lett.*, vol. 24, pp. 1086, 1988.

[78] E. A. P. Cheng, T. J. Kane, "High-power single-mode diode-pumped Nd:YAG laser using a monolithic nonplanar ring resonator", *Optics Lett.*, vol. 16, pp. 478, 1991.

[79] R. J. Shine Jr., A. J. Alfrey, R. L. Byer, "20W CW single-frequency diode-laser pumped Nd:YAG slab laser", *Tech Dig. CLEO'95*, paper CMD6.

[80] I. Freitag, and H. Welling, "Investigation on amplitude and frequency noise of injection-locked diode-pumped Nd:YAG lasers", *Appl. Phys. B*, vol. 58, pp. 537-543, 1994.

[81] D. Golla, I. Freitag, H. Zellmer, W. Schone, I. Kropke, and H. Welling, "15W single-frequency operation of a CW diode laser-pumped Nd:YAG ring laser", *Optics Commun.*, vol. 98, pp. 86, 1993.

[82] A. Abramoviei, "Minimal Nd:YAP laser configuration with single frequency output", *Optics Comm.*, vol. 61, pp. 401-404, 1987.

[83] J. Zhang, Experiment work in J. F. Allen Physics Research laboratories.

[84] T. Baer, "Large-amplitude fluctuations due to longitudinal mode coupling in diode-pumped intracavity-doubled Nd:YAG lasers", *J. Opt. Soc. Amer. B*, vol. 3, pp. 1175-1180, 1987.

[85] M. Oka and S. Kubota, "Stable intracavity doubling of orthogonal linearly polarised mode in diode-pumped Nd:YAG laser", *Opt. Lett.*, vol. 13, pp. 805-807, 1988.

[86] W. J. Kozlovsky, C. D. Nabors, and R. L. Byer, "Second harmonic generation of a CW diode-pumped Nd:YAG laser using an externally resonant cavity", *IEEE J. Quant. Electron.*, vol. 24, pp. 913, 1988.

[87] S. T. Yang, C. C. Pohalsk, E. K. Gustafsun, R. L. Byer, R. S. Feigelson, R. J. Raymakers, and R. K. Ronte, "6.5-W, 532nm radiation by CW resonant external-cavity second-harmonic generation of an 18-W Nd:YAG laser in LiB_2O_5" *Optics Lett.*, vol. 16, pp. 1493-1495, 1991.

[88] L. Y Liu, M. Oka, W. Wiechmann, and S. Kubota, "Longitudinally diode-pumped continuous-wave 3.5 W green laser", *Optics Lett.*, vol. 19, pp. 189-191, 1994.

[89] R. Scheps and J. Myers, "Laser diode pumped half-watt single frequency ring laser", *OSA Ann. Meet., 1989 Technical Digest Series*, vol. 18, pp.218.

[90] D. W. Anthon, D. L. Sipes, T. J. Pier, and M. R. Sessl, "Intracavity doubling of CW diode-pumped Nd:YAG laser with KTP", *IEEE J. of Quant. Eletron.*, vol. 28, pp. 1148-1157, 1992.

[91] N. Mackinnon and B. D. Sinclair, "A laser diode array pumped, Nd:YVO_4/KTP, composite material microchip laser", *Optics Comm.*, vol. 105, pp. 183-187, 1994

[92] H. Nagai, M. Kume, I. Ohta, H. Shimiza, and M. Kazumura, "Low-noise operation of a diode-pumped intracavity-doubled Nd:YAG laser using a Brewster plate", *IEEE J. Quant. Electron.*, vol. 28, pp. 1164-1167, 1992.

[93] T. Y. Fan, "Single-axial mode, intracavity doubled Nd:YAG laser", *IEEE J. Quant. Electron.*, vol. 27, pp. 2091-2093, 1991.

[94] T. Carry, T. Honda, and H. Matsumoto, "Frequency stabilization of a diode-laser pumped CW Neodymiun Yttrium Vanadate intracavity-doubled solid-state laser", *Jpn. J. Appl. Phys.*, vol. 32, pp. 3185-3186, 1993.

[95] K. Kubodera and Otsuka, "Single-transverse-mode $LiNdP_4O_{12}$ slab waveguide laser", *J. Appl. Phys.*, vol. 50, pp. 653-659, 1979.

[96] T. Y. Fan and R. L. Byer, "Modeling and CW operation of a quasi-three-level 946 nm Nd:YAG laser", *IEEE J. of Quant. Eletron.*, vol. 23, pp. 605-612, 1987.

[97] P. F. Mead, S. P. Bush, and C. C. Davis, "Single-mode operation of diode-pumped Nd:YAG lasers by pump-beam focusing", *IEEE J. of Quant. Eletron.*, vol. 30, pp. 2902-2906, 1994.

[98] D. G. Hall, R. J. Smith, and R. R. Rice, "Pump-size effects in Nd:YAG lasers", *Appl. Opt.*, vol. 19, pp. 3041-3043, 1980.

[99] M. J. F. Digonnet and C. J. Gaeta, "Theoretical analysis of optical fiber laser amplifiers and oscillators", *Appl. Opt.*, vol. 24, pp. 333-342, 1985.

Chapter 3

DIODE-PUMPED ND:YLF LASER

3.1 Introduction

The criteria for the design of the frequency-doubled Nd:YLF laser are set primarily by the requirements on the pump beam for the successful operation of CW OPOs. Based on the KTP and the LBO nonlinear material, CW OPOs that are able to oscillate in doubly-resonant cavity (including dual-cavity) or pump enhanced singly-resonant cavity require a pump source with: (1) the capability of delivering ~ 1 W output power in green spectrum; (2) single-frequency radiation which have sub-MHz linewidth and low frequency jitters; (3) both short-term and long-term intensity stability. As discussed in § 2.6, due to the spatial hole burning effect, stable single-frequency operation can not be achieved in a standing-wave cavity. The conventional ring configurations are able to provide single-frequency operation, but the unidirectional devices also introduce undesirable losses and complexity in the processes of intracavity second harmonic generation. The nonplanar ring oscillator (NPRO), however, is limited by its low power level, and it is a costly device due to the crystal cutting. In addition, to obtain the single-frequency SHG output, an external resonant enhanced optical cavity is needed for frequency doubling.

To simplify the pump laser, an intracavity frequency-doubled diode-pumped Nd:YLF laser has been designed and constructed to meet the basic requirements for the CW OPO experiment. In this design, we utilise the diode-end-pumped geometry and standing-wave cavity in order to achieve an overall efficient system, and use the novel birefringent filter technique to obtain the single-frequency SHG output. According to the experimental results, such a single-frequency green laser appears to be a successful system, and we have hence demonstrated a new approach in the frequency-doubled

diode-pumped solid-state laser designs. In this chapter, we discuss the considerations and the design of the diode-pumped Nd:YLF laser and describe the experimental performance of the laser at the fundamental wavelength.

3.2 General Considerations

In order to achieve the required output power, 20 W CW GaAlAs linear array laser diode has been procured as the laser pump source. To obtain a higher optical-to-optical conversion efficiency and a near diffraction limit TEM_{oo} output, diode-end-pumped geometry has been employed. Considerations of efficiency in this laser design have been concentrated on obtaining a good spectral and spatial overlap between the diode array pump region and the laser cavity mode in the Nd:YLF crystal. The 20 W diode laser is designed to be temperature tuned as a 797 nm pump source so that good pump absorption can be attained. The water cooling loop capable of dissipating 80-W nonradiation heat is built for the 20 W diode laser. Furthermore, a thermo-electric cooler is used to finely control the diode operating temperature. A major drawback of the diode array for the spatial mode overlap is its emission aperture. The conventional coupling optics can not transfer the diode arrays into a small cross-sectioned circular pump beam. However, compared with the fibre coupling, free space optics offer a simple and efficient way for diode pumping. In our design, we have used the combination of a cylindrical lens and a spherical condenser lens to collect and couple the diode array into the Nd:YLF crystal. An elliptical pump beam cross section of 3:1 ratio has been produced a few millimetres in front of the coupling optics. In order to efficiently couple the pump beam into the laser mode, the Nd:YLF crystal, which is HR coated at 1047 nm and AR coated at pump wavelength on one end surface, is placed immediately in front of the coupling optics.

Since the pump light can only be an elliptical cross-sectioned beam, in order to match the laser mode into the same shape as the pump volume inside the Nd:YLF crystal, a folded cavity is designed and constructed. An additional benefit from such cavity

configuration is that a circular tightly focused beam waist could be produced in the other folded cavity arm so that the nonlinear crystal can take the advantage of the high intracavity power density to achieve a high nonlinear conversion efficiency. In addition, the green beam generated in the two directions can be combined into a single output by a dichroic end mirror. Moreover, the flexibility of setting of the fold angle, and changing the separations of the mirrors and the Nd:YLF crystal in the cavity could allow a complete compensation of the astigmatic thermal lensing effect which is induced by the diode pump. This folded resonator design results in the diode light being efficiently coupled into the laser mode in one cavity arm, and the laser fundamental energy being efficiently converted into the SHG and coupled out of the cavity in the other arm.

Several issues in relation to the design of high power and efficient diode-pumped Nd:YLF lasers are discussed in detail in this chapter. Thermally induced beam distortion in the high power end-pumped Nd:YLF material is investigated. The computer modelling of the folded linear cavity has been set up to analyse the cavity mode characteristics and the resonator stability range. Several cavity configurations are compared for their laser performance. Finally the spectral characteristics of the diode-end-pumped Nd:YLF lasers are discussed.

3.3 Nd:YLF Material for Diode Pumping

A. Nd:YLF Material

Nd:YLF is attractive as an active material for use in solid-state lasers because of several properties that are very different from those of Nd:YAG. Firstly, since it is uniaxial material, one can select one of the two different naturally polarised wavelengths for each transition simply by using an intracavity polariser. The strong natural birefringence of the material also swamps the effect of thermally induced birefringence observed in optically isotropic hosts like YAG. Secondly, Nd:YLF is suitable for the generation of high-power Q-switched pulses due to its long fluorescence lifetime and high energy density storage

capability. Finally, weak thermal lensing effect in the Nd:YLF crystal provides additional advantage over continuous-wave or mode-locking laser operations of Nd:YAG.

The optical-absorption and stimulated-emission study of Nd^{3+} in the uniaxial crystal yttrium lithium fluoride ($YLiF_4$ or YLF) [1][2][3] shows several main absorption lines lying at 792, 797 and 806 nm which can be excited by the AlGaAs diode lasers. These absorption lines of Nd:YLF are typically a few nanometers wide, thus can be well matched by the emission spectrum of diode arrays. The uniaxial Nd:YLF crystal exhibits strong polarisation dependent absorption transitions and fluorescence due to the anisotropic crystal field. Fig 3.3.1 [3] shows the same orientationally resolved absorption spectra in the wavelength range of AlGaAs laser diode pumping. The σ ($E \perp c$) and the π ($E // c$) polarised absorption spectra of Nd:YLF at room temperature are plotted in Fig. 3.3.1.(a) and (b) respectively.

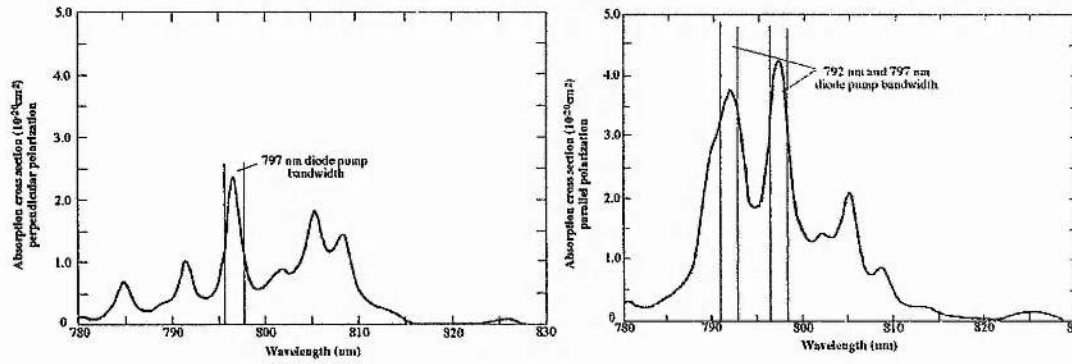

(a) (b)

Fig. 3.3.1. Absorption cross section for Nd in YLF at room temperature. (a) for light polarized perpendicular to c-axis; (b) for light polarized parallel to c-axis.

The two straight lines in the figures stand for the spectral width of diode arrays used as pump. The fact that the absorption cross section of Nd:YLF is much larger for the polarised incident light parallel to the c-axis of YLF crystal than that for the light perpendicular to the c-axis can also be considered as an advantage for linearly polarised diode light pump. Other advantages of Nd:YLF material in favour of diode-pump are relatively large thermal conductivity allowing efficient nonradiation heat extraction, and less strong thermal lensing effect allowing high beam quality. The thermal-mechanical

properties of Nd:YLF, however, are not as good as those of Nd:YAG. The low hardness and the inferior thermal fracture limit of this material may cause breakage in crystal mounting and high-power end-pumping processes.

Stimulated-emission oscillations have been realised in both $^4F_{3/2}$ - $^4I_{11/2}$ and $^4F_{3/2}$ - $^4I_{13/2}$ manifolds transitions of Nd:YLF by diode pump, corresponding to 1.05 μm and 1.31 μm laser output. The peak $^4F_{3/2}$ - $^4I_{11/2}$ cross sections are 14.2 x 10^{-20} cm^2 at 1.053 μm (σ-polarisation) and 19.6 x 10^{-20} cm^2 at 1.047 μm (π-polarisation). As a consequence, operation on the 1.047 μm occurs in the absence of wavelength or polarisation selective elements in the resonator at a certain pump level.

B. Spectroscopic Properties for Laser Operation

It is observed in the experiment that Nd:YLF has the most efficient absorption line at 792 nm for the polarised light parallel to the c-axis of Nd:YLF crystal. Substantially lower laser threshold has been shown in our experiment by using the diode laser as 792 nm pump source rather than 797 nm pump source. The experiment set up is an end-pumped linear cavity with a 5% output coupler mirror (detailed description are in § 3.7). The diode pump wavelength can be tuned either to 792 nm or to 797 nm by controlling the diode bar temperature. Fig. 3.3.2 shows the output power characteristics of diode-pumped Nd:YLF laser operating at 1.047 μm under 792 nm and 797 nm diode array pumps. As shown in the figure, the oscillation threshold of the laser at 792 nm pump is about half the value of that at 797 nm pump, while there are not significant differences between the two slope efficiencies. This behaviour can be understood by analysing the threshold Eq. (2.16) and the slope efficiency Eq. (2.25) developed in chapter 2. In the experiment, the diode-pumped Nd:YLF laser starts to lase before the diode laser reaches its lasing threshold. Thus, at threshold, Nd:YLF laser is actually pumped by LEDs light instead of diode laser light. Fig. 3.3.1.(b) shows that the Nd:YLF material absorption bandwidth of 792 nm line is much wider than that of 797 nm line. So much more incident LEDs pump light are absorbed when the laser is pumped at 792 nm resulting in $\overline{\eta}_p\big|_{792(LED)} > \overline{\eta}_p\big|_{797(LED)}$ (where $\overline{\eta}_p$ is the average pump absorption efficiency

when considering a wide pump spectral band), and gives $P_{th}|_{792} < P_{th}|_{797}$. However, as the diode driving current increases, the diode laser soon reaches its threshold and the emitting radiation becomes much narrower in spectral width. Because $\overline{\eta}_p|_{792(laser)} \approx \overline{\eta}_p|_{797(laser)}$ under the condition of diode laser pump, we have the two slope efficiencies $\eta_{792} \approx \eta_{797}$ which is shown in Fig. 3.3.2.

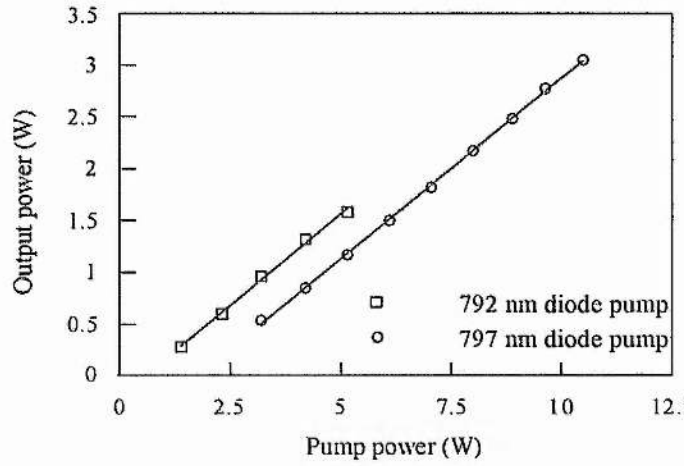

Fig. 3.3.2. Output power from Nd:YLF laser versus diode pump power at 792 nm and 797 nm diode wavelength.

The laser output power with respect to the absorption cross section in the pump spectrum range of 792 - 797 nm and the crystal temperature change have also been investigated. By varying the diode pump wavelength and keeping the same pump power, dramatic output power change in Fig. 3.3.3 shows that the laser output power is a function of the pump wavelength. From Eq. (2.24), the laser output power is dependent on the pump light absorption efficiency. However, since the absorption cross section of Nd:YLF material changes rapidly with the pump spectrum, a dramatic output power change could occur when pump wavelength is tuned. Fig. 3.3.4 shows the laser output power versus the Nd:YLF crystal temperature change at 10-W diode pump. Such a behaviour indicates that the material effective emission cross section σ_e is a function of temperature. In general, by varying the diode pump wavelength, significant change of the absorption of the diode pump light results in the laser efficiency difference. They

manifest in the laser threshold and the output power both varying with the pump wavelengths. On the other hand, since the laser oscillation occurs on the same $^4F_{3/2}$ - $^4I_{11/2}$ transition of Nd:YLF, as long as the diode light is absorbed in the laser rod, the laser slope efficiency should not be affected. In Fig. 3.3.4, the slight output power drop of 0.01% per °C with the rising laser material temperature is mainly because the cross section of the laser transition is temperature dependent.

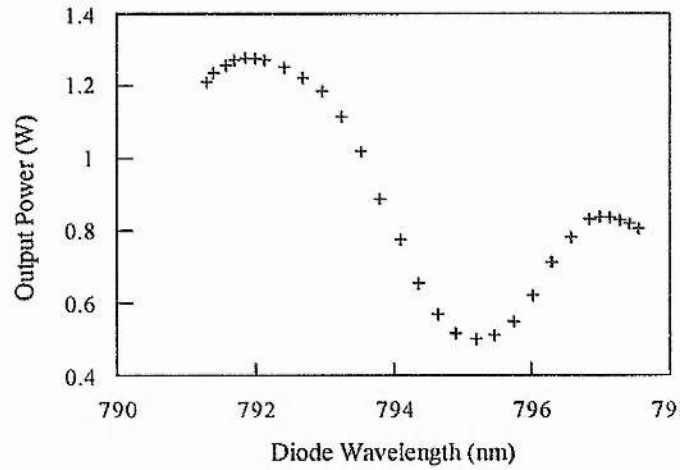

Fig. 3.3.3. Output power from Nd:YLF laser versus diode pump wavelength at 4-W pump.

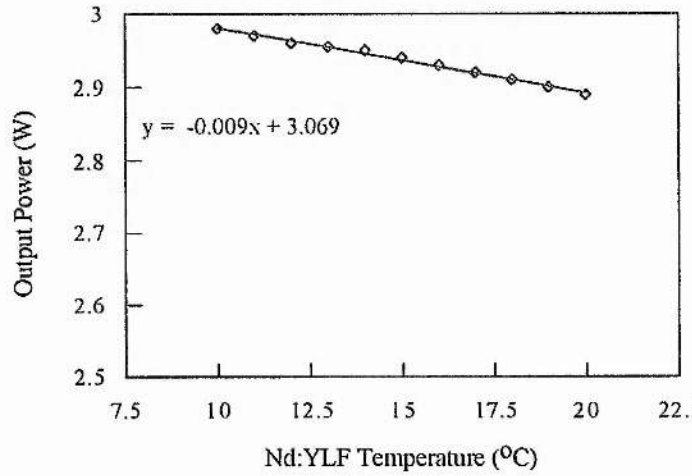

Fig. 3.3.4. Output power from Nd:YLF laser versus Nd:YLF crystal temperature at 10-W diode pump.

C. Nd:YLF Crystal Orientation

In the our experiments of Nd:YLF lasers, we have used 1% Nd^{3+} at. wt. Nd:YLF crystal (supplied by Litton). Considering the operating wavelengths and thermal effects in the Nd:YLF crystal, a crystallographic a-axis cut, 4-mm long Nd:YLF crystal cube was procured. This orientation provides access to both lasing wavelengths by intracavity polarisation selection. This may be done by simply rotating the intracavity polariser or inserting an additional half-wave plate between the polariser and the slab. Another benefit of this orientation is that the thermally induced birefringence is overwhelmed by its natural birefringence by 2 ~ 3 orders of magnitude, thus the thermal depolarisation problem can be greatly reduced in Nd:YLF material. The laser crystal in the experiment is mounted in a water-cooled brass heatsink for the conventional edge-cooling. A layer of Indium foil is wrapped around the crystal to ensure a good thermal contact between the crystal and the brass heatsink. By aligning the c-axis of Nd:YLF parallel to the polarisation direction of diode laser, the crystal absorbed about 90% of the diode-laser pump light at 797 nm.

3.4 Thermal Effects in Nd:YLF with Diode Pumping

Generally, the thermal lensing effect is considered to be quite weak in lamp-pumped Nd:YLF lasers. Even in a 7 kW lamp-pumped Nd:YLF laser system [4], the thermal dioptric power for the π-polarisation light is ~ 0.35 m^{-1} in the plane parallel to c-axis, and is ~ 1.1 m^{-1} in the perpendicular plane. Comparing with the strong thermal lensing effect in the Nd:YAG crystal, such behaviour is mainly because the negative thermal lensing induced by the indices change dn/dT of Nd:YLF has been partially weakened by the thermal expansion in the material. In high power lamp-pumped or diode side-pump Nd:YLF lasers, the negative anisotropic thermal indices change (- 4.3 x 10^{-6} K^{-1} for π-polarisation and - 2.0 x 10^{-6} K^{-1} for σ-polarisation) and the anisotropic thermal expansions (13 x 10^{-6} for π-polarisation and 6 x 10^{-6} for σ polarisation) of the Nd:YLF material present a negative lensing effect with a strong astigmatism for the π-polarised

light. Meanwhile, they present a negative lensing in the plane parallel to c-axis and a positive lensing in the orthogonal plane for the σ-polarised light. However, thermally induced effects are different in diode-end-pumped Nd:YLF lasers, since strong astigmatic positive lensing are exhibited for the light of both polarisations. In Rines' end-pumped Nd:YLF laser [5], with 10 W diode pump power, the Nd:YLF exhibits an astigmatic positive lens with a focal length of 40 cm in the horizontal plane (parallel to c-axis) and a 100 cm focal length in the orthogonal plane, both for the π-polarised light.

A. End Surface Deformation

The thermal distortion of laser crystal is the sum of three independent effects, namely the thermally induced variation of the refractive index dn/dT, the thermally induced birefringence due to the photo-elastic effect, and the expansion of the laser material with increasing temperature [6]. In the case of a homogeneously pumped Nd:YLF laser medium, the thermal distortion can be expressed as a resulting thermal lens with focal length f [6]

$$f = \frac{KA}{P_a}\left(\frac{1}{2}\frac{dn}{dT} + \frac{\alpha \cdot r_o(n_o - 1)}{L}\right)^{-1} \tag{3.1}$$

where K is the thermal conductivity, A is the geometric cross section of the laser material, and P_a is the pump power that is transformed to heat in the crystal. α is the thermal coefficient of expansion, and n_o is the index of refraction. The radius and the length of the laser material are r_o and L, respectively. Here, the thermally induced birefringence is negligible because of the strong natural birefringence of Nd:YLF. In lamp-pumped or diode side-pumped Nd:YLF lasers, the temperature gradient is approximately uniformly distributed along the medium and in the transverse radial cross section. From Eq. (3.1), the negative thermal index change dn/dT is the major factor responsible for the thermal lensing effect. In the end-pumped lasers, the diode pump light is deposited into the crystal in a volume more or less the same size as the cavity mode in the active medium. Most of the diode light is absorbed in the end surface area which gives non-

uniform temperature distributions along the crystal as well as in the crystal radial cross section. Eq. (3.1), however, could not be applied in the case.

Several analytical models of the end-pump thermal lensing effect have been discussed previously [6][7][8], but they have not considered the end-surface deformation effect which is believed as the major factor of the cause of the positive lensing in Nd:YLF material. From the previous results of thermally induced lensing effects [4][5][9], it could be concluded that the thermal lensing or the thermal beam distortion in the end-pumped Nd:YLF material arise from two major contributions: 1) the medium refractive index variation caused by temperature gradients; 2) the thermal expansion inside the crystal (especial the end-surface curvature deformation). As a consequence of the end-pumped geometry, especially of those with a highly reflective coating on the pump surface, the curved surface of Nd:YLF material (or a curved surface mirror), which is formed of the deformation of the flatten end-surface, overwhelms the negative index change and leads to a strong positive lensing effect. In addition, being an anisotropic material, Nd:YLF has two different expansion coefficients for the a-axis and c-axis, as well as two refractive indexes and two thermal lensings for the π- and σ-polarised light. These properties give rise to the thermal beam distortion effect exhibiting polarisation dependence with astigmatic forms.

In the end-pumped geometry, the thermal induced effect of Nd:YLF crystal is also strongly dependent on the diode pump intensity profile in the gain medium. When the crystal cooling condition is defined, at certain pump power, the distribution of temperature, stress and strain is established. Based on these data, the space-resolved changes of the refractive index are determined considering thermal dispersion, surface deformation, and strain-induced birefringence. In the case of the high reflectivity mirror on one end surface of the crystal, optical path can be integrated along the laser mode in the gain medium. Comparing the differences of optical paths in the laser mode cross section, the thermal induced beam distortion which exhibits in the surface deformation and the thermal lensing effect can be predicted. However, since the diode pump light profile in

our experiment is the overlapped diode arrays with a high astigmatism, it is difficult to use a simple model to simulate the pump beam profile in the active medium.

B. Thermal Distortion Measurements

Instead of theoretical modelling, we have conducted a series of experiments to evaluate the thermal beam distortion in relation with the pump power, the pump volume and the edge cooling condition. To simulate the effect of beam distortion to a simple astigmatic lens, a corresponding relationship between the diode pump power and the thermal beam distortion has been established through the following measurement. The collimated π-polarised TEM_{00} HeNe beam is incident into the Nd:YLF crystal from the opposite end to the pumped surface. The spot size of the back reflection beam has been measured at several positions away from the crystal. The value of the thermal focal length has been obtained by fitting the data. Fig. 3.4.1 shows the measured values of dioptric power as a function of the pump power in the plane parallel to the c-axis and the plane perpendicular to the c-axis for π-polarised light. However, these values are measured under non-lasing condition, the actual values of dioptric power will show some different values due to the difference of thermal condition.

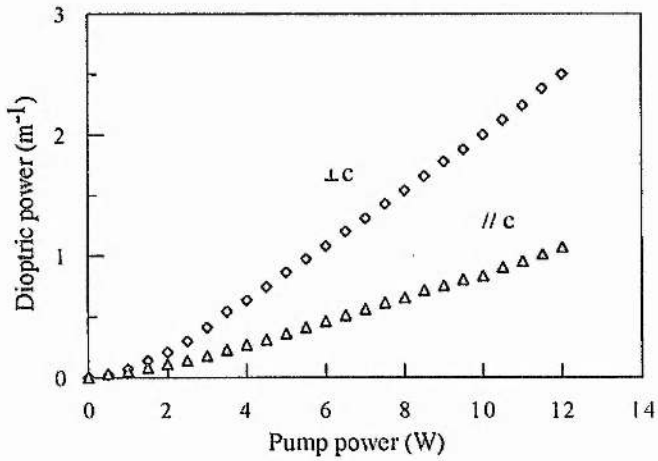

Fig. 3.4.1. The dioptric power of thermal beam distortion in Nd:YLF versus the diode pump power for p-polarized light in two orthogonal planes.

Astigmatism of thermal beam distortion is illustrated in the figure. With 10-W pump light, the thermal beam distortion approximately corresponds to a astigmatic positive lens. For π-polarised light, it has a focal length of 50 cm in the plane parallel to the c-axis, and a focal length of 150 cm in the orthogonal plane. This simple astigmatic lens simulation is largely in good agreement with the actual thermal beam distortion and provides thermal effect data for the laser cavity design. Similar measurements have been conducted to evaluate the thermal beam distortion for σ-polarisation. Longer thermal lensing focal length has been obtained by fitting the data.

C. Thermal Fracture Limit

An additional issue associated with the high temperature gradient in the region of end-pumped surface of the crystal is the stress fracture of the Nd:YLF laser material. This thermal fracture has been observed in our experiments. It occurs in the pump region along the c-axis of Nd:YLF crystal. The fracture threshold for 792 nm pump is 10 W, while for 797 nm pump it is 20 W. The main reasons for the low thermal tolerance are believed to be as follows. a) Nd:YLF has a larger expansion coefficient along the a-axis than the c-axis. So the thermal stress is easier to reach the structure modules tolerate limit threshold in the plane perpendicular to a-axis. b) The diode pump light in our experiment are concentrated in a narrow stripe at the end surface of Nd:YLF crystal. The stripe is parallel to the c-axis leading to a high temperature gradient along the a-axis. In the design of the diode-pumped Nd:YLF laser, we have used the diode laser as a 797 nm pump source to achieve a relatively deep-depth pump absorption in the Nd:YLF crystal. Although 797 nm pump has less efficient pump absorption than 792 nm pump, it partially relaxes the critical stress in the Nd:YLF material.

The diode array coupling scheme is the crucial component responsible for the thermal fracture. It transfers the diode array energy into the pump beam intensity profile which largely decide the temperature distribution in the Nd:YLF crystal. Based on the present cylindrical and aspherical lens combination, the inter-position of diode coupling optics is optimum adjusted considering both the thermal fracture limit and the overlap

between the pump beam intensity profile and the laser mode in the gain medium. In addition, other diode light deliver scheme, e.g. fibre coupling and binary optics coupling, are also considered for the future design.

3.5 Diode Laser Pump and Coupling Optics

A. 20-W CW Diode Arrays

A Spectra-Diode Labs SDL-2460-S diode laser bar and an Opto Power OPC-A020-797.5-CS diode laser bar have been procured as pump sources for Nd:YLF laser. They are AlGaAs linear arrays laser diodes which emit up to 20-W CW radiation in 800 nm wavelength region. The commercial bar device consists of tens individual emitters with an aperture of 100 μm (or 200 μm) which are grown on a single 1-cm substrate. These emitters are multistripe gain-guided laser diode arrays and are electrical-driven in parallel. The output of the diode bar is predominately incoherent since there is no possibility of coupling between adjacent arrays. On the other hand, due to small material variations in the manufacturing stage, the spectral output of the diode bar exhibit 2 - 3 nm spectral bandwidth which is suitable to pump the absorption band of Nd^{3+} doped material.

Similar optical and electrical characteristics are exhibited in the two devices. Table 3.1 lists some of optical specifications and operating parameters of SDL and OPTO diode laser arrays. The specified wavelength of the diodes at room temperature (25.0 °C for SDL, and 27.5 °C for OPTO) is subject to a manufacturing tolerance of +/- 3 nm. However, the output wavelength of the device is designed to be temperature tuned to 797 nm to match a strong absorption line of Nd:YLF. The power conversion efficiency of these devices are typically 30%. Over the threshold, the light output versus drive current is quite linear up to the recommended maximum operating current. Low noise output are exhibited by these diodes. The polarisation ratio of these gain-guided diodes are typically 10:1 with the E vector in the plane of the diode junction.

As experimental references, both temperature coefficient of wavelength and the wavelength shift rate versus driving current have been measured. The measured

temperature coefficient of wavelength agrees with the specified value. However, large wavelength shift with the variation of the driving current in the Opto diode bar has been observed, as shown in Fig. 3.5.1. A scanning monochromator is used in this measurement. The temperature of the diode bar sub-mount is stabilised at 27.5 °C. By scanning the monochromator at different driving current, as high as 0.32 nm/A wavelength shift rate has been recorded. This large figure is believed to be partly due to the temperature gradient change between diode and the heatsink. As a result from Fig. 3.3.3, less than ± 1 °C diode temperature stability is required to keep the spectral match of diode output and the Nd:YLF peak absorption line so as to achieve a stable laser output. For above reasons, in order to keep the diode as a constant 797 nm pump source, the ambient temperature needs to be adjusted with the driving current in our experiments.

Table 3.1 Optical specifications and operating parameters of SDL and OPTO 20-W diode laser

PARAMETER	*SDL-3460-S GC019*	*OPC-A020-797.5-CS 00200903*
Threshold	9.2 A	7.15 A
I at 20W	31 A	30 A
Array length	1.0 cm	1.0 cm
Number of emitters	48	24
Emitter dimensions	100 μm x 1 μm	200 μm x 1 μm
Emitter centre to centre spacing	200 μm	390 μm
Wavelength centre	801 nm	797.5 nm
Emission bandwidth (FWHM)	2.1 nm	2.5 nm
Beam divergence (FWHM)	< 45° ⊥, < 10° //	< 45° ⊥, < 10° //
Temperature coefficient of wavelength	0.3 nm/°C	0.27 nm/°C
Wavelength shift rate versus drive current	0.2 nm/A	0.32 nm/A
Heatsink temperature @797 nm operation with 10 W pump	16 °C	29 °C
Resistance	0.0034 OHMS	0.0065 OHMS

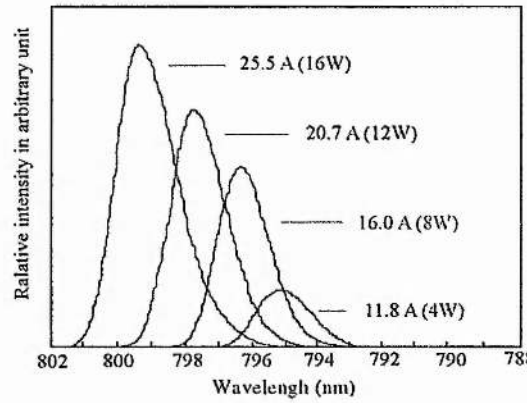

Fig. 3.5.1. Wavelength shift versus driving current of OPC-A20-797-CS diode bar at room temperature

B. The Current Supply and The Temperature Controller

Both diode lasers are driven by constant current supplies (type Kingshill CZ-115) which can give up to 40-A DC current with less than 20 mV rms ripple. Because of the requirement of using the diode lasers as 797 nm pump sources with ~ 15-W stable output power, the diode heatsinks are designed with the capability of up to 70 W heat dissipation and +/- 0.1^{0}C ambient temperature stability. Temperature control of the diode is achieved through the use of a thermoelectric (TE) cooler, which is sandwiched between the copper diode laser sub-mount and the tap-water-cooled cooper plate, see Fig. 3.5.2. The TE cooler and its temperature controller are Marlow Industry devices, types DT1089 and SE5020, respectively. Temperature sensing is via a bead thermistor located in the diode sub-mount. A thin sheet of Indium foil between the laser diode base and the heatsink and the Epoxy between the copper mounts and the TE cooler decrease the thermal resistance of these interfaces. Using this arrangement the ambient temperature can be accurately stabilised at any point in the range of 10 ^{o}C - 40 ^{o}C corresponding to 7.5 nm diode wavelength change. This temperature tolerance leaves a large space for the diode laser wavelength selection.

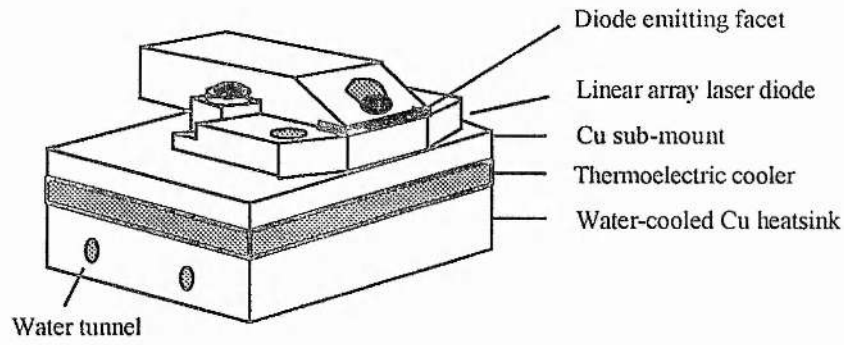

Fig. 3.5.2. GaAlAs linear array laser diode bar on heatsink

C. The Coupling Optics

The scaling of CW diode arrays to high power diode bar devices results in the highly divergent and astigmatic emission radiation output (~ 40^0 perpendicular to the diode array and ~ 10^0 along the array), and a rectangular emitting facet (10 mm x 1 μm). As pump sources for solid-state lasers, they are naturally used in side pump geometry with minimal coupling optics. These diode bars are difficult devices to use efficiently in end-pumped configurations. However, the recent development of optical delivery schemes utilise the potential of diode bars as efficient end-pump sources. Commercially, the diode arrays can be purchased with an optical fibre pigtail or fibre bundle [10]. In these package the radiation of high power diode bar are focused into an array of fibres by cylindrical microlens or gradient index (GRIN) lens. At the rear end, the fibres are joined into a circular bundle for end pumping. Clarkson and Hanna have developed a beam shaping technique [11] by using diode imaging optics and multiple reflection beam shaper. This technique combines the multiple parallel beams from the diode to produce a single spatial output through multi-reflecting process and allows a focused spot of less than 200 μm diameter with a relatively low beam divergence. To scale the end pump power, Lawrence Livemore National Laboratory (LLNL) research group have used cylindrical-microlens to collimate each emitting array individually, and an aspherical lens to focus them into the laser material[12]. Similarly, GRIN lens arrays have also been used in this

coupling scheme [13]. Other developed diode coupling schemes include binary optics collimating multistripe emission [14], lens duct coupling [15], and multiple diode laser arrays off-axially coupling with biconvex lens [16].

In our Nd:YLF laser design, we have used Shannon and Wallace's cylindrical and aspherical lens combination diode light coupling scheme [17] and its two lens variation. Although the pump volume is an overlap of multi-beamlets and has a relatively large elliptical spot in the cross section of the focus plane, the advantages of this optical system are high coupling efficiency, less optics, and the independence of the number of emitters along the 10-mm length of laser diode bar. Fig. 3.5.3.(a) illustrates the diode light coupling scheme used by Shannon et. al. The vertical plane in the experiment set up is parallel to the diode arrays junction plane. In this plane, beamlets which have a 10^{o} beam divergence are collimated by an aspherical condenser lens and overlapped at its focal spot area. The rod and the cylindrical lens with their cylindrical axis parallel to the diode emitter facet line collect and nearly collimate the diode light into the dimension parallel to the diode junction plane. A focused spot of 1.5 mm x 150 μm is finally produced roughly 5.8 mm beyond the final surface. The position of the rod lens and the cylindrical lens are finely tuned by minimising astigmatism at the final focus. The overlapped beamlets at the aspherical lens focal spot region rapidly divert in the vertical plane and slightly convert in the horizontal plane as shown in the figure. The rod lens is uncoated, while the remaining cylindrical and aspherical lenses are antireflection coated at 800 nm. With the diode bar operating at 10 W, 90% of diode light is incident upon the laser crystal, resulting in a maximum pump power density of 5 kW/cm^2. As a variation of the three lens system, the combination of a cylindrical lens and an aspherical lens, shown in Fig. 3.5.3.(b), requires less adjustment but produces an astigmatic focusing. In the horizontal plane, the cylindrical lens with 5 mm focal length is located approximately 3.5 mm from the diode junction. The lens collects the diode emission and yields a reduced divergent beam. The final focus in this dimension produced by the aspherical lens is beyond the focal point.

When placing the Nd:YLF crystal in the focus region, the pump beam profile in the medium is in the cross section of 1.5 mm x 0.5 mm.

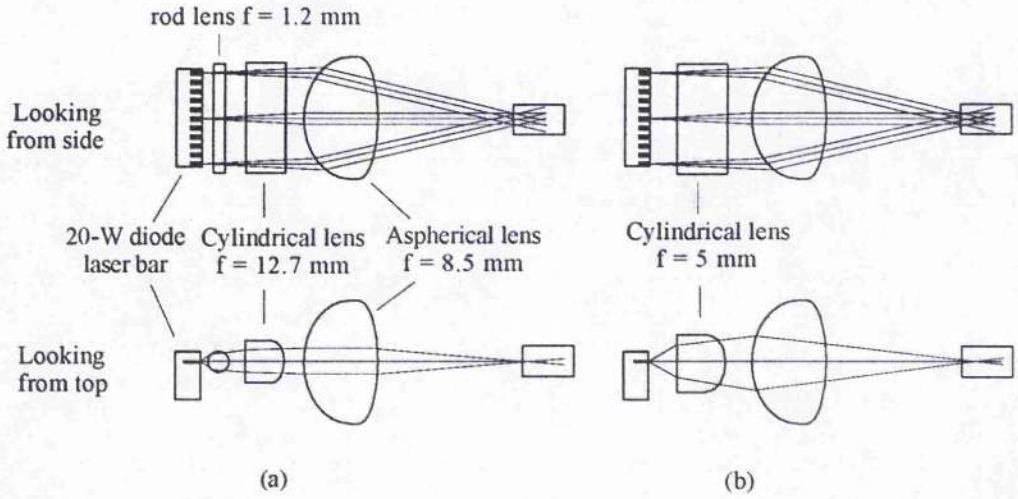

Fig. 3.5.3. End-pumping optics and ray-tracing plot. (a) rod lens, cylindrical lens, and aspherical lens combination; (b) cylindrical lens and aspherical lens combination. The optical traces represent the extreme rays from the three of the emitters within the laser bar.

Fig. 3.5.4 shows the image of the fluorescence profile in Nd:YLF crystal which also corresponds to the pump beam profile.

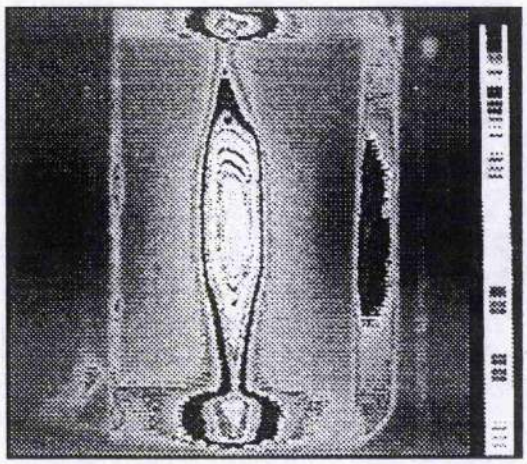

Fig. 3.5.4. Pump fluorescence in Nd:YLF crystal (image from CCD camera, looking from the opposite diode pump end, the crystal is dimensioned 2 mm x 3 mm in the picture)

The Nd:YLF is dimensioned 2 mm x 3 mm in the picture. Looking down from the opposite end of the pump surface, the image is actually an integrated fluorescence profile along the crystal length considering a astigmatism pump beam in the crystal. Together with the edge cooling condition, such a pump profile results in an elliptical top-hat temperature distribution along the crystal.

3.6 Resonator design

With the diode-laser end-pumped geometry and the Nd:YLF laser crystal described above, a number of laser configurations of standing-wave cavities and ring resonator have been explored to evaluate the laser efficiency, second harmonic conversion efficiency, and the spatial and spectral qualities of laser output. Using the data of the diode pump characteristics in the Nd:YLF crystal, the integrity of the gain material at high pump powers, and the thermal effect in the gain medium, a folded linear resonator (as shown in Fig. 3.6.1) has been developed for the intracavity frequency doubling. This resonator is also an optimum design for generating the fundamental mode of 1047 nm Nd:YLF laser output under the present pump geometry.

A. Resonator Description

The illustrated resonator cavity (see Fig. 3.6.1) is formed of the highly reflective coating surface D of Nd:YLF, mirror M1 and M2 with two intracavity elements: Brewster plate and KTP crystal. It is folded at an angle of incidence of around 20° by mirror M1. The total cavity length is 40 cm with a distance of 35 cm between the Nd:YLF crystal and M1; and a variable separation of about 5 cm between M1 and M2. The intracavity second harmonic generation is achieved by using a 5.5 mm KTP crystal which is cut for type-II phase-matching geometry and located at the waist of the cavity mode (near the end mirror M2). As shown in Fig 3.6.1, the diode bar is mounted vertically to incorporate with the elliptical resonator mode in the gain material. The Nd:YLF crystal is oriented with the c-axis parallel to both the pump polarisation and the

laser polarisation (perpendicular to the paper plane in the figure). Inside the cavity, the free transmission polarisation direction of Brewster plate is parallel to this linear laser polarisation while the axes of KTP crystal are oriented 45° with it. All optical parameters of related components are listed in Table 3.2.

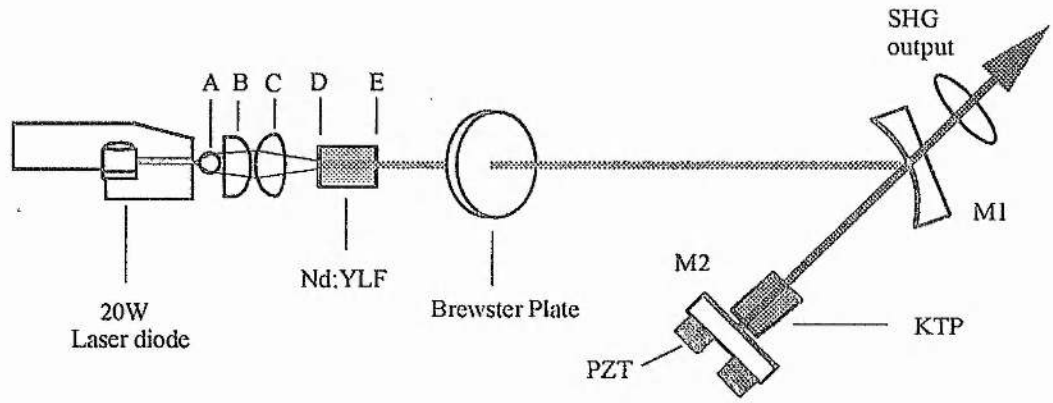

Fig. 3.6.1. Schematic configuration of intracavity frequency-doubled diode-pumped Nd:YLF laser in horizontal plane. (looking from top)

Table 3.2. Nd:YLF laser optics parameters

Optical components	*Specification*	*Reflectivity* 800 nm	1047 nm	523.5 nm	*Description*
A	f = 1.2 mm	---	---	---	rod lens
B	f = 12.7 mm	AR	---	---	cylindrical lens
C	f = 8.5 mm	AR	---	---	aspherical lens
Nd:YLF crystal D	flat	AR	HR	---	pump end surface
E	flat	---	AR	---	inside end surface
Brewster plate	—	---	uncoated	uncoated	Brewster window
M1	R.O.C. = 100 mm	---	HR	HT	curved mirror SHG output coupler
KTP crystal (both surface)	flat	---	AR	AR	nonlinear crystal
M2	flat	---	HR	HR	end surface

f: focal length; R.O.C.: Radius of Curvature; HR: High reflective; AR: Anti reflection; HT: High-transmission

As mirror M2 is HR coated for both fundamental and SHG wavelengths, the intracavity SHG beam generated in two directions can be combined into a single output by dichroic mirror M1 and M2. A positive lens of 15 cm focal length is placed in front of the SHG output collimating the large divergent laser beam. Such an optical resonator with the intracavity elements provides following advantages. (1) The 1.5 mm x 0.5 mm pump cross section in the gain medium is approximately spatial-matched with the elliptical cavity mode. Thus high laser efficiency and fundamental transverse mode can be attained. (2) The astigmatic thermal beam distortion in Nd:YLF and the cavity folding angle induced astigmatism can be fully compensated. (3) The intracavity loss is minimised by only inserting a Brewster plate. (4) Single frequency operation in SHG is achieved by using the nonlinear KTP crystal and the Brewster plate as an novel intracavity birefringent filter. (5) High conversion efficiency is achieved by placing the KTP crystal at the beam waist in the cavity, the size of the beam waist is insensitive to the thermal distortion.

In addition, by adjusting the folding angle on M1 and the separation between M1 and M2, this resonator can fully balance different thermal beam distortions in Nd:YLF crystal which correspond to the different pump power, and produce a constant circular TEM_{oo} second harmonic output. Without the intracavity Brewster plate and the nonlinear crystal, this configuration can also serve as a standing-wave resonator to generate fundamental mode 1047 nm light. By using an output coupler instead of high reflective mirror on M2, linearly polarised 1047 nm laser output can be obtained, even at the high power diode pump. In comparison with the two mirror linear cavity or the ring cavity, such a resonator can efficiently extract the diode pump power into the TEM_{oo} fundamental laser output.

B. Design of the Resonator

The elliptical cross-sectioned pump beam and the astigmatic thermal beam distortion in the Nd:YLF gain material raise two issues in the resonator design concerning

the laser beam quality and the laser efficiency. Firstly, considering the high gain and the fundamental mode operation, an elliptical cross-sectioned fundamental laser mode in the Nd:YLF crystal is required to overlap with the pump volume. Secondly, to eliminate the astigmatism in the laser output, compensation optics need to be applied in the resonator. As solutions of the first issue, Shannon et. al. [17] have used a pair of mode-expansion anamophic prisms to expand the fundamental mode in the desired dimension; Rae et al. [18] have used 3 x cylindrical lens telescope in the cavity with the same pump geometry. As for the second issue, two convex cylindrical compensation mirrors have been used in an astigmatic thermal lensing resonator by Rines [5]. However, the above lasers encounter either the elliptical pump spot or the astigmatism thermal lensing. In our intracavity-frequency-doubled Nd:YLF laser design, both issues need to be considered. In addition, a tightly focused beam waist is desired to be produced in the cavity for the nonlinear medium to take the advantage of the high electric field density. The resonator is also desired to be able to compensate the astigmatism dynamically, since the astigmatic thermal beam distortion varies with the diode pump power on Nd:YLF crystal.

As a solution of above requirements, we have used a folded resonator in the design (see Fig. 3.6.1). The whole cavity is divided into two cavity arms by the folded curve mirror M1. The longer cavity arm YLF-M1, i.e. from Nd:YLF crystal to mirror M1, efficiently extracts the diode pump energy by providing an elliptical resonator mode in Nd:YLF. This is of benefit to the cavity astigmatism which exists in this cavity arm. However, such astigmatism can be eliminated in the other cavity arm M1-M2 and a circular symmetry beam waist is formed at the end mirror M2, which is of further benefit to the intracavity frequency doubling. The SHG output with a circular TEM_{00} mode can be achieved from dichroic mirror M2.

A computer simulation modelling of such resonator incorporating with the astigmatism thermal beam distortion is conducted by using the laser cavity design (LCAV) programme. The typical resonator mode radius change along the cavity is shown in Fig. 3.6.2.(a). From the result of the thermal lensing measurement in § 3.4, we treat the

thermal beam distortion in Nd:YLF as a simple astigmatic mirror valued of 0.5 m radius-of-curvature (R.O.C) in the plane perpendicular to c-axis and of 1.2 m R.O.C in the plane parallel to c-axis. This is corresponding to the 10 W diode pumps. The mode radius change is plotted along the cavity. Tangential and sagittal modes in the plot correspond to the mode radius in the plane of horizontal and vertical respectively. As shown in Fig. 3.6.2, an astigmatic laser mode is exhibited between Nd:YLF and M1, meanwhile the tangential and sagittal modes are symmetric between M1 and M2. The elliptical cross-sectioned mode volume of 1.0 mm x 0.6 mm which is produced inside the Nd:YLF crystal approximately overlaps the 1.5 mm x 0.5 mm cross-sectioned pump beam. The inset of Fig. 3.6.2.(a) which indicate the mode radius inside the KTP crystal are enlarged in Fig. 3.6.2.(b). A beam waist of 88 μm in diameter is produced inside KTP crystal.

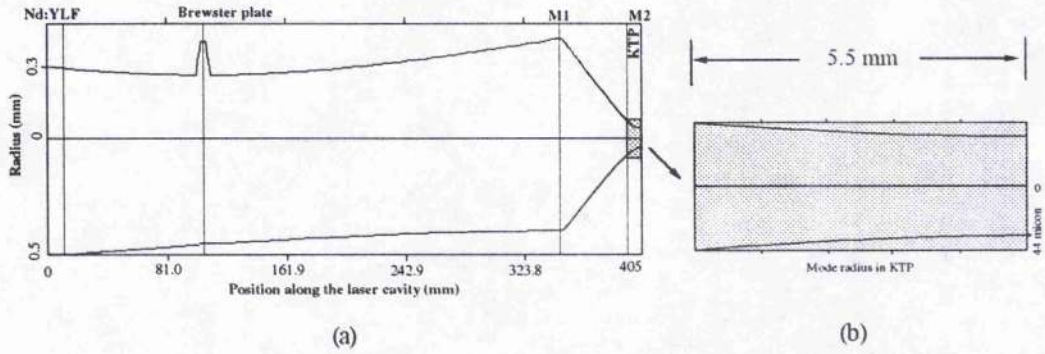

Fig. 3.6.2. Tangential and sagittal laser mode radius change in the cavity. (a) along the whole laser cavity; (b) in the KTP crystal, the enlarged inset of (a). The tangential mode is plotted above the zero line; the sagittal mode is plotted below the zero line.

C. Astigmatism in the Resonator

Naturally, a folded planar multielement resonator (e.g. shown in Fig. 3.6.1) is an astigmatic resonator; that is, the round-trip ABCD matrices may be different for rays in the tangential plane (in the plane of paper) and for rays in sagittal plane. Thus the evaluation of the ABCD matrices, eigensolutions and eigenvalues must be treated separately and independently for the two planes. However, such resonator is both geometrically stable and perturbation stable [19], but with a small range of resonator stability. Due to the large difference of the length of two arms, $L_{YLF-M1} >> L_{M1-M2}$, it is

possible to eliminate the astigmatism in the M1-M2 cavity arms by selecting a particular distance of L_{M1-M2}. Even when the astigmatic thermal beam distortion is presented in the Nd:YLF crystal, we still can keep a circular non-astigmatic resonator mode in the M1-M2 arm leaving all the astigmatism in the other cavity arm. For folded resonators, the induced astigmatism is a function of the folding angle on mirror M1. The angle induced variation of the radius of curvatures is given by:

$$R_{Ti} = R \cdot \cos\varphi_i \tag{3.2}$$

$$R_{Si} = R \cdot \sec\varphi_i \tag{3.3}$$

where R_{Ti} and R_{Si} are the effective radius of curvature of M1 in the tangential and sagittal plane, respectively, R is the radius of curvature of M1, and φ_i is the folding angle on M1. To analyse the effect of angled mirror M1 in YLF-M1 arm, we need to calculate the round trip matrix: $M1 \cdot L_{M1-M2} \cdot M2 \cdot L_{M1-M2} \cdot M1$ which is:

$$\begin{vmatrix} 1-\frac{4B}{R_i} & 2B \\ \frac{-2}{R_i}(2-\frac{4B}{R_i}) & 1-\frac{4B}{R_i} \end{vmatrix} \tag{3.4}$$

where $B = L_{M1-M2}$, R_i is the generalised curvature. Assuming the M1-M2 arm as one optics, we can estimate the effective radius of curvature of this particular optics from the function

$$\frac{-2}{r_i} = \frac{-2}{R_i}(2-\frac{4B}{R_i}) \tag{3.5}$$

In the tangential or the sagittal plane, r_i becomes r_{Ti} and r_{Si} where

$$r_{Ti} = \frac{R^2\cos^2\varphi_i}{2[R\cos\varphi_i - 2B]} \tag{3.6}$$

$$r_{Si} = \frac{R^2}{2\cos\varphi_i[R - 2B\cos\varphi_i]} \tag{3.7}$$

Fig. 3.6.3 plots the two effective curvatures against L_{M1-M2} (which is B) when $\varphi_i = 20^o$. The effective tangential curvature becomes very short in the cavity stability range of L_{M1-M2} while the sagittal curvature relaxes to a few meters in this range. This significant difference of the effective radius of curvatures in the two orthogonal planes can explain the different positions of the beam waist in the YLF-M1 cavity arm of Fig. 3.6.2. It can also explain that there is a L_{M1-M2} in the stability range to allow a circular mode resonating in M1-M2 arm.

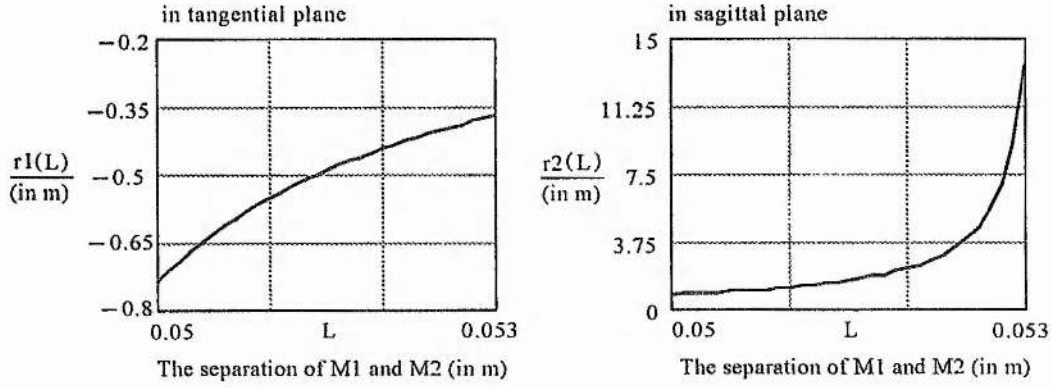

Fig. 3.6.3. The effictive radius of curvature of M1-M2 cavity arm versus the separation of M1 and M2 in tangential and sagittal planes.

D. Dynamic Resonator

Taking the astigmatic thermal beam distortion into account, we separately calculate the tangential and sagittal mode stability for the cavity described in Fig. 3.6.1. The thermal lensing in Nd:YLF is simply simulated as a $f = 5\ m$ lens which is corresponding to low power diode pump. Fig. 3.6.4 shows the cavity stability range at different folding angles. The horizontal axis of the figure is the varying separation of mirror M1 and M2: L_{M1-M2}. The vertical axis is the mode waist radius in the YLF-M1 cavity arm. Tangential and sagittal mode radius are plotted separately against L_{M1-M2}

from 40 mm to 60 mm. From the figure we can see that: (a) the larger the folding angle the smaller the stability range of the cavity becomes; (b) the stability ranges of tangential and sagittal modes move to the opposite directions with the increasing of the folding angle; (c) in the cavity stability range, the mode waist radius in the sagittal plane is much greater than that in the tangential plane.

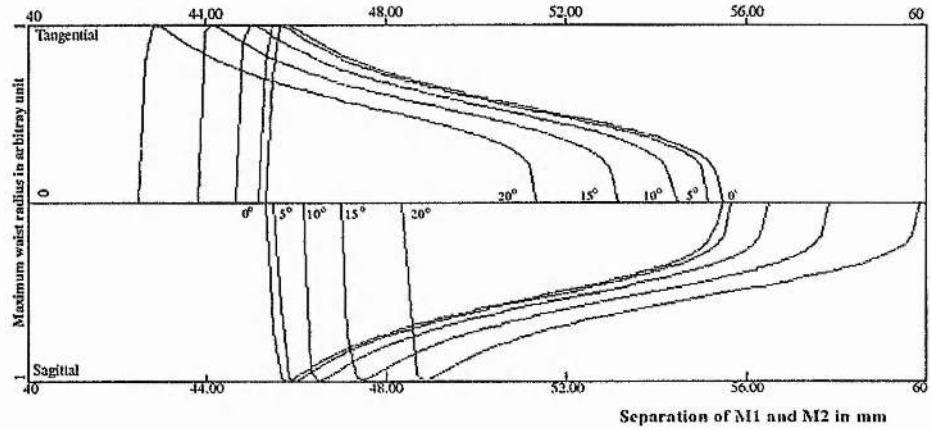

Fig. 3.6.4. Cavity stability range by varying the separation of M1 and M2. The tangential mode radius is above the zero line; the sagittal mode radius is below the zero line.

In the Nd:YLF laser design, we select the folding angle of around 20° in order to match the elliptical cross-sectioned pump volume. The separation of YLF and M1 is set to be 35 cm as an optimum length considering astigmatism in YLF-M1 arm and mode radius in Nd:YLF and KTP crystals. Based on this arrangement, the pump power dependent thermal beam distortion can be balanced simply by adjusting the separation of the mirror M1 with the mirror M2. Thus, a tightly focused circular mode can be produced in the cavity arm M1-M2 for frequency-doubling, at the same time, an elliptical cross-sectioned mode is formed in the gain medium for efficiently extracting the pump power.

However, the mode size in KTP and YLF is a function of the diode pump power due to the thermal beam distortion change in the Nd:YLF crystal. Based on the measurement of thermal lensing data in § 3.4, we are able to calculate the mode radius change with the pump power. To ensure a circular mode in KTP, the length of L_{M1-M2} is adjusted in every calculation. Fig. 3.6.5 plots the mode radius versus the pump power.

The elliptical mode radius in Nd:YLF are shown in forms of tangential mode radius and sagittal mode radius.

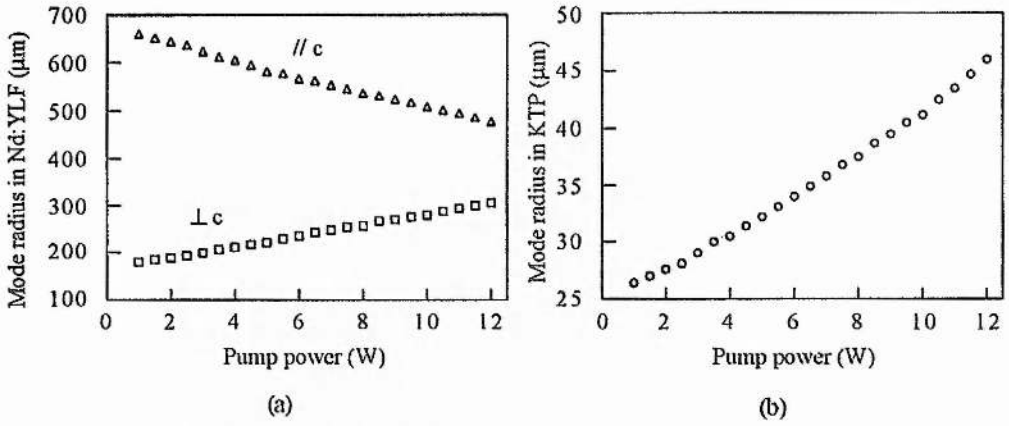

Fig. 3.6.5. Mode radius in the gain and the nonlinear medium versus diode pump power. (a) Tangential (perpendicular to c-axis) and sagittal (parallel to c-axis) mode radius in the Nd:YLF crystal. (b) Cavity mode waist inside the KTP crystal.

From above discussions of the resonator design, we can conclude that: (1) the folded resonator can fully balance the astigmatic thermal beam distortion in Nd:YLF and the cavity becomes insensitive to the thermal effects; (2) the resonator can achieve a good overlap between the cavity mode and the diode pump volume; (3) this resonator can produce a circular TEM_{00} beam waist for the efficient intracavity-frequency-doubling. In addition, combining with the intracavity birefringent filter technique, this simple cavity design exploits the use of end-pumped Nd:YLF laser in the generation of a few watts of high degree spatial and spectral quality output at the fundamental as well as the second harmonic frequency.

3.7 Laser Performance of End-Pumped Configurations

A. Plane-Parallel Resonator

In order to investigate the power characteristics and the spectral output properties, the diode-end-pumped Nd:YLF laser is initially set up as a plane-parallel resonator which simply consists of Nd:YLF crystal and a plane output mirror. Fig. 3.7.1. schematically

illustrates the end-pumped plane-parallel resonator configuration. As described previously, the laser crystal is dichroically coated at the pump end surface to form a highly transmitting window for the pump wavelength and a highly reflective mirror at the lasing wavelength. The opposite end of the laser crystal is also antireflection coated for 1047 nm light to reduce the intracavity losses. In this intensely pumped laser, the Nd:YLF crystal is mounted in a water-cooled brass heatsink in order to achieve efficient four side edge cooling. Without active water cooling, as high as 70 °C crystal surrounding surface temperature has been observed under 10 W pump. Output mirrors with 2, 5, 7, 10 and 20% laser wavelength transmission have been used in the experiments. The separation of the Nd:YLF crystal and the output mirror has been varied from 5 cm to 150 cm for the investigation of thermal lensing properties in the Nd:YLF material. However, in most experimental measurements, the plane-parallel resonator length is set to be ~ 10 cm.

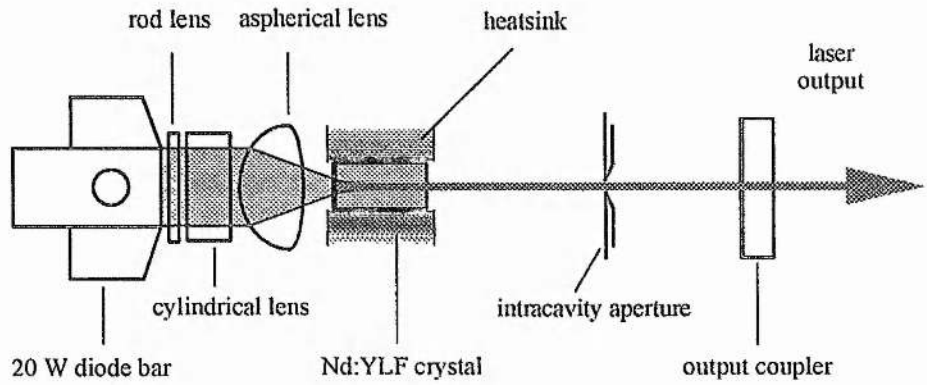

Fig. 3.7.1. Schematic plane-parallel cavity configuration of diode-pumped Nd:YLF laser. (looking from top)

It is observed in the plane-parallel Nd:YLF resonator that both 1047 nm and 1053 nm wavelengths can resonate. The optimal aligned resonator corresponds to the 1047 nm oscillation, while at certain tilted output mirror angle, the 1053 nm line could suppress the high gain 1047 nm line. Between the two extremes, both 1047 nm and 1053 nm oscillations have been observed. In the same pump condition, the output power of 1053

nm are slightly lower than that of 1047 nm. The above behaviour is believed to be the consequence of the different beam distortion effects in the Nd:YLF material for π-polarised (1047 nm) and σ-polarised (1053 nm) light. According to the experimental measurements in § 3.4, the longer thermal lensing focal length for the σ-polarisation than that for the π-polarisation enables the plane-parallel resonator to exhibit larger resonator stability. Tilting the end mirror slightly can increase the diffraction loss for the π-polarisation to the point at which the gain on the 1047 nm transition is no longer sufficient to reach the threshold. Thus, by utilising the thermal lensing behaviour for the σ- and the π-polarisation in a plane-parallel resonator, different polarised lasing wavelength can be easily selected without any additional intracavity elements.

When the diode pump power increases, the thermal lensing in the Nd:YLF crystal occurs and subsequently becomes stronger. Thus, the plane-parallel resonator becomes plano-concave resonator with a variable radius of curvature in a equivalent curved mirror. In our experiments, laser activity is observed up to a resonator length of 100 cm at 10 W diode pump. Further increasing the pump power or the cavity length can abruptly eliminate the laser action. This implies that the further increased thermal effect, which is equivalent to a ~ 100 cm R.O.C end mirror, or the further increased cavity length, which is greater than 100 cm, can drag the plano-concave resonator out of the laser stability range. The stable laser cavity length of 100 cm at 10 W pump is the lowest limit for the radius of curvature of an equivalent mirror and corresponds to a thermal lensing with a focal length of 50 cm, which is in good agreement with the measured value in § 3.4. From these values, we can see that using an equivalent astigmatistic lens or curved mirror to simulate the thermal distortion can achieve a reasonably good match, although the exact treatment of thermal distortion requires a more sophisticated modelling. The laser operation characteristics with several different cavity lengths have also been examined. As the resonator length enlarges, the laser threshold exhibits a slight increase while the slope efficiency exhibits a slight decrease. This is largely due to the increasing diffraction losses with the longer cavity length.

The end-pumped Nd:YLF plane-parallel resonator shows multi-transverse mode in its output which is subject to the elliptical pump volume and also dependent on the level of pump power. Typically, as the diode pump increase from the threshold pump power to 10 W, the transverse-mode of laser output changes from the fundamental TEM_{00} to the TEM_{20} accordingly. In the case of multimode operation, the highest slope efficiency of 47% is achieved with the 5% coupled resonator at 1047 nm, and as high as 5.4 W multimode output power have been obtained with 12.5 W diode pump. In order to achieve a fundamental transverse mode from the plane-parallel cavity, a mode selection intracavity aperture has been applied (as shown in Fig. 3.7.1). However, there are significant power losses due to the under utilisation of the gain volume. By using the aperture, ~ 2 W TEM_{00} 1047 nm laser output have been obtained. The beam profile of the TEM_{00} output is measured by a 50 μm scanning pinhole when the laser is operating at 2 W output power. The beam divergence angle is 0.90 mrad (± 2%), and the radius of the beam waist is 400 μm (± 6%). From these values, the calculated M^2 parameter is 1.08 (± 8%) which shows the output beam is nearly diffraction limited.

B. Ring Resonator

By using the end-pumped geometry, we have also constructed a simple bow-tie ring oscillator for the study of the single frequency operation. As shown in Fig. 3.7.2, the ring cavity consists of a end-pumped Nd:YLF crystal, two curved mirrors and a plane output coupler. The diode pump beam has been set primarily to pump one branch of the laser mode in the crystal. However, since the limit of the resonate mode angle in the Nd:YLF crystal is 30° because of the crystal aperture, some part of the other mode branch and the overlap region of the two mode branches are inevitably pumped. The use of the two curved mirrors are essentially for the intracavity frequency doubling. Since a tightly focused mode waist can be produced in the section between the two curved mirrors, an efficient intracavity frequency doubling could be attained. The unidirectional operation of the ring oscillator is achieved by inserting the "optical diode" which consists of a half-wave plate and a Faraday rotator. Such a unidirectional device can provide a

differential loss between clockwise and counter clockwise propagation. It is measured that the polarisation rotation angle of Faraday rotator is 5.4 degree. Thus, when the half-wave plate is oriented with one of its axes at an angle of 2.7 degree with the polarisation direction of the beam, the travelling wave in the counter clockwise direction is unattenuated in respect of polarisation losses. In addition, to further reduce the intracavity losses, both half-wave plate and Faraday crystal are AR coated at the laser wavelength.

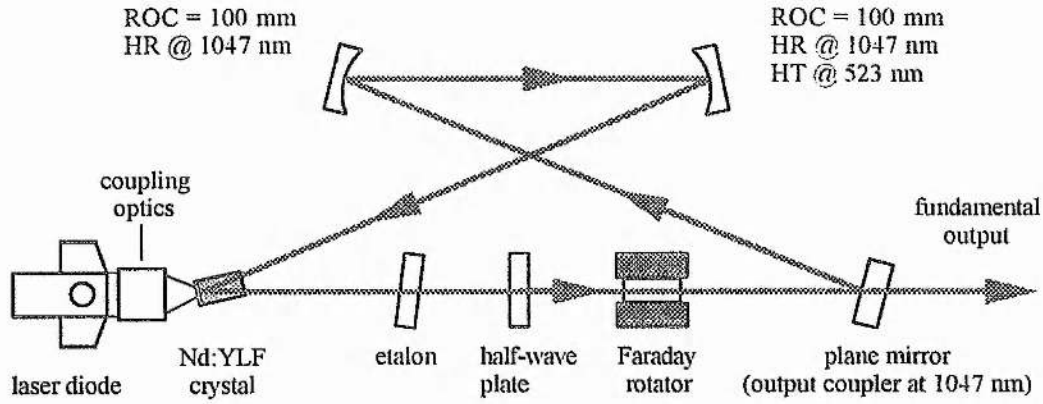

Fig. 3.7.2. Schematic ring cavity configuration of diode-pumped Nd:YLF laser. (looking from top)

In the ring resonator experiments, only linear polarised 1047 nm wavelength has been observed in the laser output. This is believed to be caused by the large polarisation losses of 1053 nm introduced by the unidirectional device. Lower optical-to-optical conversion efficiency has been attained in the ring oscillator which is partly due to the poor spatial mode overlap between the pump and the laser in the Nd:YLF and partly due to the large intracavity parasitic losses. Similarly, in order to achieve the fundamental transverse mode operation, an intracavity aperture is required. At 10 W pump, 1.8 W TEM_{00} laser output have been obtained. Although the resonator is running the unidirectional operation, the standing-wave in the gain medium is not fully demolished. Because of the limitation of the small cavity angle in Nd:YLF, a significant amount of the resonant mode are overlapped and subsequently pumped resulting in a standing-wave

gain region. Thus, an intracavity etalon is needed to ensure the high power single frequency operation. By using a 2 mm spaced fused silica etalon, we have obtained 1.6 W stable SLM laser output.

C. Folded Linear Resonator (Dog-Leg Cavity)

The folded linear cavity has been described and analysed in details in § 3.6. Such a resonator takes the advantage of the cavity astigmatism to optimise the spatial overlap of the pump and the laser, and to produce a circular tightly focused mode waist inside the laser cavity for the frequency doubling. As discussed, this cavity also possesses the geometrical and perturbation stability, as well as the flexibility to dynamically compensate the thermal beam distortion in Nd:YLF.

While experimenting with this cavity in the fundamental wavelength, we have taken the KTP crystal out of the cavity and changed the mirror M2 to a 5% plane output mirror (refer to Fig. 3.6.1). When the Brewster plate is inserted in the cavity, the output behaviour is almost unchanged compared with the empty cavity operation. This behaviour indicates that the Brewster plate introduces no loss for the linearly polarised oscillation, and only the 1047 nm wavelength is resonating in the empty cavity. By varying the separation of M1 and M2, we are able to obtain a TEM_{00} laser output without any intracavity aperture. The output beam profile is further characterised to have a M^2 parameter, which is a measurement of laser beam quality (see reference [20] [21] for the definition), of 1.12 (± 8%). Although the laser has a large beam divergence (half angle ~ 14 mrad) in its output, a f = 15 cm convex spherical lens has been used to collimate this output into a parallel diffraction limited beam. With 10 W pump, we have obtained 2.5 W of TEM_{00} output at 1047 nm from the folded cavity. In the fundamental wavelength operation, typically several axial modes are resonating in the cavity. By using an intracavity etalon (with 100 GHz FSR), SLM operation has been achieved. However, such SLM operation is not reliable due to the fact that both the adjacent cavity modes and the spatial hole burning modes are likely to be present. The novel birefringent filter has also been applied to achieve the fundamental SLM operation. In this experiment, both the

Brewster plate and the KTP crystal are placed in the M2-M1 arm of the Nd:YLF laser cavity, so that the nonlinear conversion is reduced to a minimum, and that these two elements only act as an intracavity birefringent filter. As much as 1 W of SLM laser output at 1047 nm has been obtained by using this technique.

D. Comparison

Due to the elliptical pump volume and the poor spatial overlap, lower optical-to-optical efficiency is attained for the TEM_{00} operation. In the three cavities investigated, which use the same end-pumped geometry, the dog-leg cavity is the most efficient fundamental-transverse-mode oscillator. This is because a relatively good overlap is achieved between the elliptical pump and the elliptical resonator mode in the Nd:YLF crystal. The single frequency operation is not normally associated with the standing-wave cavities due to the spatial hole burning effect in the gain medium. However, by using intracavity etalon or birefringent filter in the plane-parallel resonator or dog-leg cavity, multiple axial modes operation can be suppressed. At the same time, there are inevitable significant power losses with the SLM operation. In the travelling-wave cavity, single-frequency can be easily obtained. Due to the limitation of the small cavity fold angle in the designed ring resonator, a small standing-wave region still exists in the gain medium and is subsequently pumped. Thus, an intracavity etalon is also required. Fig. 3.7.3 shows the experimentally measured power characteristics of the TEM_{00} and SLM operations in the three cavities. Some of the parameters are further compared in Table 3.3. These figures suggest that the dog-leg cavity can be used to generate TEM_{00} fundamental output, and the ring resonator can be used to generate stable SLM fundamental output.

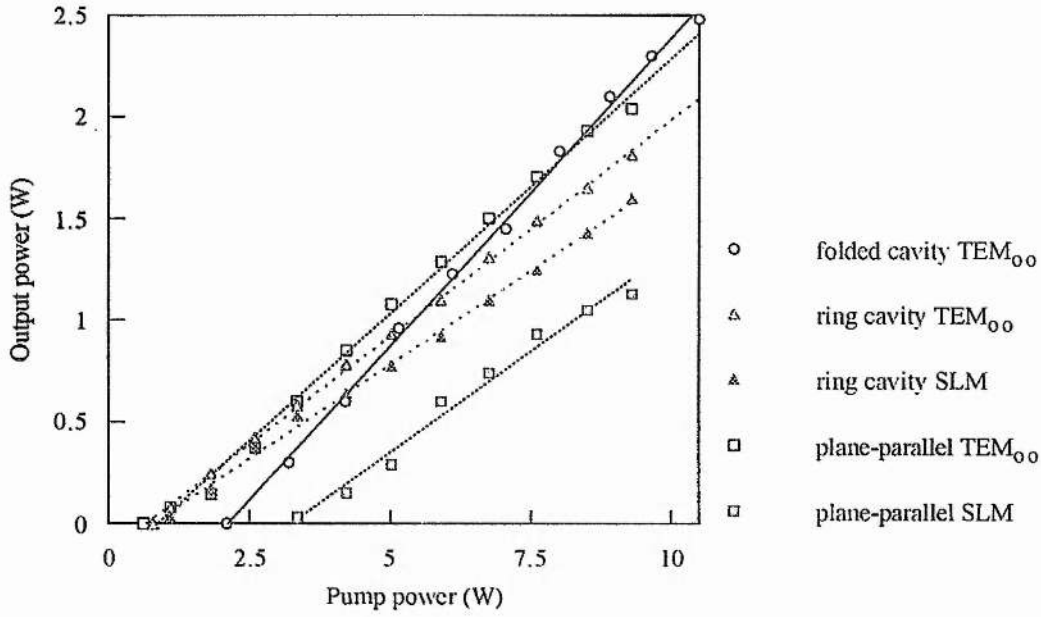

Fig. 3.7.3. Comparison of the TEMoo output power characteristics of three end-pumped resonators. They are plane-parallel cavity, ring cavity and folded linear cavity.

Table 3.3 **Comparison of three resonator configurations**

Resonator configuration	*Lasing wavelength (nm)*	*Threshold pump power (W)*	*TEM_{00} Slope efficiency (%)*	*Max. TEM_{00} output power (W)*	*Max. SLM output power (W)*
plane-parallel	1053 / 1047	0.62	25.1	2.04	1.13
ring	1047	0.79	21.3	1.81	1.6
folded cavity	1047	2.1	30.4	2.48	1

(a) All output power are measured with 5% output coupling. (b) Max. indicates the result under 10 W pump.

When considering the intracavity frequency doubling, both the ring resonator and the folded liner cavity can provide a tightly focused resonator mode for efficient nonlinear frequency conversion. To achieve the desired mode waist in the plane-parallel cavity, the alternative intracavity telescope can be used, but additional losses are also expected. The single-frequency operation of the ring resonator is an advantage in avoiding the "green problem" with intracavity frequency doubling. However, the standing-wave cavity can also be utilised in achieving stable second harmonic generation. To compare these cavity

designs in achieving a stable intracavity frequency doubling, other issues such as the intracavity parasitic loss, the effects of thermal distortion and the output directions of SHG also need to be considered. Among these cavities, the folded linear cavity design has the advantages of efficient TEM_{00} operation, high intracavity optical field, low intracavity loss, and insensitivity to the perturbation of thermal distortion in Nd:YLF. In addition, by using the novel intracavity birefringent filter, such a cavity could be utilised in the generation of stable single-frequency SHG output.

3.8 Laser Output Power Characteristics

As discussed in § 2.9, the externally measurable quantities such as laser output, threshold and slope efficiency are interrelated with the internal system efficiencies and material parameters. In diode-end-pumped solid-state laser systems, the energy is efficiently transferred from the diode pump to the laser upper state level, and subsequently becomes the useful laser output power. The total efficiency of the process is the product of the efficiencies of every energy transferring step. However, in the conversion process of a steady-state oscillation with unsaturated gain, the circulating power in the optical resonator is diminished by both the internal losses and the radiation coupled out of the resonator. Thus, the output power can reach a maximum for a specific value of output coupling factor. When output coupling is below or over the optimum value, the resonator is either under- or over-coupled with a reduction of output power. Further analyses [19] show that for different values of internal cavity loss, there is different optimum output coupling values which maximise the output power, and the optimum output coupling is always considerably smaller than the available gain. In addition, even very small internal losses have a very serious effect on the maximum useful output power available from the laser. So, in order to maximise the laser extraction efficiency, the intracavity parasitic losses need to be reduced to the minimum value. On the other hand, for a given internal loss, the output coupling factor needs to be optimised.

Similar output power characteristics are exhibited in the three experimental resonators. The multi-transverse-mode output power versus diode pump power from the plane-parallel cavity is plotted at different output coupling in Fig. 3.8.1. The laser thresholds and the output power have further been plotted as a function of the total percentage of output coupling (output mirror transmission) in Fig. 3.8.2. From these figures, it can be seen that optimum coupling of 5% are exhibited by the plane-parallel cavity, and the pump power for laser threshold linearly increases with the resonator output coupling factor. In addition, the slope efficiency of the laser exhibits slight decrease when the output coupling exceeds the optimum value.

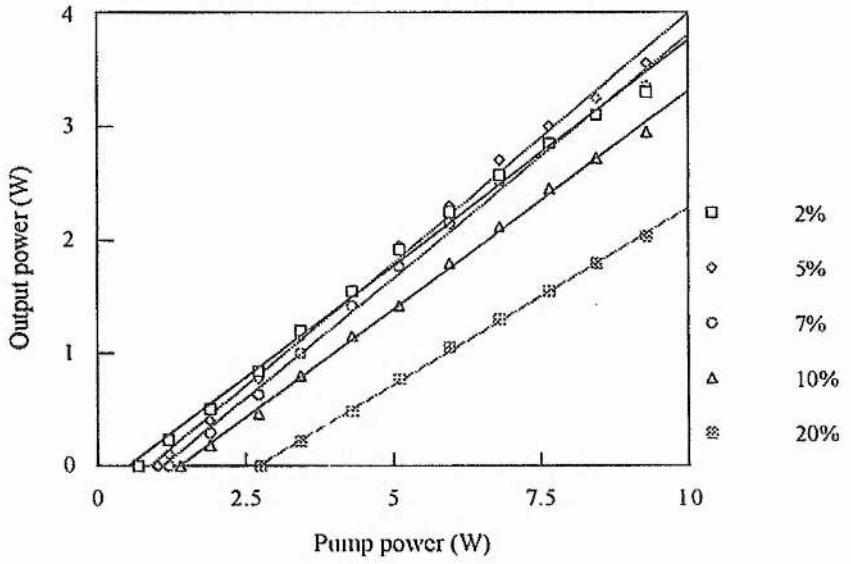

Fig. 3.8.1. Output power versus pump power for different resonator output coupling.

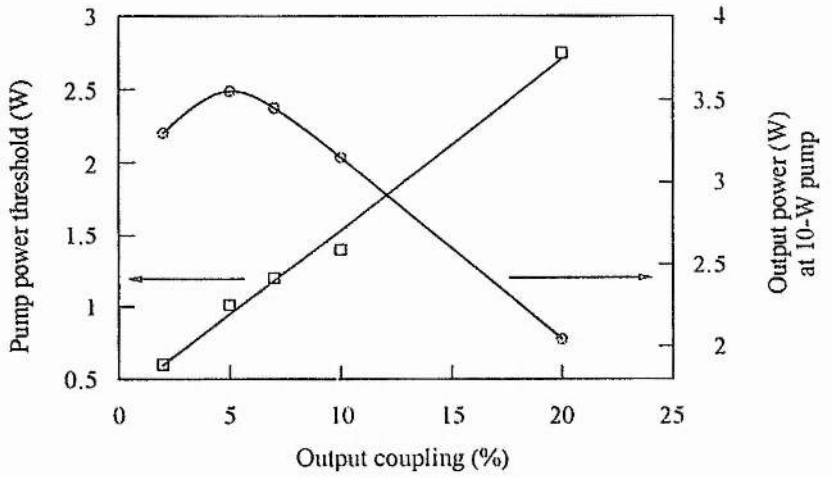

Fig. 3.8.2 Pump threshold and output power versus output coupling.

To analyse the above behaviour, we can rewrite Eq. (2.16) and Eq. (2.25) as follows:

$$P_{th} = \frac{\pi \cdot h\nu_p}{4\sigma_e \tau_2} \cdot \frac{T+L}{\eta_p}\left(w_l^2 + w_p^2\right) \tag{3.8}$$

$$\eta_s = \eta_p \frac{h\nu}{h\nu_p} \cdot \frac{T}{T+L}. \tag{3.9}$$

Here, we have written the round-trip cavity loss in terms of $T+L$, where T is the resonator output coupling (output mirror transmission) and L is the total internal parasitic loss. Due to the poor spatial mode overlap in the end-pumped geometry, the pump absorption efficiency η_p inside the laser mode is uncertain. Hence, the value of pump threshold and slope efficiency can only be estimated from the modelling. In the folded resonator, the typical round-trip internal loss is 2.5 %, and the pump absorption efficiency η_p inside the laser mode is essentially limited by the ratio of the pump and the laser mode spatial overlap which is 1.5 : 1 (see fig. 3.5.4). Thus, the calculated value of slope efficiency in this case is 33.8 % which is in close agreement with the actual value of 30.4 % (see Table 3.3). In the plane-parallel resonator, the pump absorption factor η_p for

multi-transverse mode operation is much higher than that in the folded resonator. If we estimate $\eta_p = 90\%$, the calculated slope efficiency becomes 49 % which is also in good agreement with the maximum experimentally obtained value of 47 %. The fact that the slope efficiency decreases with the output coupling is inconsistent with Eq. (3.10). However, it can be understood because of the absence of high order traverse mode in the oscillation. When the resonator output coupling increases, the threshold for the high-order transverse mode oscillation also increases due to the limited laser gain. At certain pump powers, such a behaviour is equivalent to a smaller η_p, giving a lower value of slope efficiency. The linear relationship between the pump threshold and the output coupling which is exhibited in the experiment is also given by Eq. (3.9).

To analyse the optimum resonator output coupling, Eq. (2.24) can also be written in the form [22]

$$P_{out} = I_s A \cdot T \cdot (\frac{g_o}{L+T} - 1) \tag{3.10}$$

where g_o is the unsaturated round-trip laser gain, A is the cross-sectional area of the mode, and I_s is the saturation intensity. Maximising P_{out} with respect to T by setting $\partial P_{out}/\partial T = 0$ yields

$$T_{opt} = -L + \sqrt{g_o \cdot L} \tag{3.11}$$

as the condition for the mirror transmission that yields the maximum power output. In the plane parallel resonator, we have $g_o \approx 25\%$ and $L \approx 2\%$. Hence, the theoretical predicted value of the optimum resonator coupling is also ~ 5 %.

3.9 Spectral Output of Standing-Wave Cavity

In the experiment, the laser axial mode structure is analysed by a Fabry-Perot interferometer with variable free spectral range (FSR) and by a spectrum analyser. The

Fabry-Perot interferometer consists of two plane mirrors both HR coated at the laser wavelength. The separation of the two mirrors can vary from 0.5 mm to 25 mm, giving a variable interferometer FSR of 300 GHz to 6 GHz. A small area (1 mm^2) photodiode placed on the output side of the interferometer is used to monitor the intensity of the central Fabry-Perot fringe when the interferometer is scanned through several free spectral ranges. The *Hewlett-Packard 70004A spectrum analyser* is used with a fast silicon photodiode to detect the intensity of the laser output and then proceed to the Fourier transformation. The signal from the photodiode which contains the different frequency between the oscillating axial modes can be analysed in spectrum. Because of the limitation of the photodiode, only those beat notes lower than 3 GHz can be observed. In addition, such a device can also be used to analyse the phase noise of the laser output.

The standing-wave cavities used in the experiments have exhibited similar behaviour in their spectral output. Fig. 3.9.1 shows a typical trace of a laser output spectrum. It is obtained from a 300 GHz FSR Fabry-Perot interferometer when the interferometer cavity length is scanned over a range of 1 μm. In the figure, the standing-wave cavity laser oscillates in 5 or 6 stable axial modes separated by a regular spacing of 25 GHz. Such axial mode structure is independent of cavity length and cavity configurations, as long as the standing-wave mode pattern is present inside the Nd:YLF crystal. The fixed mode spacing is measured by varying the separation of the interferometer mirrors. When these oscillating modes are completely overlapped, the free spectral range of the Fabry-Perot interferometer are equal in value to the frequency spacing of the modes, which is a constant 25 GHz. The detailed adjacent cavity modes can not be resolved by the Fabry-Perot interferometer. However, they can be recorded by the spectrum analyser. The beat note of adjacent cavity modes, whose value, subject to the cavity length, is $c/2L_{cav}$ (typically ~ 1.5 GHz in plane-parallel resonator and ~ 400 MHz in the dog-leg cavity), only appears occasionally on the spectrum analyser. It is also noticed that the stabilised cavity can greatly reduce the appearance of such beat note.

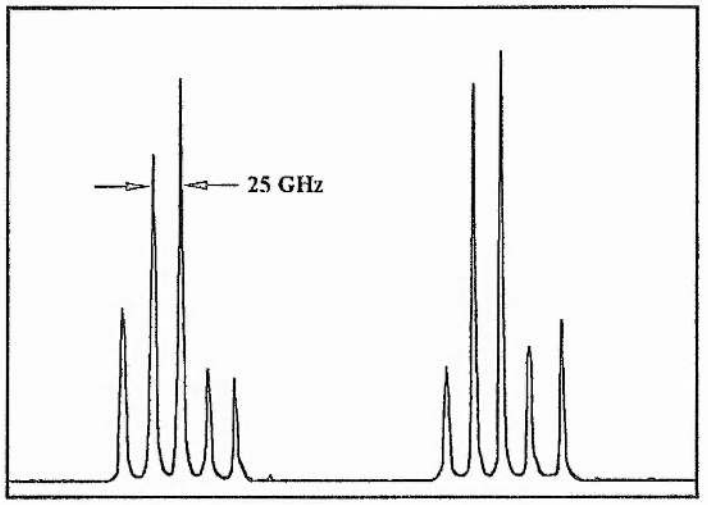

Fig. 3.9.1. Spatial hole burning modes of Nd:YLF laser. Trace from a 300 GHz F.S.R. scanning Fabry-Perot interferometer.

The appearance of the adjacent cavity mode beat is largely dependent on the instability of the cavity length. It is believed that the beat note is observed only when the adjacent cavity mode hop occurs which is induced by the perturbation of the cavity length. Also, the gain competition between the adjacent cavity modes increases the chance of such mode hops. The regular frequency spacing of 25 GHz in the axial mode structure can be analysed by Eq. (2.19). Because the gain medium is located at the end of the cavity, the antinodes of all cavity mode are pinned at HR surface of the laser crystal. Thus the potential standing-wave mode that can utilise the gain region unoccupied by the primary mode pattern is the second resonator mode. The phase relationship between the two modes can be simply written as $c/2nl_{rod}$. In our end-pumped Nd:YLF laser, we have $l_{rod} = 4\ mm$, $n = 1.5$. From these values, 25 GHz mode frequency spacing is given. Since the secondary resonating mode interacts essentially with a different spatial group of laser active centres from the primary mode, there is little or no gain competition between these two modes and both can oscillate simultaneously. Through this process, it may be understood that several axial modes can simultaneously oscillate in the cavity with a regular frequency spacing.

3.10 Summary

An efficient folded optical resonator has been designed and constructed. Such a cavity design is derived from the considerations of efficiently extracting the elliptical diode pump into a TEM_{00} resonator mode for the intracavity frequency doubling. From this folded optical resonator, we have obtained diffraction-limited output power of 2.5 W with 10 W diode pump. The laser performance in the resonator has been characterised and further compared with the plane-parallel resonator and ring resonator with the same end-pump geometry. The basic investigations and considerations for this laser design have been performed. They include the investigations of the laser properties and the thermal effects of Nd:YLF material with diode-end-pump, the design considerations of the end-pump geometry, and the theoretical analysis of the folded optical resonator.

References

[1] A. L. Harmer, A. Linz, and D. R. Gabbe, "Fluorescence of Nd^{3+} in Lithium Yttrium Fluoride", *J. Phys. Chem. Solids*, vol. 30, pp. 1483-1491, 1969.

[2] T. M. Pollak, W. F. Wing, R. J. Grasso, E. P. Chicklis, and H. P. Jenssen, "CW laser operation of Nd:YLF", *IEEE J. Quant. Electron.*, vol. 18, pp. 159-163, 1982.

[3] J. R. Ryan and R. Beach, "Optical absorption and stimulated emission of Neodymium in Yttrium Lithium Fluoride", *J. Opt. Soc. Am. B*, vol. 9, pp. 1883-1887, 1992.

[4] G. Cerullo, S. De Silvestri, and V. Magni, "High efficiency, 40W CW Nd:YLF laser with large TEM_{00} mode", *Optics Comm.*, vol. 93, pp. 77-81, 1992.

[5] R. A. Rines, R. A. Schwarz, and P. F. Moulton, "Diode-laser-pumped, CW, Nd:YLF laser with efficient intracavity second harmonic generation", *Conf. on Advanced Solid-state lasers*, Salt-lake City, paper ATuD3, 1994.

[6] W. Koechner, "Solid-state Laser Engineering", Third Edition, *Springer-Verlag*, pp. 338-401, 1993.

[7] C. Pfistner, R. Wever, H. P. Weber, S. Merazzi, and R. Gruber, "Thermal beam distortions in end-pumped Nd:YAG, Nd:GSGG, and Nd:YLF rods",*IEEE J. of Quant. Electron.*, vol. 30, pp. 1605-1615, 1994.

[8] A. K. Cousins, "Temperature and thermal stress scaling in finite-length end-pumped laser rods", *IEEE J. Quant. Electron.*, vol. 28, pp. 1057-1069, 1992.

[9] T. M. Baer, M. S. Keirsted, "Modeling of end-pumped solid-state lasers". *Tech. Dig. CLEO '93*, paper CFM1.

[10] J. Berger, D. F. Welch, W. Streifer, and D. R. Scifres N. J. Hoffman. J. J. Smith and D. Radecki, "Fibre-bundle coupled, diode end-pumped Nd:YAG laser", *Opt. Lett.*, vol. 13, pp. 306-308, 1988.

[11] W. A. Clarkson, A. B. Neilson, D. C. Hanna, "Novel beam shaping technique for high-power diode bars", *Tech. Dig. CLEO '94*, paper CThL2.

[12] J. J. Snyder, P. Reichert, and T. Baer, "Fast diffraction-limited cylindrical microlenses" *Appl. Opt.*, vol. 30, pp. 2743-2747, 1991.

[13] S. Yamaguchi and H. Imai, "Efficient Nd:YAG laser end-pumped by a 1 cm aperture laser diode bar with a GRIN lens array coupling", *IEEE J. Quant. Electron.*, vol. 28, 1992.

[14] W. Goltsos and J. R. Leger, "1-D to 2-D optical transformation of a 5-Watt diode-laser bar for end-pumping solid-state laser using binary optics", *Tech. Dig. CLEO '91*, paper CFC5.

[15] G. Feugnet, C. Bussac, C. Larat, M. Schwarz, and J. P. Pocholle, "High-efficiency TEM_{00} Nd:YVO_4 laser longitudinal pumped by a high-power array", *Opt. Lett.*, vol. 20, pp. 157-159, 1995.

[16] S. C. Tidwell, J. F. Seamans, C. E. Hamilton C. H. Muller, and D. D. Lowenthal, "Efficient, 15-W output power, diode-end-pumped Nd:YAG laser", *Opt. Lett.*, vol. 16, pp. 584-586, 1991.

[17] D. C. Shannon and R. W. Wallace, "High-power Nd:YAG laser and pumped by a CW, 10 mm x 1 μm aperture, 10-W laser-diode bar" *Opt. Lett.*, vol. 16, pp. 318-320, 1991.

[18] C. F. Rae, J. A. C. Terry, B. D. Sinclair, M. H. Dunn, and W. Sibbett, "Single-frequency, end-pumped Nd:YLF excited by a 12-mJ diode-laser array", *Opt. Lett.*, vol. 17, pp. 1673-1675, 1992.

[19] A. E. Siegman, "Lasers", Chapter 21, *University Science Books*, 1985.

[20] M. W. Sasnett and T. F. Johnston, Jr., "Beam characteristics and measurement of propagation attributes", *SPIE Proceedings* vol. 1414, 1991.

[21] A. E. Siegman, "New development in laser resonators" in *Laser Resonator*, D. A. Holmes Ed., *Proc. SPIE*, vol. 1224, pp. 2-14, 1990.

[22] A. Yariv, "Optical Electronics", *Saunder College Publishing*, 4th Edition, 1993.

Chapter 4

1-W SINGLE-FREQUENCY GREEN LASER

4.1 Introduction

Frequency-doubled diode-pumped Nd^{3+} lasers represent one of the most efficient laser sources of visible radiation. In the continuous-wave regime, efficient frequency conversion processes are obtained by using resonant enhancement techniques such as intracavity doubling or external resonant doubling where high resonant optical fields are available within the nonlinear medium. Intracavity frequency doubling (or second-harmonic generation) is achieved by placing the nonlinear crystal inside the laser cavity to make direct use of the high circulating power in the resonator. Although simple to implement, it is difficult to realise good performance with this approach since the cavity must be simultaneously optimised for the infrared power and the second harmonic output. In addition, chaotic intensity fluctuations may be present in this process due to the nonlinear sum-frequency generation (SFG) coupling of different cavity modes. The alternative technique of external resonant frequency doubling is achieved by coupling the laser output into a second cavity in which includes a doubling crystal. While this requires extra components, it allows for the generation of the infrared and the second harmonic to be individually optimised. However, it requires a highly stable, narrow linewidth, and single frequency laser as the input source.

According to the experimental results detailed in the previous chapter, SLM operation of the standing-wave Nd:YLF laser greatly reduced the laser efficiency. Also the performance was somewhat unreliable due to the effects of the spatial hole burning. In order to obtain an efficient single-frequency second harmonic output from the laser, we have utilised an intracavity doubling architecture and eliminated the so called "green problem" by using the birefringence of the KTP crystal in combination with a polariser

(Brewster plate) to form an intracavity birefringent filter. This combination was capable of suppressing the multimode operation of the standing-wave laser hence resulting in a single frequency SHG output. In addition, the frequency-doubling efficiency has been greatly improved since this design minimises the intracavity losses by minimising the intracavity components used. In this chapter, we will analyse the conditions for obtaining efficient single-frequency intracavity SHG output and discuss the performance of the 1-W SLM green laser.

4.2 Nonlinear Materials

A. Nonlinear Optical Properties of KTP

The biaxial nonlinear crystal Potassium Titanyl Phosphate ($KTiOPO_4$, KTP) has been used in the intracavity frequency doubling and also in the degenerate OPO which will be described in chapter 5. It is a unique nonlinear material that has been shown to have excellent properties for frequency doubling the 1 μm radiation of the Nd lasers. It is also very attractive for various sum- and difference-frequency mixing schemes and parametric optical applications over most of its transparency range. KTP has a combination of favourable properties [1] namely: large nonlinear optical coefficients ($d_{eff} \approx 5.1$ pm/V for 1.064 mm doubling); broad temperature bandwidth (25 °C-cm) and spectral bandwidth (5.6 Å-cm); wide angular bandwidth (20 mrad-cm) and small walk-off angle (4.5 mrad or 0.26 °). The birefringence in the x-y and the x-z principle plane allows phase matching for the more effective type-II frequency conversion process over a large wavelength range. It is highly suitable for frequency up-conversion process, offering high conversion efficiency when frequency doubling, or when generating sum and difference frequencies. In addition, its large electro-optic coefficients and low dielectric constants make it attractive for various electro-optic applications, such as modulators and Q-switches.

Single crystals of KTP can be grown by both hydrothermal and flux techniques. It crystallises in the orthorhombic point group mm2. The crystal structure, refractive indices, nonlinear coefficient, and phase-matching parameters have been reported in

references [2], [3], [4], and [5]. KTP has a transparency range from 0.35 μm to 4.5 μm, but with measurable absorption beyond $\lambda \sim 2.8$ μm. The linear absorption loss at $\lambda \sim 1.06$ μm is ~ 1% /cm and a few percent at $\lambda \sim 0.53$ μm. Refractive indices of different KTP samples may vary subject to the crystal growth technique, the growth process and the crystal temperature. However, Sellmeier equations for KTP can give a fairly accurate prediction of the phase matching angle. Other phase-matching parameters such as phase-matching temperature bandwidth, angular bandwidth and walk-off angle can also be calculated from Sellmeier equations which fit actual measured refractive indices.

In KTP, the indices of refraction allow both type-I and type-II SHG. The conditions for phase matching in the type-I and the type-II interactions and the corresponding effective nonlinear coefficients have been examined by Ito et al. [6] and Yao et al. [5]. The expressions for the effective nonlinear coefficient, d_{eff}, in the two possible interactions are [7]

$$d_{eff}(I) = \frac{1}{2}(d_{15} - d_{24}) \cdot \sin 2\theta \cdot \sin 2\phi \tag{4.1}$$

$$\begin{aligned} d_{eff}(II) = {} & (d_{24} - d_{15}) \cdot \sin 2\theta \cdot \sin 2\phi \\ & -(d_{15} \sin^2 \phi + d_{24} \cos^2 \phi) \sin \theta \end{aligned} \tag{4.2}$$

where ϕ is the angle from the x-axis (refer Fig. 4.2.1) in the x-y plane and θ is the angle from the z-axis. Since the effective nonlinear coefficient, d_{eff}, for type-I SHG is nearly an order of magnitude smaller than that for type-II, for efficient interactions type-II SHG is preferred. The wavelength range over which type-II SHG is allowed is limited by the birefringent and dispersive properties of KTP. In the x-y principal plane, SHG phase-matching can be achieved over the internal angle range of $\phi \sim 74^o$ to 5^o for fundamental wavelength range $\lambda \sim 1.0$ μm to 1.078 μm. In the x-z principal plane, SHG phase matching can be achieved in the internal angle range of $\theta \sim 90^o$ to 55^o for fundamental wavelength range $\lambda \sim 1.08$ μm to 2.0 μm. Noncritically phase-matched frequency doubling in an a-cut KTP crystal at 1.08 μm has also been reported [8]. Fig. 4.2.1 shows the crystal

orientation for the phase-matching condition of the type-II interaction at 1.047 μm. In the figure, KTP is a 3 mm x 3 mm x 6 mm flux-grown crystal with two faces antireflection coated for low loss at both fundamental and second-harmonic wavelengths. The crystal is cut for propagation at $\theta = 90^o$, $\phi = 37^o$. Because type-II phase-matching requires both an ordinary (o) and an extraordinary (e) beam for the generation of the second-harmonic, the incident infrared light is linearly polarised at 45° with respect to the e- or o-ray polarisations of the crystal. The generated green light is polarised along the extraordinary-ray polarisation.

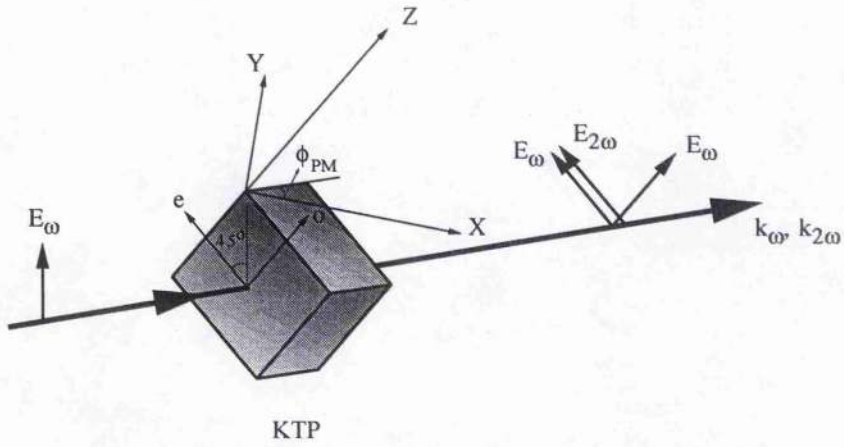

Fig. 4.2.1. Phase matching geometry in the KTP crystal for the frequency doubling of 1.047 μm. (x, y, z) is the optical frame, which is identical to the crystallographical axes (a, b, c) of KTP. k_ω and $k_{2\omega}$ are the collinear wave vectors of the fundamental and the harmonic wave respectively, E_ω and $E_{2\omega}$ are the associated electric field vectors which allow type-II phase matching. $\phi_{PM} = 37^o$ is the phase-matching angle for the conversion 1.047 μm to 0.523 μm in x-y plane. The linear polarization of incident fundamental beam is aligned 45° with the extraordinary ray polarization for the optimum frequency-doubling.

Frequency doubling efficiency in excess of 65% are now routinely obtained from KTP crystals by using high quality laser beams, and values as high as 85% for CW frequency doubling have been demonstrated [8]. Although the quality of the material has been improving, scaling up SHG efficiencies at room temperature continues to be limited by gradual photochemical degradation (grey tracking) [9] [10] which is cumulative with exposure to a combination of second-harmonic and fundamental radiation. The degradation

leads to increased absorption in the crystal which can eventually cause crystal failure. In our experiments, the observed grey track was a dark-grey line throughout the KTP crystal from surface of surface following the 1.047 μm beam. It was also observed that some KTP crystal samples were more likely to form grey tracking than others. Obvious grey tracks can be formed in these crystals in a few hours by intracavity frequency doubling the 1.047 μm radiation to generate 1 W continuous-wave green light, while other crystals have not exhibited visible grey tracks even after tens of hours of operation under the same operation conditions. This is believed to be due to the crystal quality variations in the two growth runs. It is possible to prevent the grey track formation by raising the crystal temperature above 150 °C [11]. However, the optically induced photorefractive damage which results from multiphoton absorption of fundamental and second-harmonic photons is still present in KTP. This effect produces an astigmatic distortion of the second-harmonic output and reduces the up-conversion efficiency.

Variation of the refractive indices and birefringence of KTP with temperature is another factor that reduces the efficiency of the nonlinear interaction. While the nonlinear interaction proceeds, a fraction of the radiation is absorbed. Because the heating of the nonlinear crystal by the absorbed radiation is volumetric while cooling tends to be a surface effect, thermal gradients are established. Since the refractive index is dependent on temperature, the thermal gradient also induces a spatial variation of the refractive indices. However, for efficient nonlinear interaction, the refractive indices must satisfy the phase matching condition quite closely. A spatial variation of the refractive indices prohibits ideal phase matching throughout the volume of the nonlinear crystal. Since the establishment of thermal gradients is a slow process, accordingly the second harmonic output power slowly drifts downward, which has been observed in our experiments.

B. Nonlinear Optical Properties of LBO

In addition to the type-II KTP phase-matching geometry, noncritical type-I phase matching LBO crystal has also been used in the intracavity frequency doubling and the optical parametric oscillation. However, type-I phase-matched crystals can not be utilised

as a birefringent element in the cavity. Lithium Triborate (LiB_3O_5, LBO) is a recently developed nonlinear optical material that is characterised by high damage threshold (> 15 GW/cm^2 for nanosecond pulses), a wide transparency range (160 - 2600 nm), large acceptance bandwidths, and moderate nonlinear coefficients. Due to the biaxial nature of the crystal it can provide phased-matched nonlinear interactions in all three principal planes. The critical angle tuned type-I interaction (e $\rightarrow$ o + o) in the x-y principal plane can provide wide tuning ranges, while in the x-z and y-z planes, it is possible to use type-II phase matching (e $\rightarrow$ o + e and o $\rightarrow$ e + o, respectively) in critical or noncritical configurations for smaller tuning ranges by using angular or temperature control. One of the most attractive properties of LBO in OPO devices is the possibility of temperature tuned noncritical phase matching (NCPM) operation. The type-I NCPM geometry (θ = 90°, ϕ = 0°; e $\rightarrow$ o + o; $d_{eff} \approx 1.2$ pm/V) is usually used in frequency doubling of near infrared laser sources. Between room temperature and T $\approx$ 300 °C, this geometry can provide NCPM frequency doubling for 0.9 μm < λ_{laser} < 1.7 μm. With θ = 90° and ϕ = 0°, and the parametric waves travelling along the x-axis, Poynting vector walk-off is eliminated. Also, since the effective nonlinear coefficient for the type-I interaction is given by $d_{eff} = d_{32} \cos\phi$, we maximise the parametric gain with $d_{eff} \sim 1.2\ pm/V$ over the complete temperature tuned wavelength range. This geometry also avoids the problem of Fresnel reflection loss associated with angle tuned devices such as the KTP OPO, thus allowing high efficiencies to be maintained across the available tuning range. Furthermore, the large spectral and angular acceptance bandwidths are favourable for efficient conversion of ultrashort pulses in tightly focused beams, allowing the use of longer crystal lengths before the onset of gain reduction.

The LBO crystal used in our experiments was an a-axis cut, 20 mm long, with AR-coated facets at both fundamental and second-harmonic wavelengths. This orientation can be temperature tuned in the type-I noncritical SHG (OPO) phase-matching geometry, with the fundamental wave (signal and idler wave) polarised along the z principal optical axis, and the second harmonic wave (OPO pump wave) polarised along the y-axis. The

principal optical axes x, y and z are parallel to the crystallographic axes a, c and b respectively. The optimum frequency doubling was observed for a measured temperature of 166.3 °C. When configured as a doubly resonant OPO, the degenerate parametric oscillation can be observed in the temperature range of 1.3 ° around 166.3 °C which correspond to an OPO wavelength tuning range extended from 990 nm to 1100 nm.

4.3 Efficiency of Intracavity Second Harmonic Generation

As Eq. (1.6) indicates, the efficiency of second harmonic generation depends upon a number of factors of which the most important are the fundamental power level, the length of the crystal, the degree of focusing of the fundamental beam, the magnitude of the nonlinear coefficient of the material, and the phase-matching conditions. However, when we consider the effect of placing the doubling crystal inside the laser cavity, the maximum SHG power generated is under conditions of optimum output coupling. According to the theory of Smith [12], there is an optimum output coupling of the SHG produced in the intracavity doubled continuous-wave laser similar to the optimum output coupling for a conventional laser, and the maximum second harmonic power generated can be equal to the maximum fundamental power available from the laser. Such a theory is based on the rate-equation description of the lasers oscillation in which the frequency-doubling and sum-frequency generation processes are modelled as intensity-dependent nonlinear losses, and both steady-state and transient behaviour are performed. We rewrite Eq. (1.8) and (1.9) which describe the steady state round-trip saturated gain in relation with the laser and nonlinear losses in intracavity-doubled laser as,

$$\frac{2g_o l}{1+I/I_s} = L + K' I \tag{4.3}$$

$$K'_{\max} = \frac{L}{I_s} \tag{4.4}$$

Eq. (4.3) is simply a statement that the gain equals the sum of the linear and nonlinear losses. Eq. (4.4) gives the magnitude of nonlinearity required for optimum second-harmonic generation. It is proportional to the linear loss at the fundamental wavelength, inversely proportional the saturation density for the laser transition and independent of gain. Thus, for a given loss, it is possible to achieve maximum second harmonic conversion efficiency at all values of gain and hence all power levels without the need for adjustment of the nonlinear coupling. This behaviour is in contrast to the problem of output coupling from a normal homogeneously broadened laser where the optimum transmission is given by Eq. (3.11) which is gain dependent. The reason is that the effective nonlinear loss, which can be viewed as a fictitious transmission, increases with the fundamental power density.

From Eq. (4.4), the optimum nonlinear output coupling corresponds to the optimum length l_{opt} of the nonlinear crystal, which is given by

$$l_{opt} = \left[\left(\frac{\varepsilon_o}{\mu_o}\right)^{1/2} \cdot \frac{n^3 c^2}{2\omega^2 \cdot d_{eff}^{\ 2} \cdot \kappa} \cdot \frac{L}{S_o} \right]^{1/2}, \qquad (4.5)$$

where the laser beam diameter is assumed to be constant. In our experiment, the round-trip loss was L = 0.02, the saturation intensity $S_o = 0.22 \times 10^8$ Wm^{-2}, the refractive index n = 1.47, the laser frequency $\omega = 1.8 \times 10^{15}$ Hz, the intracavity beam focusing factor $\kappa \approx 100$, and the effective nonlinear coefficient $d_{eff} = 4 \times 10^{-12}$ m/V. The values yield an optimum length $l_{opt} = 0.78$ cm, which is quite near to the length of the nonlinear crystal used in our experiments, $l = 6$ mm. According to the theory [13], it follows that if the linear loss due to the inserted second-harmonic crystal is small compared to the total internal loss, the value of nonlinear coupling factor K' is the same for fundamental and second-harmonic output coupling. Also, the maximum second-harmonic power equals the fundamental power obtainable from the same laser. However, in practical intracavity frequency doubled laser systems, the second-harmonic power is usually considerably below the output power which can be achieved at the fundamental wavelength even with

the optimum length crystal. The reason is that the insertion loss of the nonlinear crystal is in many cases significant in the low-gain lasers employed for intracavity frequency doubling. Furthermore availability of crystals and damage considerations often lead to non-optimum conditions as far as crystal length and pump-power density are concerned.

A shorter optimum crystal length is often desired in nonlinear conversion systems [13]. From Eq. (4.5) we can see that the optimum length l_{opt} at a given effective nonlinear coefficient d_{eff} is reduced by an increase in the saturation intensity S_o and a decrease in the total internal round trip linear losses L at the fundamental wavelength. The quantity L includes transmission, scattering, and absorption losses in the mirrors, and absorption and scattering losses in the laser medium and nonlinear crystal as well as any other cavity components. However, a high saturation intensity is not an advantage since the laser threshold intensity will be also high. Also the internal losses are limited by the optical properties of gain medium and nonlinear material. Alternatively, the optimum length can also be reduced significantly by reducing the size of the intracavity mode waist. Such a tightly focused beam is only limited by the optimum phase matching condition. In practical systems, although the optimum coupling can be achieved with an optimum crystal length, the extracted SHG power is often much lower than the available fundamental power. In addition, the conversion efficiency is insensitive to the length of the nonlinear crystal, if the laser is operating far above threshold. This is because a short nonlinear crystal which is shorter than the optimum length can effectively reduce the intracavity scattering and absorption losses and thus improve the extraction efficiency. In contrast to the optimum crystal length, the effects of loss in the laser are shown to reduce the available fundamental as well as second harmonic power and to increase the magnitude of the nonlinearity required for optimum coupling. Therefore the reduction of the internal resonator losses is the key to efficient intracavity frequency doubling. In our experiment, the insertion loss of the Brewster plate and the KTP crystal is estimated as 1%, which is, we believe, limited by absorption loss of KTP material.

There are three primary factors that need to be considered in the design of a laser cavity configuration for efficient intracavity frequency doubling. In order to achieve efficient harmonic generation it is important to obtain a high power density inside the nonlinear crystal. Thus, the cavity mode must be large enough inside the laser rod to utilise the maximum gain volume which can contribute to TEM_{00} mode oscillation, while a small cross-sectional area is desired inside the nonlinear crystal. Focusing optics are generally required in the cavity so as to achieve a large mode cross-section ratio between the two positions. Since the intracavity loss is the key factor for the extraction efficiency for the optimised resonator, it is desirable to reduce both the nonlinear crystal insertion losses and other cavity element losses. Finally, since intracavity second-harmonic generation produces a beam in two directions, it is necessary to select a cavity configuration which permits recovery of both beams. In addition, when joining the two SHG outputs into a single output, the destructive interference of the two overlapped beams due to the phase difference needs to be avoid. In our laser design, a cavity mode cross-section ratio of ~ 100 has been achieved between the positions of the laser rod and the nonlinear crystal. The insertion loss was minimised by only inserting a Brewster plate and a KTP crystal. And a dichroic end mirror was used to combine the bi-directional green output into a single output.

4.4 Theoretical Study of Stable Single-Frequency Operation of Intracavity-Doubled Diode-Pumped Nd:YLF Laser

A. the "Green Problem"

The analysis of efficient intracavity SHG in § 4.3 was made under the assumption of stable single-frequency operation of the fundamental laser. In practice, however, intracavity frequency doubling of a laser which operates in many longitudinal modes oscillate usually exhibits large fluctuations in the instantaneous as well as the average harmonic power. This so called "green problem" was first considered in detail by Baer [14]. The cavity he used consisted of an end-pumped Nd:YAG rod, a KTP crystal and a

curved reflector, with no additional polarisation-controlling elements. When the laser operated without an intracavity etalon, it produced chaotic amplitude fluctuations. When an etalon was added to force two-mode operation, well-defined periodic oscillations were observed. Finally, a laser forced to run in a single mode with an etalon was stable but produced very little green output. Baer explained this behaviour in a simple phenomenological manner by considering the sum-frequency interaction between the two infrared axial modes and the intensity dependent losses borne by each mode through this process. In the sum-frequency interaction between the two modes, the power contributed to the sum frequency output from each axial mode was the same. Therefore, both modes shared equally the losses that were due to the nonlinear process. In contrast, the frequency doubling losses for each axial mode were borne by that mode alone. On the other hand, the nonlinear coupling constant for sum-frequency generation was twice that of frequency doubling, and the total sum-generation output power was proportional to the square of this constant. Thus, the loss due to the sum-frequency mixing was also twice that due to the frequency-doubling for each mode. Based on such nonlinear coupling mechanism, Baer gave a full account of the dynamic green modification in the case of two longitudinal mode oscillation. However, subsequent work by several groups [15] [16] [17] have shown that it is possible to build intracavity-doubled diode-pumped lasers that do not exhibit this behaviour. A significant advance was made by Oka and Kubota [15] who used an intracavity quarter-wave plate to stabilise the SHG output, and this led them to propose that the mechanism for the instability was the nonlinear coupling of independent polarisation modes. When they inserted quarter-wave plate in the cavity to define the cavity modes into two orthogonal polarisation eigenvectors which were 45° with the ordinary and extraordinary wave polarisation axes of the KTP crystal, the SHG output was stabilised. A generalised analysis was given by Anthon et al [18] who concluded the amplitude noise as a consequence of laser bistability, and considered the bistability of an intracavity-doubled laser system as the result of two coupled nonlinearities: nonlinear cross saturation and sum-frequency generation.

Following Baer's model, a laser system with intracavity doubling and spatial hole burning is typically described by the rate equations [14]

$$\tau_c \frac{dI_j}{dt} = G_j I_j - \alpha \cdot I_j - I_j \sum_{k=1}^{m} D_{jk} \cdot I_k \tag{4.6}$$

$$\tau_f \frac{dG_j}{dt} = \gamma - G_j - 2G_j \sum_{k=1}^{m} \beta_{jk} \cdot I_k \tag{4.7}$$

where G_j is the unsaturated gain for the j_{th} mode, I_j is the unidirectional intensity for the j_{th} mode, τ_c and τ_f are the cavity round-trip time and the fluorescence lifetime of the gain medium, respectively, α is the linear loss of the cavity, γ is the small-signal gain parameter, D_{jk} is the nonlinear coupling coefficient, and β_{jk} is the cross saturation of modes j and k. The magnitude of the cross saturation depends on the depth of modulation of the standing waves. It has been assumed in above equations that there are m longitudinal modes oscillating in the cavity. Because the rate equations are quadratic, bistability, oscillation and ultimately chaotic amplitude fluctuations are unavoidable in such a system. However, there are also multiple stable points which can be found.

Many of the features of the intracavity-doubled lasers are determined by the form of D_{jk}. Doubling and sum generation are pair-wise interactions between modes; doubling mixes a mode with itself, while sum generation mixes two separate modes. All modes will have well-defined polarisations. The polarisation incident on the KTP is characterised by

$$\tan\theta = \left|E_o/E_e\right| = \left|E_x/E_y\right| \tag{4.8}$$

where o (x) and e (y) refer to the ordinary and extraordinary ray polarisation directions in the crystal. For the interaction of two modes with average frequency ω in a type-II crystal like KTP, the nonlinear coefficient is given by [19]

$$D_o = \frac{\omega^2 d_{eff}^2 L_{eff}^2}{c^3 \varepsilon_o n^3} \tag{4.9}$$

where L_{eff} is the effective length of the crystal. Phase matching consideration give [20], for parallel modes,

$$D_{jk} = D_P = D_o \cdot \sin^2(2\theta) \cdot \left| \frac{(1-\exp(i\Delta k_{jk} l_c))}{2 l_c \Delta k_{jk}} + \frac{(1-\exp(i\Delta k_{kj} l_c))}{2 l_c \Delta k_{kj}} \right|^2 \quad (4.10)$$

while for orthogonally polarised modes,

$$D_{jk} = D_S = D_o \cdot \cos^2(2\theta) \left| \frac{\tan\theta(1-\exp(i\Delta k_{jk} l_c))}{2 l_c \Delta k_{jk}} + \frac{\cot\theta(1-\exp(i\Delta k_{kj} l_c))}{2 l_c \Delta k_{kj}} \right|^2 \cdot \quad (4.11)$$

The phase mismatches are given by

$$\Delta k_{jk} = -[n_x \omega_j + n_y \omega_k - n_x(\omega_k + \omega_j)] / c \quad (4.12)$$

$$\Delta k_{kj} = -[n_y \omega_j + n_x \omega_k - n_x(\omega_k + \omega_j)] / c. \quad (4.13)$$

These are identical for frequency doubling, but need to be distinguished for sum-frequency generation.

In the phase matched region where $\Delta k \cong 0$, $D_p/D_o = \sin^2 2\theta$ and $D_s/D_o = \cos^2 2\theta$. The total green output for m phase-matched modes is given by

$$\sum_{j=1}^{m} I_j \cdot \sum_{k=1}^{m} D_{jk} I_k = D_p(I_1^2 + I_2^2) + 2D_s(I_1 I_2) \quad (4.14)$$

where I_1 and I_2 are the total intensities in each polarisation. The green output depends only on the total intensities in each polarisation. Bistability and chaos are intimately related to the existence of mode pairs that double less efficiently than they sum. If the laser is operating in one of these modes, it will induce a large nonlinear loss that will

prevent the other mode from reaching threshold. This interaction is symmetrical so that stable operation in either mode is possible. In the absence of spatial hole burning this makes the laser bistable and results in mode hops that cause large spontaneous shifts in the laser output. Adding the slow feedback mechanism of gain saturation to the system causes the laser to switch back and forth between the two stable states, leading to oscillation and chaos.

B. Stable Steady-State Operation

However, if we control the cavity intensities in each eigen-polarisation state, I_1 and I_2, as well as the polarisation angle θ with respect to the type-II doubling so that sum-frequency generation of the modes is much less efficient than the frequency-doubling, stable operation can be achieved. Eq. (4.14) also reveals the conditions for stable steady-state operation of the laser for the following cases:

(a) In the case of single-frequency operation, sum-frequency and frequency-doubling become the same process. Although the doubling efficiency may be variable subject to the nonlinear coupling and the internal losses, the steady-state operation is stable. To achieve single-frequency operation of intracavity-doubled lasers, techniques such as etalons [14], ring configurations [21], ultrashort cavity microchip lasers [22], and birefringent filters [17] [23] [24] have been used, and stable single-frequency SHG output has been successfully obtained from these lasers. However, many of these single-frequency lasers require the polarisation to be defined in the cavity. Since the birefringence of the type-II doubling crystal (KTP) is temperature sensitive, perturbations of the KTP birefringence may affect the confined polarisation state, and thus in turn reduce the reliability of the single-frequency operation and the efficiency of frequency-doubling.

(b) In the cavity with eigen-polarisations defined, when $\theta = \pi/4$, $D_s = 0$. There is no sum-frequency coupling of orthogonal modes, and the green noise can be greatly reduced. This is the technique which was used by Oka and Kubota [15] by using an intracavity quarter-wave plate with its axes 45° to the e- and o-ray polarisation axes of the KTP crystal . In the case of two orthogonal longitudinal mode operation, the process can be

understood as the exact cancellation of the two sum-frequency waves generated by two pairs of polarisation components. So no SFG signals are observed, and only SHG of each mode are generated. Such stable two mode SHG output has been experimentally observed [25]. As a special case, due to the fact that thermal induced birefringence in Nd:YAG can behave as a wave plate, a stable output can also be obtained in the cavity without any quarter wave plate [16][26]. However, owing to the arbitrary nature of such thermal birefringence, the laser medium or nonlinear crystal need to be rotated to the optimum angle, which corresponds to $\theta = \pi/4$, so that the mode coupling can be reduced to the minimum ($D_s = 0$). In the eigen-polarisation defined cavity, angle θ determines the nonlinear coupling efficiency of pairs of orthogonal modes. When $\theta < \pi/8$, D_p is less than D_s and the laser will exhibit bistability with respect to polarisation. In the cases where $\pi/8 < \theta < 3\pi/8$, the bistability is less obvious. If the difference in Δk and D_o can be neglected then D_s is less than D_p, and the polarisation-related bistability disappears. The special case is $\theta = \pi/4$, $D_s = 0$. However, because of the variations of the Δk and D_o, bistable operation can occur if there are modes that double less efficiently than they sum, even when $\theta = \pi/4$.

(c) In a cavity with an intracavity polariser, SFG coupling between orthogonally polarised modes is eliminated. The efficiency of sum-frequency generation between the parallel longitudinal modes depends on the total intensities in the e and o polarisations of the KTP crystal. Stable multi-longitudinal-mode operation can be obtained when the SFG is less efficient than the SHG. It has been observed that both SHG and SFG can exist in the stable green output [27][28]. The criteria for such operation is to reduce the longitudinal-mode number, and to enlarge the intensity ratio of the major and the minor oscillating modes so as to reduce the efficiency of SHG of longitudinal mode coupling.

Note that instability can also be induced by higher-order transverse modes. Because the nonlinear gain saturation of the intracavity-doubled laser combined with poor spatial overlap of these transverse modes increase the gain and reduce the nonlinear losses for the higher order modes, the intracavity-doubled lasers are much more prone to

multitransverse mode operation than lasers with conventional output coupling. Thus TEM_{00} operation in intracavity-doubled laser is as important as the stable longitudinal-mode operation.

Nonetheless, the presence of the nonlinear output coupling causes nonlinear gain saturation and bistability that can cause the laser to operate in a number of undesirable ways. However, with careful control of the laser cavity it is possible to overcome the fact that intracavity doubled lasers are inherently less stable than lasers with linear output coupling. And indeed, elimination of the amplitude fluctuations have been demonstrated by several different techniques. In general it can be said that in order to build an efficient intracavity doubled laser, it is desirable to have the cavity polarisation controlled and use a low loss frequency selector.

C. Frequency Selection of Intracavity Birefringent Filter

In our frequency-doubled Nd:YLF laser, we have used the KTP crystal and the Brewster plate as a novel intracavity birefringent filter to define the cavity polarisation and to select a single longitudinal oscillating mode. Such a frequency-selection technique has further been enforced by the Nd:YLF crystal which is naturally birefringent and has an anisotropic emission cross-section.

As was shown in chapter 3, the Nd:YLF laser typically runs in 5-6 linearly polarised longitudinal modes with 25 GHz regular spacing which is due to the spatial hole burning effect. When the Brewster plate is inserted into the cavity, these linearly polarised modes encounter no additional loss. However, when the birefringent KTP is inserted at an angle of 45° with respect to the linear polarisation, the linearly polarised wave in the cavity is equally split in the KTP crystal into the ordinary and the extraordinary ray components. As Fig. 4.2.1 indicates, after a round trip in the KTP crystal, each mode returns to the Brewster plate with a phase shift between its two components, which is given by

$$\delta_i = 4\pi \cdot \Delta n \cdot L_{KTP}/\lambda_i \qquad (4.15)$$

where L_{KTP} is the length of the KTP crystal, Δn of 0.0865 is the difference of the refractive index between orthogonal refractive indexes, and λ_i is the fundamental wavelength of each longitudinal mode. When δ_i is an integral multiple of π, the round-trip lightwave still has p-plane polarisation and the loss in passing through the Brewster plate will be negligible. Otherwise, the light will be elliptically polarised by the KTP crystal, so some loss will occur at the Brewster plate. Mode selection is provided because δ_i depends on λ_i, which in turn has different values for different longitudinal modes.

Using the Jones-Vector formalism [29], we can evaluate the round-trip transmittance against δ. The Jones matrix for the Brewster plate is given by

$$B = \begin{bmatrix} 1 & 0 \\ 0 & q^2 \end{bmatrix} \tag{4.16}$$

where $q = 2n/(n^2+1)$ with n as the refractive index of the glass. For fused silica (n = 1.45 at 1.047 μm), q ~ 0.935. The relevant matrices for the analysis are

$$R(\theta) = \begin{bmatrix} \cos\theta & -\sin\theta \\ \sin\theta & \cos\theta \end{bmatrix} \tag{4.17}$$

$$C(\delta) = \begin{bmatrix} e^{i\delta/2} & 0 \\ 0 & e^{i\delta/2} \end{bmatrix} \tag{4.18}$$

where R(θ) is the matrix for the rotation angle of the KTP crystal, and C(δ/2) is the matrix describing the retardation effect in the KTP crystal. The round-trip Jones matrix in this case can then be described as

$$M = BR(\theta)C(\delta/2)C(\delta/2)R(-\theta)B \tag{4.19}$$

By evaluating the matrix elements, we have

$$M=\begin{bmatrix} \cos^2\theta+\sin^2\theta\cdot e^{i\delta} & q^2\cdot\sin\theta\cdot\cos\theta\cdot(1-e^{i\delta}) \\ q^2\cdot\sin\theta\cdot\cos\theta\cdot(1-e^{i\delta}) & q^4\cdot(\sin^2\theta+\cos^2\theta\cdot e^{i\delta}) \end{bmatrix}. \tag{4.20}$$

When θ is 45°, Eq. (4.20) can be rewritten as

$$M=\begin{bmatrix} (1+e^{i\delta}) & q^2(1-e^{i\delta}) \\ q^2(1-e^{i\delta}) & q^4(1+e^{i\delta}) \end{bmatrix}. \tag{4.21}$$

The round-trip transmittance of the resonator is given by the square of the eigenvalues, t_p and t_s, of the matrix M. The eigenvalues are expressed as

$$t_{p,s}=\frac{1}{2}\left\{(1+q^4)\cdot\cos\frac{\delta}{2}\pm\sqrt{(1+q^4)^2\cdot\cos^2\frac{\delta}{2}-4q^4}\right\} \tag{4.22}$$

corresponding to the p and s plane of the Brewster plate, respectively. Fig. 4.4.1 shows the solution of $\left|t_{p,s}\right|^2$ as a function of δ.

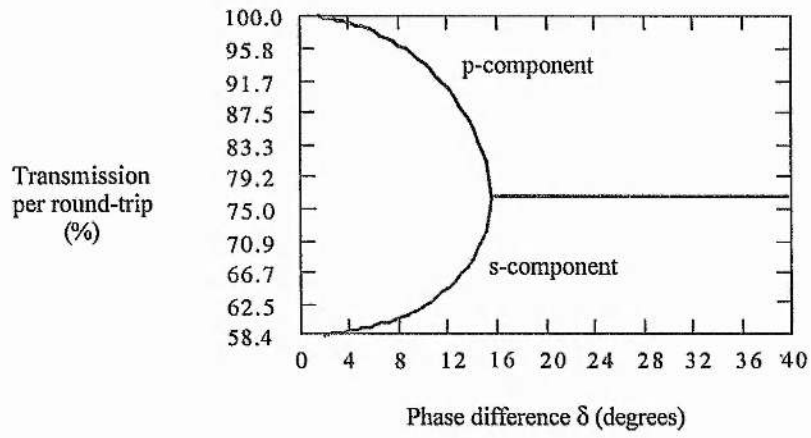

Fig. 4.4.1. Roundtrip transmittance for the eigenvalues of the resonator included the birefringent filter plotted as function of retardation δ, for the case of θ = 45°. The upper line of the graph corresponds to the p component, the lower one corresponds to the s component.

The upper line corresponds to $|t_p|^2$ and the lower one to $|t_s|^2$. These two lines join to form a single line at the angle of ~ 15.5° and the transmittance of ~ 76% corresponding to q^4. This figure indicates the zero round-trip loss occurs at $\delta = 0$ for the p-polarised light wave and that some loss is introduced for the retarded modes, hence giving the mode selection.

As an example, for the optical path length 6.0 mm, the frequency interval between longitudinal modes $\Delta\nu$ is ~ 25 GHz, which corresponds to ~ 31° of phase difference as found from Eq. (4.15). From Fig. 4.4.1, the loss is ~ 24 % at $\delta = 31°$. The frequency spacing between round-trip transmission maxima of (180°/31°) x 25 GHz ~ 145 GHz is similar with the observed gain spectral width of Nd:YLF of ~ 150 GHz. Therefore, only the single mode with $\delta = 0$ and emitting near the centre of the gain profile would be allowed to oscillate. Low overall loss and simultaneous high gain will prevail within a narrow frequency band near the centre of the gain profile.

In the above Jones-Vector analysis, the phase retardation introduced by the Nd:YLF is ignored. This is because the birefringence in Nd:YLF is so large that modes become out of phase in a fraction of the absorption depth. In addition, the ratio between the emission cross sections of the orthogonal polarisations is so significant that no gain is obtained for the modes polarised perpendicular to the c-axis of the crystal. Therefore, we have assumed that all oscillating longitudinal modes are linearly polarised along the c-axis of Nd:YLF crystal with the largest emission cross section.

D. Long Term Stability Analysis

SHG amplitude fluctuation in intracavity-doubled lasers has been a major concern for many applications, and various techniques have been developed to reduce nonlinear coupling between the cavity modes so that low noise operation becomes possible. However, long-term stability remains to be a problem. The transition from stable to unstable operation is typically very sensitive to small thermal or mechanical perturbations, and in many cases, a laser that is operating in a stable region will not restart in a stable regime when the pump diode laser is switched off for a few seconds. The sporadic nature of this low-noise regime of operation also makes it difficult to

unambiguously identify systems with good long-term stability. Many designs that can be forced into a stable region with a particular set of components will not work well with a different set of components, nor will they withstand the more rigorous regime of thermal cycling and repetitive use.

The difficulty of long-term stable operation is two-fold. Firstly, the doubling efficiency is extremely sensitive to the finesse of the laser cavity. So any loss induced by small perturbations of the intracavity components may cause dramatic reduction in the SHG output. Secondly, most of the stabilisation techniques are related to the polarisation modification of the laser modes in the doubling (KTP) crystal. However, in KTP the birefringence is temperature sensitive, and the absorption and scattering loss is dependent on both infrared and SHG intensities. So small perturbation in the KTP crystal may either disturb the stable performance or in turn reduce the doubling efficiency. It has been observed in our experiments that intracavity-doubled lasers exhibit power drifting, mode hop, and un-repeatable operation although short-term stable operation has been obtained and maintained.

Achieving an efficient intracavity doubling laser that can maintain long-term stability requires simultaneous control of a large number of parameters. It is desirable for the laser to suppress oscillation of more than one mode in the cavity and a low loss frequency-selection technique is required. Since it is critical in most cases that birefringent elements perform as a quarter-, half-, or full-wave plate, precise temperature control of polarisation retardation elements such KTP is needed. Finally, intracavity doubled lasers tend to operate in multiple transverse modes. Thus, good transverse mode control is essential to avoid oscillations involving different transverse modes. Nonetheless, it has been demonstrated that if enough constraints are placed on the cavity without introducing appreciable losses to the system, stable and efficient operation of the intracavity frequency-doubled laser is possible.

4.5 Single-Longitudinal-Mode Operation

A. SLM Operation by Using a Birefringent Filter and an Etalon

The folded-cavity diode-pumped Nd:YLF laser configuration had been described in § 3.6. When frequency-doubling the laser, we inserted the doubling crystal, the Brewster plate and an additional etalon inside the cavity. The folding mirror M1 in the fig. 3.6.1 was replaced by a high pass (HR coated @ 1047 nm; AR coated @ 523.5 nm) filter with the same curvature, and the end-mirror M2 was replaced by a dichroic plane mirror which was HR coated at both 1047 nm and 523.5 nm wavelengths. The doubling crystal was a 3 x 3 x 6 mm a-cut KTP crystal (detailed description in § 4.2). The Brewster plate and the etalon used in the experiment were two identical 2-mm uncoated fused silica plates which had a transmission band of 50 GHz. Appendix I shows a picture and the 3-D configuration of this doubled Nd:YLF laser.

From theoretical analyses, the intracavity birefringent filter formed by the Brewster plate and birefringent KTP provides significant loss on the adjacent spatial hole burning modes. Thus, the threshold for multimode operation is much higher than that for single-mode operation. In addition, the energy diffusion in the spatial hole burning gain medium and the anisotropic emission cross-section of Nd:YLF are also responsible for the high multimode operation threshold. For this reason, we are able to achieve as high as 1 W single-frequency SHG output from this device. However, by increasing the pump power, the multimode operation threshold may be exceeded allowing multimode oscillation. The birefringent filter is no longer sufficient to maintain SLM operation, and additional mode control elements such as an etalon is required.

In our experiments, the output spectrum of the frequency-doubled laser was examined by using scanning plane-parallel Fabry-Perot interferometers and a scanning confocal green interferometer. Detailed spectral characteristics were also analysed by a spectral analyser. Fig. 4.5.1 shows the typical spectral traces of the laser with varying degrees of longitudinal mode selection. At 10-W diode pump, the standing-wave Nd:YLF laser exhibits 4 spatial hole burning modes at a regular spacing of 25 GHz, as shown in fig.

4.5.1 (a). This is a direct consequence of the strong spatial hole burning effect of placing Nd:YLF gain medium at the end of the cavity. After inserting the birefringent filter into the cavity, the number of oscillating longitudinal modes is reduced. Due to the high pump power multiple adjacent spatial hole burning longitudinal modes still oscillate in the cavity, as seen in fig. 4.5.1. (b). Finally, an uncoated etalon was inserted into the cavity to eliminate adjacent modes and allow only one single longitudinal mode to oscillate. Fig. 4.5.1. (c) shows the single-frequency spectral trace of the 1 W intracavity-doubled green laser output.

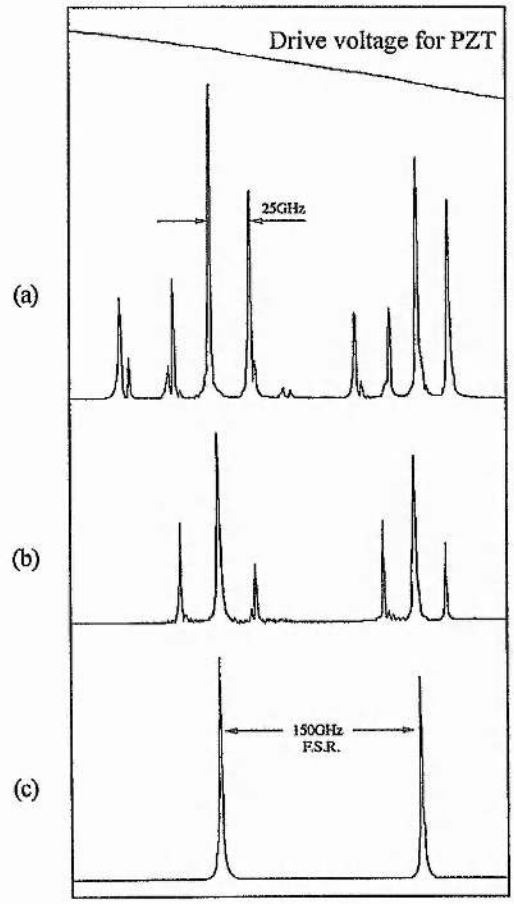

Fig. 4.5.1.

Spectral characteristics of 1-W intracavity frequency-doubled Nd:YLF laser. Traces of spectral output of the fundamental-wave from a 150 GHz FSR scanning plane-parallel Fabry-Perot interferometer for 1047 μm.

(a). spatial hole burning modes of the fundamental output;

(b). the stable fundamental spectral output of the laser, when using the composite intracavity birefringent filter at 10-W diode pump;

(c). stable single frequency SHG output, when using the birefringent filter and a 2-mm uncoated etalon.

The output spectrum of the second harmonic output has also been examined at different stages. Stable SHG single-frequency traces has been observed from the confocal green interferometer corresponding to the fundamental single frequency trace. In the case of

stable two or three longitudinal mode operation, the SHG components of each fundamental mode have been observed. The appearance of the additional components in the green spectrum is believed to be due to SFG of the fundamental modes.

Before the pump power exceeds the multimode oscillation threshold, the birefringent filter can efficiently control the single-frequency operation. It has been observed in the experiment that stable single-frequency operation can be obtained without an etalon for diode pump powers lower than 5 W. In fact, at lasing threshold a few milliwatts of single-frequency SHG have been produced even without the insertion of the Brewster plate. This is due to the fact that the anisotropic property of the Nd:YLF material gives different optical gain to those modes with different polarisations while the birefringent crystal separates those oscillating modes with different polarisations. The attainment of SLM operation by using the combination of the birefringent crystal and the anisotropic gain medium has been observed in the Nd:YVO_4 laser [22] where 16 mW of single-frequency green light has been obtained.

B. Reliability of SLM Performance

Stable single-frequency operation can be abruptly terminated by either some perturbation of the laser cavity or through a change in the KTP temperature. Sudden shock or strong vibration applied to the optical bench would switch the laser from stable SLM operation to mode characterised by chaotic intensity fluctuations. However, such process can be reversed by another shock or vibration. The mechanical instability of the cavity can also induce stable two adjacent mode oscillation or adjacent mode hopping. The stable operation is critically related to the angular alignment and positions of mirrors M1, M2 and the KTP crystal. On the other hand, stable single-mode operation is not affected by a change in the cavity length. In fact, the single-frequency green light can be continuously tuned over 9 GHz by shifting the cavity length as far as ~ 5 μm. Beyond this length, a mode hop occurs resulting in the laser frequency returning to the starting point. It is believed that the bistability of single-mode operation due to the perturbation of the cavity is subject to the mechanical instability which induces the cavity mode change

in the KTP crystal. Because the phase shift δ_i in Eq. (4.15) is dependent on both L_{KTP} and λ_i, any perturbation of the cavity mode would result in a large discrete phase shift in δ_i, which may cause mode-hops or unstable performance. The drift of KTP temperature can also induce unstable operation and mode hops. In the experiment, it has been observed that unstable operation occurs for a KTP temperature change of a 0.5 °C. However, by improving the cavity and the temperature stability, over 2 hours of continuous SLM operation has been demonstrated.

When the single-frequency SHG output is coupled into an external cavity, the feedback signal can also disturb the stable SLM operation. The feedback problem is especially serious when the SHG output is well mode-matched into a confocal external cavity. This is because the down-conversion process caused by the reflected green light can induce additional oscillations in the laser cavity. However, in practice such feedback signals can be suppressed by using an optical isolator located between the two optical resonators.

4.6 Output Power Characteristics and Spatial Mode Quality

A. 1 W Continuous-Wave Single-Frequency Intracavity SHG

When the KTP crystal, the Brewster plate and the 2-mm uncoated etalon are inserted into the cavity, stable single-frequency green light can be generated. The mirror M2 in fig. 3.6.1 is highly reflective at both the fundamental and the second-harmonic wavelengths so that the green beams generated in each direction are combined into one output which emerges from mirror M1. Since the output is diverging as it leaves the cavity, a 15-cm focal-length lens was placed near the mirror M1, yielding a collimated beam. Fig. 4.6.1 shows the single-frequency SHG output power and the total available fundamental power as a function of laser-diode pump power. 1 W of single-frequency TEM_{00} output at 523.5 nm has been obtained for ~ 10 W of pump power, resulting in a diode laser output to green output conversion efficiency of 10%. Electrical-to-optical conversion efficiency, which includes the diode laser efficiency and the coupling efficiencies, was 2.5%. At 10 W diode

pump, the green output power begins to saturate. This is due to the increased thermal lensing in the Nd:YLF crystal at high pump powers which moves the cavity out of the stability range. In the course of measuring the green power at different pump power levels, the cavity was optimised to adapt the Nd:YLF thermal lensing so as to extract the maximum green power in a single transverse mode. The procedure of optimisation of the laser cavity was simply to translate the end mirror M2 (and KTP, if necessary) back- and forth along the cavity in a range of 5 mm. Such movement can reduce the influence of the Nd:YLF thermal lensing which shifts the cavity stability range and changes the resonator mode cross-section. If the cavity is maintained at the optimum configuration for 10 W pump, the laser oscillation threshold is much higher than the value in the figure. The conversion efficiency from the fundamental wave to the single-frequency green light was around 40-50%. This is largely limited by the additional intracavity linear losses introduced by the insertion of intracavity doubling and mode selection elements. The non-optimised nonlinear coupling parameter is another factor responsible for the measured value of conversion efficiency. Note that the fundamental-to-green conversion efficiency at 5 W diode-pump is higher than that at 10 W pump. This is believed to be due to the absorption loss in the KTP crystal which dramatically increases with the intensities of both fundamental and SHG inside the KTP crystal.

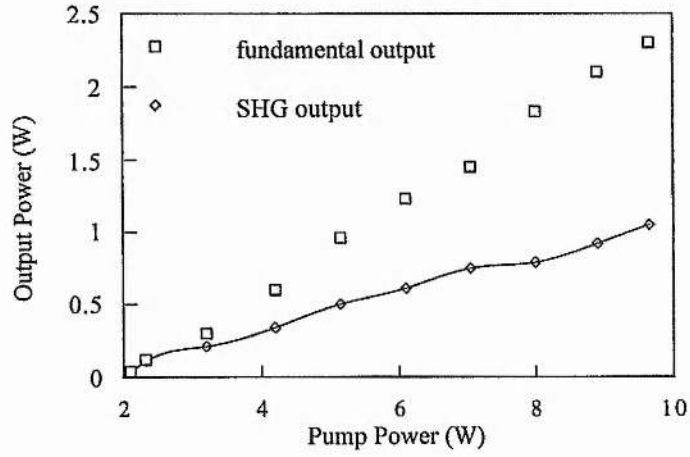

Fig. 4.6.1. Total fundamental power and intracavity single-frequency SHG output power as a function of diode-pump power.

Although the maximum extracted SHG power is limited by the linear internal loss and the nonlinear coupling parameter, other cavity elements or parameters also impose a strong influence on the SHG power. At a certain intracavity loss values, the extracted SHG power is very sensitive to the alignment with respect to the phase-matching direction and the cavity mode size in the KTP crystal. Slightly tilting the KTP angle off the phase-matching direction or translating the KTP away from the cavity mode waist may greatly reduce the SHG power. This can be considered as further decreasing the nonlinear coupling parameter which in turn reduces the conversion efficiency. Large temperature drifts (> 0.5°C) in the KTP crystal may also decrease the SHG power. This was usually accompanied with mode hopping or frequency tuning process but could be reversed by slightly tilting the crystal. The output power was typically reduced by 10-15% with the insertion of the uncoated etalon. This was attributed to the large etalon tilt angle and the associated insertion loss. Thermal distortions in the Nd:YLF crystal were relatively stable in the CW laser which allows a stable cavity mode inside the doubling crystal. However, any large change in the pump power or pump distribution required readjustment of the cavity, otherwise a power decrease or unstable operation may result. The destructive interference effects which may occur due to the two overlapped SHG outputs have not been observed. This is because the separation between mirror M2 and the KTP crystal is only millimetres and the travel range of M2 is also limited by a few millimetres, hence the the dispersion of the air path is not significant. As a reference, the 1047-523.5 nm dispersion of air is 3.6×10^{-6} which is approximately 29.0 °C/cm.

The intracavity-doubled laser tends to operate in multiple transverse modes. If any of the intracavity components have appreciable scattering or distortion it will not be possible to achieve single transverse mode operation. When the laser operates at the edge of its cavity stability range, it is also likely to oscillate in multiple transverse modes. Generally 20% higher output power and chaotic intensity fluctuations are associated with the multiple transverse mode operation. In the folded-cavity laser an intracavity aperture

is not generally required as long as the cavity is adjusted near the centre of the cavity stability range for TEM_{oo} operation.

B. Low Intensity Noise Operation

Without the Brewster plate, the green output from the laser tends to exhibit large amplitude noise. Typically the output is composed of a series of apparently random spikes superimposed upon a DC background. The interval between neighbouring spikes is a few tens of microseconds. When the birefringent filter and etalon are used in the cavity to suppress multimode operation, a remarkable noise reduction in the output intensity is achieved.

In our experiment, the laser output was monitored with a photodiode which integrated the intensity noise over a certain frequency range. Without any noise reduction system the rms noise of the green laser was less than 1% over the frequency range 10 Hz to 1 MHz. The intensity fluctuations recorded over different time-scales for the single-mode green laser are shown in fig. 4.6.2. (a), (b), (c). The laser output recorded over a few minutes time-scale is illustrated in fig. 4.6.2. (a), where a few large random spikes due to the environmental noise are clearly evident. However, in the total observed time of 7.5 minutes, the output intensity was stable to within 1% of the average output power. Mains noise at 100 Hz originating from the power supply, environmental noise and the detector exhibits a strong modulation on the output intensity. However, such modulation is still below 1% rms, as shown in fig. 4.6.2. (b). All solid-state lasers exhibit a behaviour known as relaxation oscillations which produces intensity noise in the tens to hundreds of kilohertz range. The frequency of the relaxation oscillations depends on several factors such as the upper state lifetime of the laser material, output coupler transmission, and cavity length. Fig. 4.6.2. (c) shows typical relaxation oscillations of ~ 300 kHz from the green laser. The spectral distribution of the noise was also analysed using an *RF* spectrum analyser. Thus it was further confirmed that the main source of intensity noise was at the mains frequency and the relaxation oscillation frequency. Low intensity noise is exhibited with the single-frequency operation.

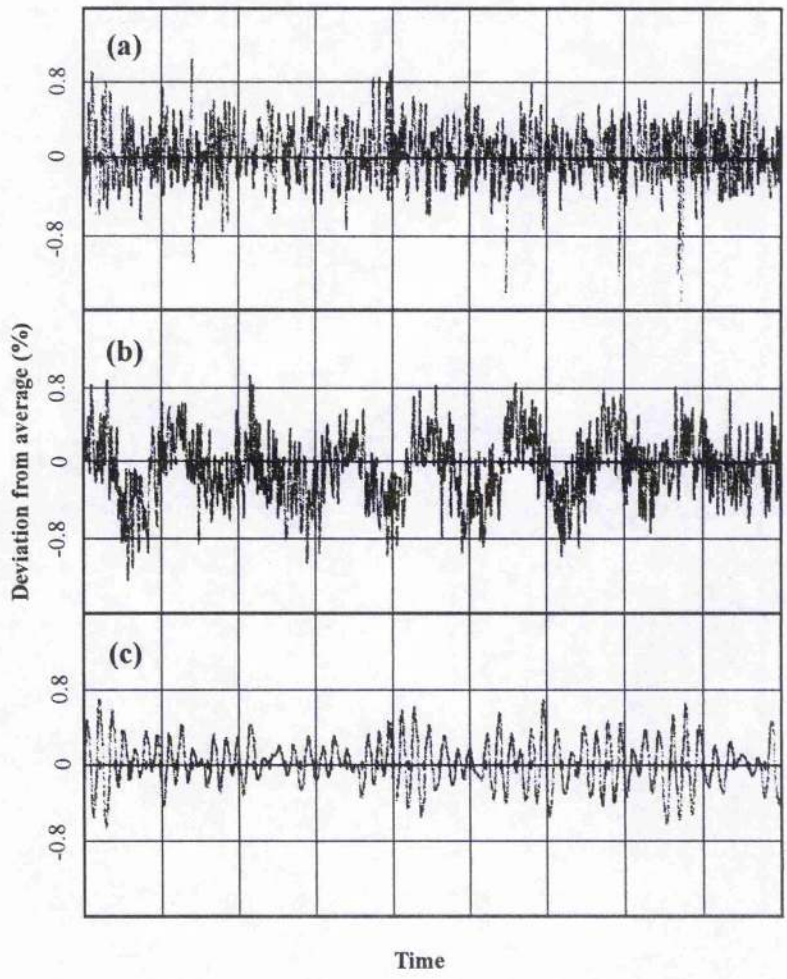

Fig. 4.6.2. Typical intensity fluctuations of the SHG output of the Nd:YLF laser recorded over three diferent time scales: (a) 50 sec/div; (b) 10 msec/div; (c) 20 μsec/div.

C. Long-Term Stability of Output Intensity

The frequency-doubled Nd:YLF laser suffers from a long-term power drifting problem. It has been observed that the SHG output slowly drifts down to approximately 1/2 - 2/3 of the initial optimised value over 1-2 hours. Short periods of mode hopping and unstable operation are also normally associated with this process. However, the reduction can be reversed to the optimised level by slightly tilting the angle of the KTP crystal, the etalon, or mirrors M1 and M2. This behaviour was first believed to be due to fluctuations

of the KTP crystal temperature. Since the KTP crystal temperature was oven controlled at 80 °C, the output power could be stabilised to within 2% of the average power level for periods of a few hours without any mode hopping. However, this technique was only relevant in the lower power regime (< 500 mW). When the operating power is above 500 mW, the output power drift persisted and was independent of any control of the KTP crystal temperature. Another characteristic of the power drifting was that the SHG output only drifted downwards rather than upwards. After the investigation of the grey-track in the nonlinear crystal, such power drift is believed to be associated with the photochchemical degradation effect in the KTP crystal.

The output power relative to the KTP crystal temperature was investigated in the following experiment. While the temperature of KTP crystal was continuously tuned from 20 °C to 55 °C, the output power was monitored with a power detector. Fig. 4.6.3 illustrates the resultant behaviour of the laser output. The solid line in the figure shows the SHG output as a function of the KTP crystal temperature when etalon was used inside the cavity; whereas the enveloped dashed line represents the output power change without the intracavity etalon. From fig. 4.6.3, it can be seen that there is a major power-temperature cycle of ~ 15 °C as well as a minor cycle of ~ 2 °C.

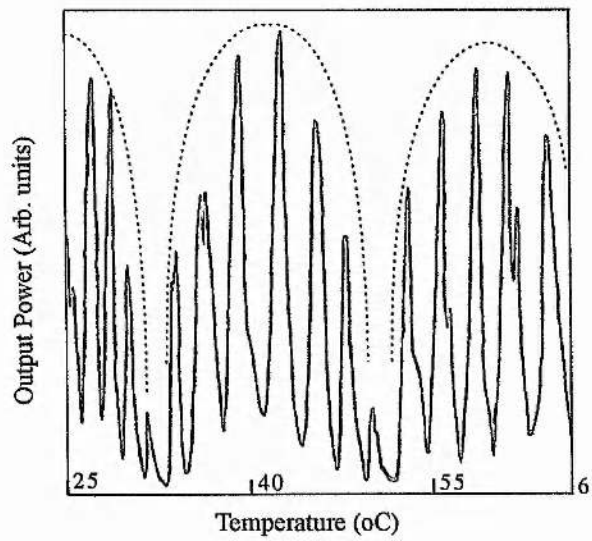

Fig. 4.6.3. Intracavity-doubled SHG output power as a function of KTP crystal temperature.

Based on the Jones-Vector analysis of the laser cavity in § 4.2, this power cycling behaviour can be understood in terms of the variation of the cavity mode polarisation which is critically dependent on the variation of the birefringence of the KTP crystal.

From Eq. (4.15) $\delta_i = 4\pi \cdot \Delta n \cdot L_{KTP}/\lambda_i$, there are hundreds of wave path difference between the extraordinary and ordinary component. Thus any small perturbation of the crystal temperature that produces a small variation of Δn and L_{KTP} subsequently causes a large change in δ_i. As the KTP crystal temperature increases or decreases, the KTP crystal may not be equivalent to a full-wave plate required for the single oscillation cavity mode. Then the resultant polarisation loss imposed by the Brewster plate results in a decrease of the output power. The KTP crystal may also gradually become a full-wave plate for another potential cavity mode. Consequently, this new cavity mode will obtain enough gain to oscillate instead of the original mode. In the fig. 4.6.3, the minor power-temperature cycle is believed to correspond to the rotation of the spatial hole burning modes as the KTP crystal becomes a full-wave plate for each of these mode in turn; while the major power cycle is believed to correspond to an extra full-wave rotation for all these modes. Note that a strong modulation was observed when the intracavity etalon was employed. This can be explained as the elimination of two mode simultaneous oscillation when none of these are under the etalon transmission maxima. The estimated value based on the above interpretation was found to be in good agreement with the experimental results.

The intracavity-doubled Nd:YLF laser is a polarisation sensitive device, and any perturbation of the intracavity birefringence or frequency drifting can cause a dramatic output power change. However, the long-term power drift exhibited by the laser is believed to be due to the absorption of the fundamental and the SHG light in the KTP crystal. As discussed in § 4.2, while the nonlinear interaction proceeds, a fraction of the radiation is absorbed, and thermal gradients are established. Thus, the spatial variation of the refractive indices slightly changes the birefringence property of the KTP crystal which

may cause the SHG power to slowly drift. On the other hand, with exposure to a combination of the high intensity second-harmonic and fundamental radiation, photochemical degradation (grey tracking) may be gradually formed in the KTP crystal and this can permanently degrade the ideal birefringence property and phase-matching condition. Using high quality crystals and operating the KTP crystal at high temperatures can help the laser to overcome the power drifting. However, an effective solution to control the birefringence in the cavity needs to be exploited.

D. Spatial Mode Quality of the Laser Output

The transverse mode properties of the second harmonic output have been examined. The beam profile is measured by a 25 μm scanning pinhole. The far-field intensity distributions is found to be very close to a Gaussian. Measurements have also been performed on the divergence properties of the SHG output, which yields an M^2 (see chapter 3 references [20] [21] for M^2 defination) value of 1.1 (± 0.8%). Fig. 4.6.4 shows the image of the output beam profile recorded on a CCD camera. The SHG output has a large beam divergence, which was measured to be ~ 14 mrad half angle. At 10 W pump the beam diameter at output mirror is 350 μm ($1/e^2$). Slight ellipticity in the cross section is also typical of the laser output. Since the output exhibits a large divergence, a 15-cm focal length lens was placed 10 cm away from the output coupler to collimate the beam.

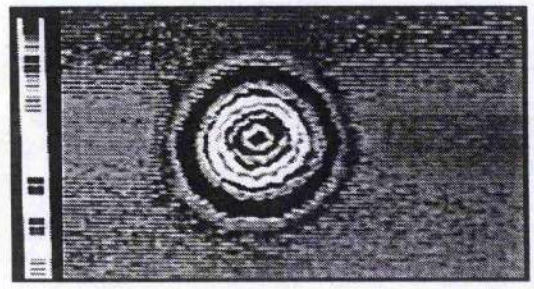

Fig. 4.6.4. The SHG TEM_{00} beam profile of Nd:YLF laser. (image from CCD camera)

The divergence of the output was found to be dependent on the diode pump power. The divergence showed a slight decrease with the increase in diode pump power

due to the influence of the thermal lensing effect in the Nd:YLF crystal where the strong thermal lens enlarges the cavity mode waist in the KTP crystal and reduces the cavity mode divergence. The transverse mode parameters also depend on the cavity configuration parameters. Changing the cavity length or folding angle can slightly change the output beam divergence and ellipticity. The measured spatial mode parameters were obtained using the configuration described in § 3.6 with a 43 cm cavity length and a 38° folding angle.

4.7 Spectral Characteristics and Frequency Tunability

A. Frequency Stability and Linewidth

The SHG output spectrum of the frequency-doubled Nd:YLF laser has been examined by using a confocal green interferometer with free spectral range of 2 GHz and a radio-frequency spectrum analyser (Hewlett-Packard HP8566B). Fig. 4.7.1 shows the single frequency trace of the 1 W green output obtained from the scanning confocal interferometer. Due to the fact that diode pumping eliminates the pump induced instabilities present in flashlamp-pumped lasers and that the use of birefringent filter and etalon suppresses the multiple longitudinal operation, the green output exhibits narrow linewidth as well as a relatively high frequency stability.

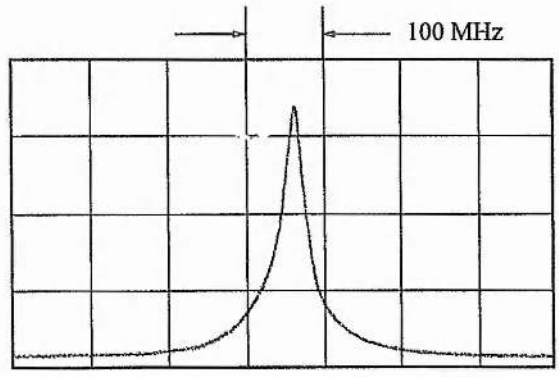

Fig. 4.7.1. Single longitudinal mode trace of the SHG output obtained from a scanning confocal optical interferometer with F.S.R. of 2 GHz.

Frequency stability refers to the jitter or drift depending on the measurement period used. Two principal effects come into play on different time scales. Frequency jitter is substantially affected by amplitude noise of the laser diode pump source and fluctuations of the optical cavity length. To reduce such frequency noise, the diode laser power supply is designed to minimise current fluctuations to less than 20 mW rms which translates directly into reduced frequency jitter. In addition, all the cavity components were bonded to a single aluminium block to reduce the mechanical vibrations and the influence of acoustic noise. Frequency drift results from changes in the KTP crystal temperature. To minimise the drift and maintain a good long-term frequency stability, accurate temperature control is crucial. In our experiment, the KTP crystal temperature was stabilised to within 0.1 °C by a crystal oven and temperature controller. With the stabilisation of the KTP crystal temperature and the reduction of environmental noise, the short term frequency jitter of the laser has observed to be less than 20 MHz and the long-term frequency drift is observed to be less than 5 GHz over the period of one hour. These frequency stability results were obtained from the scanning confocal green interferometer, so the noise of the interferometer and the ramp signal supply were also included.

The intracavity-doubled Nd:YLF laser produces single-frequency output that is relatively stable both in frequency and intensity. The output has an intrinsic linewidth that is much narrower than that of lamp-pumped lasers. A radio-frequency spectrum analyser trace of the heterodyne signal from two green lasers is shown in Fig. 4.7.2. In this experiment, the heterodyne signal was obtained by mixing the output beam of two independent single-frequency intracavity doubled green lasers on a fast photo detector. The signal from the photodiode contains the difference frequency between the laser outputs which can be displayed on a spectrum analyser. The detected phase noise of the two lasers is a measure of the linewidth over a short time period. From the figure, we can conclude that each green laser has a linewidth of less than 10 kHz over the a 10 ms spectrum analyser sweep time. Frequency jitter and drift in the beat signal preclude meaningful measurements for the sweep times required to give a resolution of better than

10 kHz. However, in order to achieve a beat signal, the two lasers must be tuned close enough together in frequency and the frequency jitter of the each laser must be kept small. The photo detector used in the experiment was a BPW28 silicon avalanche photodiode with a frequency bandwidth of 3 GHz. The radio-frequency analyser was a Hewlett-Packard HP8566B spectrum analyser. Whenever the beat signal was tuned within this range, the beat note could be recorded.

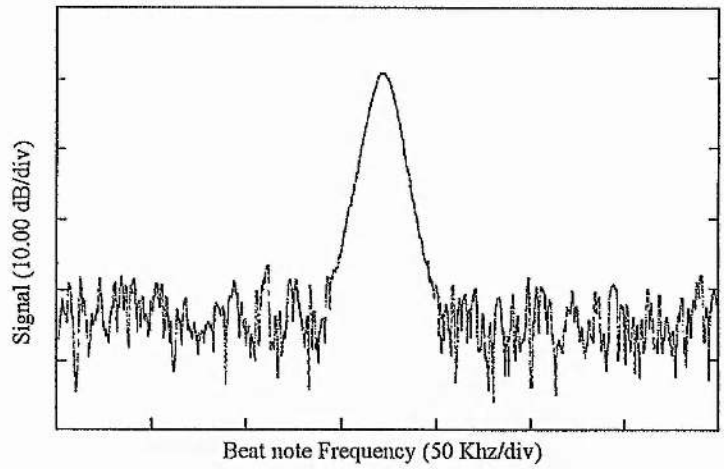

Fig. 4.7.2. Typical spectrum for the beat note of two green lasers, indicating the narrow linewidth of the green output. The center frequency is 360.85 MHz. The SHG linewidth is less than 10 kHz which is limited by the resolution of the photodetector and spectrum analyzer.

B. Frequency Tunability

Two types of frequency tunability are available with the green laser. Firstly broad tuning could be accomplished by changing the temperature of the KTP crystal or tilting the etalon. Alternatively, continuous fast tuning could be achieved by using a piezoelectric transducer bonded to the end cavity mirror. As discussed in § 4.6, by changing the KTP temperature, different spatial hole burning modes can be made to oscillate in the cavity. A tuning range as wide as 150 GHz with 12 GHz/°C tuning rate is possible. However, due to significant power changes and discontinuous mode hops, unstable operation is accompanied with this tuning process. Therefore, such a tuning technique is not utilised.

For continuous tuning, a long travel range piezoelectric transducer was bonded to the end cavity mirror which allowed the cavity length variation consistent with 12 free spectral ranges, which was 6 μm. When a voltage was applied to the piezoelectric element, a small cavity mirror translation was introduced. This resulted in tuning of the output frequency of the laser. The tuning range was measured to be about 4.5 GHz for the fundamental-frequency and 9 GHz for the SHG which was equivalent to a 725 MHz/μm cavity tuning rate (or 112.5 MHz/V voltage tuning rate). Stable single frequency operation was reliably maintained over the whole frequency tuning range. However, further tuning of the cavity length would induce a discontinuous mode hop which would result in oscillation at the original frequency. In chapter 5, this continuous single-frequency tuning technique will be utilised in a CW OPO device where 4.5 GHz continuous tuning of the signal and the idler output was obtained.

4.8 Summary and Conclusion

1 W single-frequency continuous-wave radiation at 523.5 nm has been generated from an intracavity-doubled diode-pumped Nd:YLF laser. In our laser the green noise problem has been successfully suppressed and the output has exhibited high stability both in frequency and intensity. 10 % diode-to-green conversion efficiency has been demonstrated owing mainly to the folded-cavity design and low internal loss. In this chapter, the operating characteristics of the laser have been investigated in detail, and table 4.1 summarises some of the laser parameters and operating characteristics which were typically measured in the experiment.

Theoretical analysis and discussion of efficient intracavity frequency doubling, the green noise problem, and conditions for achieving stable intracavity SHG has also been carried out. In addition, we have investigated the influence of the birefringent filter on the single longitudinal mode operation by examining the cavity mode polarisation characteristics. These analyses and theoretical expectations have been largely confirmed by the experimental results.

In the frequency-doubled laser, the intracavity birefringent filter which consists of the KTP crystal and Brewster plate plays an important role. It not only makes the single frequency operation possible but serves to minimise the intracavity loss, and provides a base for frequency tuning. On the other hand, the temperature sensitivity and absorption loss of the KTP crystal degrade the laser performance, resulting in a SHG output power drift, multimode oscillation or even unstable operation. However, through careful control of the KTP crystal temperature and the laser cavity adjustment, long-term stable operation was possible. The birefringent filter technique needs to be exploited in future work. It is suggested that by using of high quality KTP crystals with accurate temperature control or electro-optic control in conjunction with multiple Brewster plates, the birefringent filter technique may be further enhanced resulting in the long-term stable operation.

Table 4.1 Summary of the optical parameters and operating characteristics of the doubled Nd:YLF laser for the second harmonic and the fundamental-wave

Wavelength	*523.5 nm*	*1047 nm*
CW Power	1 W	2.5 W
Spatial Mode	TEM_{oo}	TEM_{oo}
M^2	1.1 ± 0.8%	1.12 ± 0.8%
Longitudinal Mode	Single-Frequency	Multimode
Amplitude Noise (10 Hz - MHz)	< 1% rms	NA
Stability of Output Power	< 2% / 2 hrs	NA
Linewidth	10 kHz/msec	NA
Jitter	< 20 MHz / sec	NA
Drift	~ 5 GHz/hr	NA
Continuous Tuning Range	9 GHz	----
Polarisation, ratio	linear, 100 / 1	linear, 100 / 1
Waist, from output mirror	5.5 cm, inside laser	5.5 cm inside laser
Ellipticity	1 : 1.1	NA

Diameter, at output mirror, ($1/e^2$)	700 μm	NA
Divergence, full angle	~ 28 mrad	NA
Pump Power	10 W	10 W

References

[1] Fujian Castech Crystals, Inc., "Data sheet KTP", Fuzhou, China, 1994.

[2] B. K. Vainshtein, "Modern crystallography I", *Springer Ser. Solid-State Sci.*, vol. 15, 1981.

[3] Y. S. Lin, D. Dentz and R. Belt, "High-average-power intracavity second-harmonic generation using $KTiOPO_4$ in an acousto-optically Q-switched Nd:YAG laser oscillator at 5 kHz", *Opt. Lett.*, vol. 9, pp. 76-78, 1984.

[4] J. C. Jacco, G. M. Loiacono, M. Jaso, G. Mizell, and B. Greenberg, "Flux growth and properties of $KTiOPO_4$", *J. Cryst. Growth*, vol. 70, pp. 484, 1984.

[5] J. Q. Yao and T. S. Fahlen, "Calculations of optimal phase match parameters for the biaxial crystal $KTiOPO_4$", *J. Appl. Phys.*, vol. 55, pp. 65, 1984.

[6] H. Ito, H. Naito and H. Inaba, " Generalised study on angular depandence of induced second-order nonlinear optical polarisations and phase matching in biaxial crystals" *J. Appl. Phys.*, vol. 46, pp. 3992-3998, 1975.

[7] T. Y. Fan, C. E. Huang, B. Q. Hu, R. C. Eckardt, Y. X. Fan, R. L. Byer, and R. S. Feigelson, "Second harmonic generation and accurate index of refrative measurements in flux-grown KTiOPO4", *App. Opt.*, vol. 26, pp. 2390-2394, 1987.

[8] Z. Y. Ou, S. F. Pereira, E. S. Polzik, and J. J. Kimble, "85% efficiency for CW frequency doubling from 1.08 to 0.54 μm", *Opt. Lett.*, vol. 17, pp. 640-642, 1992.

[9] T. A. Driscoll, H. J. Hoffman, R. E. Stone, and P. E. Perkins, "Efficient second harmonic generation in KTP crystals", *J. Opt. Soc. Am. B*, vol. 3, pp. 683-686, 1986.

[10] J. K. Tyminsk, "Photorefractive damage in KTP used as second-harmonic generator", *J. Appl. Phys.*, vol. 70, pp. 5570-5576, 1991.

[11] H. Van herzeele, "Optimisation of a CW mode-locked frequency-doubled $Nd:LiYF_4$ laser", *Appl. Opt.*, vol. 27, pp. 3608-3615, 1988.

[12] R. G. Smith, "Theory of intracavity optical second harmonic generation", *IEEE J. of Quant. Electron.*, vol. 6, pp. 215-223, 1970.

[13] J. P. Meyn and G. Huber, "Efficient intracavity second-harmonic generation in neodymium laser by using short KTP crystals" *Tech. Dig. CLEO'95*, paper CTuG1.

[14] T. Baer, "Large-amplitude fluctuations due to longitudinal mode coupling in diode-pumped intracavity-doubled Nd:YAG lasers", *J. Opt. Soc. Am. B*, vol. 3, pp. 1175-1180, 1986.

[15] M. Oka and S. Kubota, "Stable intracavity doubling of orthogonal linearly polarised modes in diode-pumped Nd:YAG lasers", *Opt. Lett.*, vol. 13, pp. 805-807, 1988.

[16] G. E. James, E. H. Harrel, C. Bracikowski, K. Wiesenfeld, and R. Roy, "Elimation of chaos in an intraccvity-doubled Nd:YAG laser", *Opt. Lett.*, vol. 15, pp. 1141-1143, 1990.

[17] T. Y. Fan, "Single-axial mode, intracavity doubled Nd:YAG laser", *IEEE J. of Quant. Electron.*, vol. 27, pp. 2091-2093, 1991.

[18] D. W. Anthon, D. L. Sipes, T. J. Pier, and M. R. Ressl, "Intracavity doubling of CW diode-pumped Nd:YAG lasers with KTP", *IEEE J. of Quant. Electron.*, vol. 28, pp. 1148-1157, 1992.

[19] M. J. Weber, Ed. "Handbook of laser Science and Technology", *Boca Raton, FL:CRC*, vol. 3, pp. 3-296, 1986.

[20] Y. R. Shen, "The principles of nonlinear optics", *New York: Wiley*, pp. 38-40, 1984.

[21] W. A. Clarkson, K. I. Martin, and D. C. Hanna, "High-power single-frequency operation and efficient intracavity frequency doubling of a Nd:YAG ring laser end-pumped by a 20W diode bar", *Tech. Dig. CLEO'95*, paper CMD8.

[22] T. Sasaki, T. Kojima, A. Yokotani, O. Oguri, and S. Nakai, "Single-longitudinal-mode operation and second-harmonic generation of Nd:YVO4 microchip lasers", *Opt. Lett.* , vol. 16, pp. 1665-1667, 1991.

[23] H. Nagai, M. Kume, I. Ohta, H. Shimizu, and M. Kazumura, "Low-noise operation of a diode-pumped intracavity-doubled Nd:YAG laser using a Brewster plate", *IEEE J. of Quant. Electron.*, vol. 28, pp. 1164-1168, 1992.

[24] J. Zhang and A. J. Henderson, "1-W single-frequency intracavity-doubled diode-pumped Nd:YLF laser", *experiments in J. F. Allen Physics Research Laboratories*, St. Andrews, 1994.

[25] L. Y. Liu, M. Oka, W. Wiechmann, and S. Kubota, "Longitudinally diode-pumped continuous-wave 3.5 W green laser", *Opt. Lett.*, vol. 19, pp. 189-191, 1994.

[26] L. R. Marshall, A. D. Hays, A. Kaz, and R. L. Burnham, "Intracavity doubled mode-loked and CW diode-pumped lasers", *IEEE J. of Quant. Electron.*, vol. 28, pp. 1158-1163, 1992.

[27] K. Suzuki, K. Shimomura, A. Eda, and K. Muro, "Low-noise diode-pumped intracavity-doubled laser with off-axially cut Nd:YVO_4", *Opt. Lett.*, vol. 19, pp. 1624-1626, 1994.

[28] N. Mackinnon, "Microchip laser: an investigation of transver-mode definition, spectral selectivity and novel frequency modulation/up-conversion techniques", *PhD. dissertation*, St. Andrews University, 1994.

[29] R. C. Jones, "A new caculus for the treatment of optical systems I. Description and discussion of the calculus", *J. Opt. Soc. Am.*, vol. 31, pp. 488-493, 1941.

Chapter 5

TUNABLE CW SINGLE-CAVITY OPTICAL PARAMETRIC OSCILLATOR

5.1 Introduction

Doubly resonant optical parametric oscillators (DROs) are the type of OPO that can be routinely operated above the CW threshold and have great potential for generating narrow-linewidth coherent radiation. Theoretical study [1] of the quantum fluctuations of DRO shows that such devices could reproduce the statistical properties of the pump light with little additional noise. In the quantum-mechanical analysis, the diffusion of the sum of the signal and the idler wave phases follows the phase diffusion of the pump wave, and the phase difference of the two waves undergoes additional phase diffusion. Therefore, the linewidth of the signal and idler wave have two noise sources: the fluctuation of the input pump and the diffusion of the phase difference. Typically, the phase difference diffusion linewidth is in the millihertz range and the OPO output linewidth are essentially limited by the pump laser. The recent coherence measurements of the output of a monolithic CW DRO [2] have confirmed such unique coherence properties.

The double-resonance condition, in terms of energy conservation, phase matching, and simultaneous resonance of signal and idler waves [3], offers the advantage of a lower threshold for parametric oscillation than in single resonance and provides additional frequency selection in OPO operation. However, this overconstrained condition also brings a considerable increase in the complexity of tuning, with more restrictive tolerances on pump stability and cavity stability. As a result, continuous frequency tuning is difficult in DROs, which typically tune with axial mode hops over a free spectral range and cluster jumps over a number of axial modes. The complications in the frequency-tuning characteristics of these devices have been studied by Eckardt *et al.* [4] in type-I

phase-matching case, and by Debrisschert *et al.* [5], and Lee and Wong [6] in type-II phase-matching case. Although double-resonance condition exists in groups of resonant cavity lengths where different modes of clusters may be partially overlapped, continuous frequency tuning is in theory possible through the simultaneous adjustment of two or three parameters, while maintaining the single-mode-pair oscillation condition.

By utilising the stability of monolithic devices, Nabors *et al.* [7] have demonstrated single-mode-pair operation of a type-I $LiNbO_3$ DRO. With the DRO servo locked to a particular axial mode-pair, the DRO signal frequency could track laser frequency tuning by as much as 90 MHz. Coarse tuning of the output wavelengths was accomplished by adjusting the crystal temperature and fine control of applied electric field. Lee and Wong [6] have systematically tuned a type-II KTP DRO over a range of ~ 3 THz through crystal angle tuning and cavity-length scanning. They achieved continuous tuning over the 0.5-GHz range through the use of temperature and electro-optic tuning of the KTP crystal. However, in general, for a fixed pump frequency, and by simply changing the common cavity length, a single-cavity could not be used to continuously tune the output while maintaining both the signal and idler fields on resonance. To achieve significant degrees of continuous tuning with a fixed frequency pump source, it is essential to have independent control of the signal and idler cavity lengths. Recently, Colville *et al.* [8] investigated, both theoretically and experimentally, the frequency-tuning and control of a dual-cavity device in which independent control of signal and idler cavity lengths became possible. Such a novel configuration greatly extended the range of continuous tuning and could overcome the continuous tuning difficulty. But dual-cavity configuration also brought about the complexity of alignment and difficulty of operating low-loss beamsplitter in potentially widely tunable type-I DROs. Independently tuning the pump frequency while servo locking the DRO cavity on single-mode resonant was a promising approach for continuously tuning DRO's. This method relaxed the critical conditions of multiple parameter tuning and opened up the possibility for extensive smooth frequency tuning of the OPO outputs.

The stability requirements on the pump frequency and DRO cavity length for the stable single-mode-pair operation may well be different in the cases of type-I and type-II phase-matching configuration near frequency degeneracy or away from degeneracy. The most important parameter is the mismatch in the free spectral ranges of the signal and idler cavity, regardless of the phase-matching geometry. The orthogonal signal and idler polarisation of type-II phase-matching offers significant advantages over type-I geometry with respect of the stability requirements and continuous tuning. Computer modelling of two typical type-I and type-II DROs [9] for single-mode-pair oscillation shows that the required pump stability is in the range of ~ 10 MHz for type-II and of ~ 0.1 MHz for type-I phase-matching and the required cavity stability is ~ 1 nm for type-II and ~ 0.1 nm for type-I phase-matching. Although stable operation of type-I DROs has been demonstrated, the stability requirement for such operation can only be provided in monolithic devices, and continuous tunability of such devices is limited. Compared to type-I, type-II geometry has more stability tolerance for single-mode operation. Thus, the stability of conventional DPSSL-pumped single-cavity DRO is well enough for single-mode operation. In addition, by means of pump frequency tuning and DRO cavity locking on resonance, a relatively wide range of continuous frequency tunability can be achieved in type-II geometry.

In this chapter, we use frequency-doubled diode-pumped Nd:YLF laser as the pump source, and LBO and KTP as nonlinear media to demonstrate single-cavity DROs. By way of theoretical analysis and demonstration of experimental results, we contrast the influence of type-I and type-II phase matching on tuning behaviour and stability requirements of DROs. Specifically for near-degenerate operation, we illustrate the advantage of type-II compared with type-I phase matching in obtaining single-mode-pair output. Based on the type-II phase-matched DRO, by means of pump frequency tuning while servo controlling the cavity length to maintain the single-mode-pair oscillation condition, we have achieved 4.5 GHz continuous tuning in a low-threshold DRO.

5.2 Single-Mode-Pair Oscillation Conditions and Tuning Characteristics of Doubly Resonant OPO

A. Simultaneously Oscillating Conditions in DRO

Because of the weakness of three-wave parametric coupling, it is usually necessary to use a doubly or even triply resonant optical cavity to obtain a threshold that is low enough to be achieved with available CW pump lasers. To continuously operate a DRO, four conditions must be satisfied simultaneously and constantly: energy-conservation, phase-matching, and cavity resonance for signal and idler frequencies. The energy-conservation condition of OPO can be expressed as

$$\nu_p = \nu_s + \nu_i \tag{5.1}$$

where an input pump wave at frequency ν_p can provide gain at two lower frequencies, called the signal ν_s and the idler ν_i. The parametric interaction is phase-dependent, and proper phasing is required for energy to flow from the pump field to the signal and idler fields. The ratio of ν_s and ν_i is determined by the phase matching within the crystal which is essentially the conservation of momentum. Phase matching is described by the wave-vector mismatch which, in the case of perfect collinear phase matching, can be expressed by the scalar relationship

$$\Delta k = k_p - k_s - k_i = \frac{2\pi}{c}(n_p\nu_p - n_s\nu_s - n_i\nu_i) = 0 \tag{5.2}$$

where k_p, k_s, and k_i are the respective wave-vector magnitude of the pump, the signal, and the idler waves, with corresponding indices of refraction given by n_p, n_s, and n_i, and c is the velocity of light. Generally, useful parametric gain exists in the range of signal and idler frequencies for which $|\Delta k| \leq \pi/l$, where l is the length (mode overlap length in the material when large walk-off is exhibited) of the nonlinear material. Phase matching is usually achieved by exploiting the birefringence and dispersion properties of anisotropic

crystals. The birefringence of nonlinear crystal can be tuned by applying a stress or voltage, varying the temperature, or varying the angle of propagation. Accordingly, a set of ν_s ν_i, & ν_p satisfied in Eq. (5.2) correspond to the coarse frequency tuning of OPOs. Phase matching determines the spectral width of the parametric gain, and it is the major factor in determining broad tuning properties of an OPO. Cavity resonance have the major effect on details of frequency tuning.

In DRO cavity, feedback is provided at both signal and idler fields. We denote the signal (idler) empty cavity-length by $L_{s(i)}$, and the length of the OPO crystal by l. The resonance condition for the signal (idler) is,

$$\nu_{s(i)} = \frac{m_{s(i)} \cdot c}{2 \cdot \left[L_{s(i)} + (n_{s(i)} - 1)l\right]} \tag{5.3}$$

where $m_{s(i)}$ is the longitudinal mode number of the signal (idler), and $n_{s(i)}$ is the refractive index of the signal (idler) within the nonlinear material.

Fig. 5.2.1 schematically shows the four conditions that need to be satisfied for signal-idler mode-pair to be resonant in DROs. The cavity modes are plotted as a function of the respective frequencies and divided into possible signal resonant modes ν_s and idler resonant modes ν_i. All vertical lines in the figure satisfy energy conservation condition Eq. (5.1). The upper curve represents the parametric gain of OPO which is defined by the phase matching condition Eq. (5.2) in nonlinear crystal. If a signal-idler resonance pair lies on a vertical line, it satisfies the simultaneous resonance conditions. Thus, such mode is most favourable for parametric oscillation.

As shown in the figure, when cavity length varies due to the tuning parameters change, the position of the resonance will advance along the scales - one to the left and another to the right - at slightly different rates because of dispersion. But the scale will not change. When the pump frequency is changed, the frequencies of the cavity resonance will not change, but one of the frequency scales will be displaced with respect to another, and the respective resonance will also move with that scale. Two types of discontinuous

frequency shift are indicated in Fig. 5.2.1 as a consequence of tuning parameter change described above. One is an axial mode hop, and the other is a cluster jump. As the tuning variable changes, better coincidence in satisfying Eqs. (5.1) (5.2) is attained on the adjacent signal-idler mode-pair. Thus, resonant frequencies are favourable to hop to the adjacent modes, to one higher in frequency and the other lower. This type of discontinuous frequency change is referred to as a mode hop.

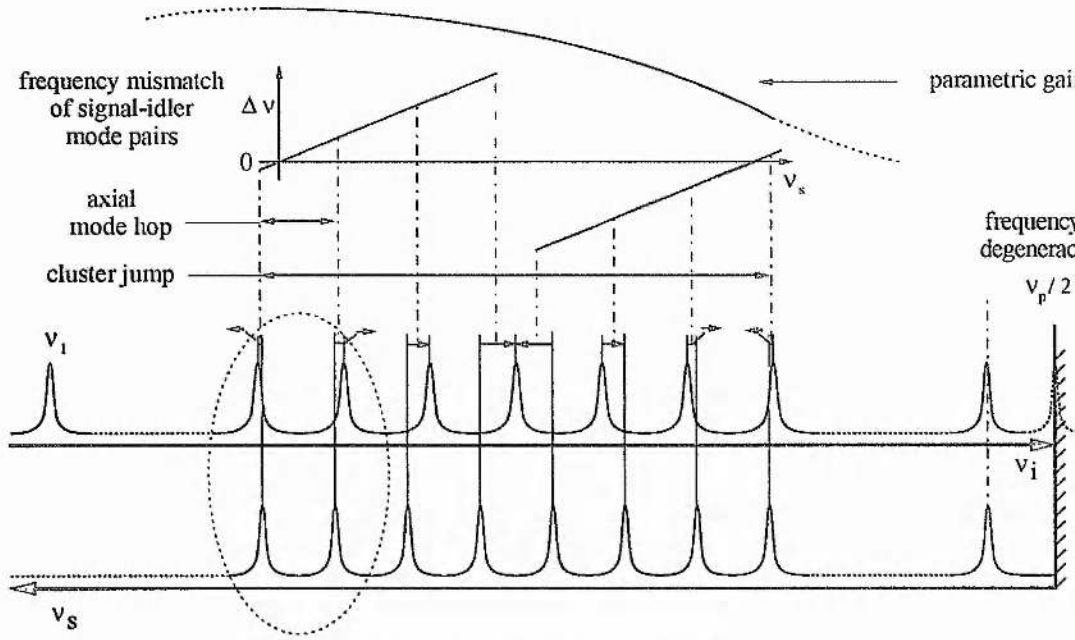

Fig. 5.2.1. Diagram that shows the relationship between the DRO signal and idler resonance frequencies, the conservation-of-energy, and the phase-matching condition. The right end side line is the $\nu_p / 2$ frequency scale. The possible idler resonances modes ν_i are plotted on an ordinary linear scale, with frequency increasing from left to right. The possible signal resonance modes ν_s are on the same reversed linear scale, therefore, frequency increases from right to left. A signal-idler mode-pair with both resonances centered on the same vertical line is in coincidence, satisfying conservation of energy. If it is also in the phase-matching region, such mode pair is most favorable for parametric oscillation. In general there will be some frequency mismatch for each mode pair. The frequency mismatch is the frequency shift that is required in order for either signal or idler resonance to produce coincidence. The difference of free spectral ranges of signal and idler cavity is exaggerated in this schematic representation.

On the other hand, as the tuning variable changes, the phase matching condition of oscillating mode also changes, and at some point it may be advantageous for the oscillation to jump to the next cluster. When the tuning variable continuously changes, the signal and the idler oscillation frequency progresses along one cluster curve in a series of mode hops until another cluster curve more closely approaches phase matching. At that

point, a large frequency change takes the oscillation to the next cluster. This is a cluster jump.

B. Mode Hop and Cluster Jump Conditions

From Eq. (5.3), a change in the length of the signal (idler) cavity of $\delta L_{s(i)}$ causes the resonant frequency of the signal (idler) field to change by $\delta \nu_{s(i)}$ and such that,

$$\delta \nu_{s(i)} = \frac{-\delta L_{s(i)} \cdot \nu_{s(i)}}{L_{s(i)} + (n_{s(i)} - 1) \cdot l}. \tag{5.4}$$

In the cases of type-II phase-matching and non-degenerate type-I phase-matching, in order to calculate numerical values for the tuning rates, dispersion terms are ignored and Eq. (5.4) can be rewritten as

$$\delta \nu_{s(i)} \approx \frac{-2 \cdot \delta L_{s(i)} \cdot \nu_{s(i)} \mathrm{FSR}_{s(i)}}{c} \tag{5.5}$$

where $\mathrm{FRS}_{s(i)}$ is the free spectral range of the signal (idler) cavity. As a tuning parameter, such as the cavity length, is continuously adjusted, the mode coincidence can be produced at some position, then simultaneous resonance of signal-idler mode pairs occurs. However, in general, the coincidence is usually not perfect, and oscillation of signal-idler mode pairs will be determined as a compromise between the optimum phase matching condition and the requirement that the frequencies satisfy the conservation of energy. Within the phase-matching bandwidth, there are often a number of potential mode-pairs for the OPO to oscillate. So, comparatively, small changes in either the cavity mode frequencies or the pump-frequency cause the OPO output to switch from one mode-pair to another. Depending on the mismatch in the FSRs of the signal and idler cavity and their cavity finesses, the new mode-pair is either adjacent to (a mode-hop) or separated by many mode pair from (a cluster-hop) the original .

The frequency mismatch $\Delta\nu$ of a signal-idler mode pair can be defined as the shift required in either the signal or the idler frequency in order to bring the two resonance into coincidence to satisfy Eq. (5.1). It is convenient to express the frequency mismatch as the sum of two components:

$$\Delta\nu = \Delta\nu_s + \Delta\nu_i. \tag{5.6}$$

Here $\Delta\nu_{s(i)}$ is the frequency shift from the peak of the signal (idler) resonance to the signal (idler) frequency that is most favourable for oscillation for that mode pair [satisfy Eq. (5.1)]. As illustrated in Fig. 5.2.1, the directions of signal and idler scale are opposite. The component of signal-idler mode pair mismatch $\Delta\nu_{s(i)}$ can be corrected by the resonant frequency change $\delta\nu_{s(i)}$ respectively. Thus, we equate $\Delta\nu_{s(i)}$ to $|\delta\nu_{s(i)}|$ in the Eq. (5.5)

$$\Delta\nu = \Delta\nu_s + \Delta\nu_i \approx \frac{2\cdot(\Delta L_s \nu_s \,\mathrm{FSR}_s + \Delta L_i \nu_i \,\mathrm{FSR}_i)}{c}. \tag{5.7}$$

Therefore, any frequency mismatch $\Delta\nu$ of signal-idler mode-pair can be compensated simply by adjusting the tuning parameter e.g. cavity length or pump frequency.

The mismatch in the free spectral ranges of signal and idler cavity is defined as $\Delta\mathrm{FSR}$, where

$$\Delta\mathrm{FSR} = \mathrm{FSR}_i - \mathrm{FSR}_s \approx \frac{c\cdot l\cdot \delta n}{2\cdot[L+(\bar{n}-1)\cdot l]^2} \tag{5.8}$$

where δn is the difference in the refractive indices of the signal and idler frequencies within the nonlinear medium, such that $\delta n = |n_s - n_i|$, $\bar{n}$ is the average refractive index given by $\bar{n} = (n_s + n_i)/2$ and $\bar{L}$ is the average (empty) optical cavity length. The mismatch of free spectral range $\Delta\mathrm{FSR}$ dictates the level of cavity-length/pump-frequency detuning, which is required to cause a hop to an adjacent mode-pair. Assuming that the

original mode-pair is exactly on resonance, then by changing the frequency mismatch $\Delta\nu$ of cavity modes by a total amount equal to the mismatch in the FSRs, a mode-hop will occur. Therefore, the condition for a mode-hop is given by

$$\Delta\nu = \Delta\mathrm{FSR}. \tag{5.9}$$

For a single-cavity OPO within which the signal and idler fields are resonant in the same cavity, the change in cavity length required to achieve a mode hop is

$$\Delta L_{hop} \approx \frac{\Delta\mathrm{FSR}}{2\mathrm{FSR}} \cdot \lambda_p \tag{5.10}$$

where λ_p is the free-space pump wavelength. This expression is under the assumption that the cavity length detuning and the FSRs of the signal and idler frequencies are approximately equal; i.e. $\Delta L_s = \Delta L_i = \Delta L$ and $\Delta\mathrm{FSR}_s = \Delta\mathrm{FSR}_i = \Delta\mathrm{FSR}$. Substituting for the refractive indices and cavity lengths, as given by Eq. (5.8), in Eq. (5.10), the mode hop cavity detuning ΔL_{hop} can also be written as

$$\Delta L_{hop} \approx \frac{\lambda_p}{2} \cdot \frac{\delta n \cdot l}{[L + (\overline{n} - 1) \cdot l]}. \tag{5.11}$$

In the case of degenerate type-I phase-matching, although the expressions for mode hop of cavity length detuning are the same as (5.10) and (5.11), the mis-match of the free spectral range is actually due to the dispersion of refractive index instead of birefringence.

The second parameter that affects the tuning behaviour of the OPO is the pump frequency. The change in pump frequency required to cause a mode-hop is given by

$$\Delta\nu_{p-hop} = \Delta\mathrm{FSR}. \tag{5.12}$$

In addition to the mode-hop, the detuning required to produce a cluster jump is also of interest. This is particularly the case if the OPO is operating with a relatively small FSR/ΔFSR or high cavity finesse when a simultaneous resonance of a signal and idler mode pair in the centre of phase-matching is not guaranteed. The number of modes of signal and idler $N_{s(i)}$ between clusters is given simply by

$$N_i = \left[\frac{\overline{\mathrm{FSR}}}{\Delta\mathrm{FSR}}\right]_{\mathrm{next-bigger-integer}}$$
$$N_s = \left[\frac{\overline{\mathrm{FSR}}}{\Delta\mathrm{FSR}}\right]_{\mathrm{next-smaller-integer}} \qquad (5.13)$$

where $\overline{\mathrm{FSR}}$ is the average of signal and idler FSRs. It is obvious that from the main cluster to the adjacent clusters we have $N_s - N_i = 1$. Therefore, from Eqs. (5.10) and (5.12) we can obtain the cavity length detuning $\Delta L_{cluster}$ or pump frequency detuning $\Delta\nu_{p-cluster}$ that is required to move from the centre of one cluster to the next, in respect of standing in a fixed phase-matching bandwidth,

$$\Delta L_{cluster} \approx \frac{\lambda_p}{2} \qquad (5.14)$$

and

$$\Delta\nu_{p-cluster} \approx \mathrm{FSR}. \qquad (5.15)$$

However, the important cluster jump parameter is the cavity length detuning ΔL_{jump} which enables the oscillating mode to jump into the adjacent cluster. It can be written as

$$\Delta L_{jump} \approx \left[\frac{\left|N_s \cdot \mathrm{FSR}_i - N_i \cdot \mathrm{FSR}_s\right|}{\overline{\mathrm{FSR}}}\right] \cdot \frac{\lambda_p}{2}. \qquad (5.16)$$

Expression (5.16) can also be approximated in terms of the pump wavelength and the integral number of ΔL_{hop}, i.e.

$$\Delta L_{jump} \approx \frac{\lambda_p}{2} - N_i \cdot \Delta L_{hop}. \tag{5.17}$$

Similarly, the pump frequency detuning for cluster jump is

$$\Delta \nu_{p-jump} \approx \left| N_s \cdot \mathrm{FSR}_i - N_i \cdot \mathrm{FSR}_s \right|. \tag{5.18}$$

Fig. 5.2.2 shows the mode-hop and cluster jump behaviour of signal modes via cavity length detuning at a fixed phase-matching condition. In the figure, there are a number of clusters existing in the phase-matching range and cavity length variation. As cavity length detunes, the oscillation mode can progress along cluster curves with a series of FSR discontinuous frequency change, or jump into adjacent cluster with N_s times FSRs discontinuous frequency change. It is also obvious that while the cavity length sweeps, the oscillation mode is hopping away from the optimum phase-matching range along its cluster curve, at the same time, the oscillating modes in the adjacent cluster is brought into the optimum phase matching bandwidth. In practice, depending on the phase-matching condition, resonator characteristics, material dispersion, and pump power level, the mode-hop and the cluster-jump behaviour via cavity length or pump frequency detuning may well be different. Generally, in near degenerate type-I single-cavity DRO the mismatch in the free spectral range of signal and idler cavity is only contributed by the dispersion term in the nonlinear crystal. From Eq. (5.13), the large N_s number forces the frequencies of the adjacent cluster mode pair out of the phase-matching range. The very small ΔFSR in type-I phase-matching makes the cavity extremely sensitive to mode hops. Single-mode-pair operation is difficult since any fluctuation in the cavity length or pump frequency can easily give rise to a discontinuous mode hop. In type-II single-cavity geometry, even at degeneracy, the free spectral range mismatch term ΔFSR is relatively large compared to that of type-I case. This is due to the birefringence of nonlinear crystal. Both mode hop and cluster jump are likely to happen when detuning the cavity length.

The large ΔFSR widens the gap of ΔL_{hop} and thus relaxes the single-mode-pair operation condition in such geometry.

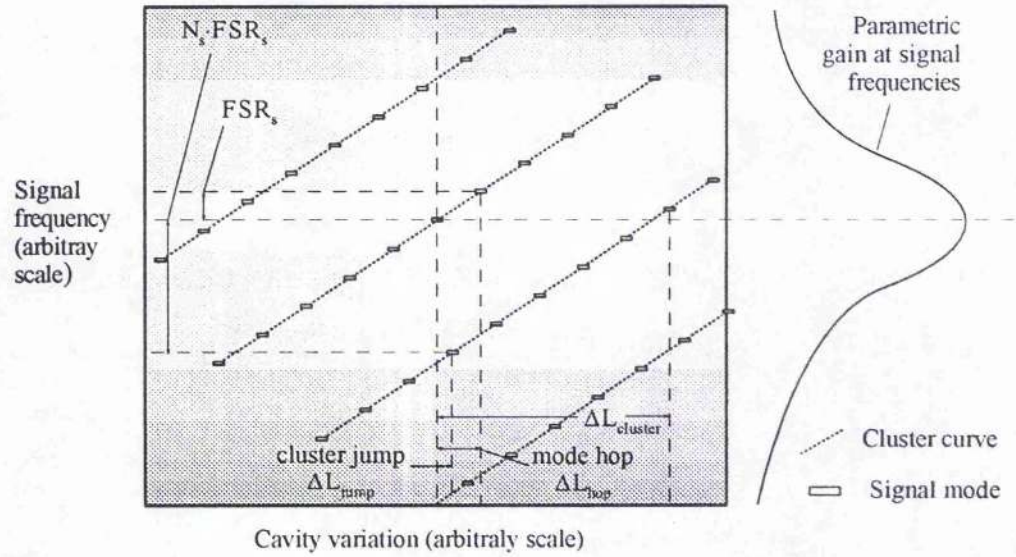

Fig. 5.2.2. Schematic representation of mode hop and cluster jump behaviour via cavity length detuning. The gray scale shows the parametric gain in the phase matching bandwidth. As cavity length detunes, oscillation progresses along cluster curves in a way of mode-hop. Cluster jump occurs when better phase matching exists on an adjacent cluster curve corresponding a large discontinuous frequency change.

C. Stability Conditions

To evaluate the stability requirements on the pump frequency and the cavity length, it is necessary to examine the range over which the available pump power is sufficient to maintain oscillation on a single signal-idler mode-pair. The pump power required to reach threshold depends on the degree to which the resonance conditions for the signal and idler modes are satisfied. It has been derived in terms of classical electromagnetic theory by Eckardt et al. in reference [4]. The parametric threshold $\Gamma^2 L^2$ for doubly-resonant OPO is

$$\Gamma^2 L^2 = \frac{\pi^2}{F_i F_s \cdot \mathrm{sinc}^2(\Delta k \cdot l/2)} \cdot \left[1 + \left(\frac{2 \cdot (\Delta \nu_s + \Delta \nu_i) \cdot F_i F_s}{F_i \cdot \mathrm{FSR}_s + F_s \cdot \mathrm{FSR}_i} \right)^2 \right] \qquad (5.19)$$

where F_s and F_i are the resonator finesses at signal and idler frequencies, $\Delta\nu_s + \Delta\nu_i$ is the sum of signal and idler mode mismatches. Eq. (5.19) has three main terms. Term "$\frac{\pi^2}{F_i F_s}$" describes the reduction in threshold achieved by a doubly resonant OPO. This quantity is equivalent to the multiplied cavity round trip losses of signal and idler $\alpha_i\alpha_s$ in Eq. (1.10). Term "$1/\mathrm{sinc}^2(\Delta k \cdot l/2)$" describes the increase in threshold due to non-perfect phase matching in the nonlinear crystal. Term "$1+\left(\frac{2\cdot(\Delta\nu_s+\Delta\nu_i)F_iF_s}{F_i\cdot \mathrm{FSR}_s + F_s\cdot \mathrm{FSR}_i}\right)^2$" describes the increase in threshold when the signal and idler frequencies do not exactly match the cavity mode frequencies. It is obvious that in the case of perfect phase matching, $\Delta k = 0$, and no frequency mismatch, $\Delta\nu = 0$, Eq. (5.19) reduces to $\Gamma^2 L^2 = \alpha_s\alpha_i$, which is the result obtained directly from the case. As defined by Eq. (5.6), the degree of frequency mismatch of a signal-idler mode pair can be measured as the shift in frequency that is required of either the signal or the idler in order to bring the two resonance into coincidence to satisfy Eq. (5.1). Approximate expressions can be obtained for the maximum fluctuations in the cavity-length or pump-frequency which can be tolerated if the output of the OPO is to be maintained on a single mode-pair. From Fig. 5.2.3, it can be deduced that the allowed maximum detuning, $\Delta\nu$, while maintaining operation on a single mode-pair, is given by

$$\Delta\nu = \Delta\nu_s + \Delta\nu_i \le \frac{\mathrm{FSR}_s}{2F_s} + \frac{\mathrm{FSR}_i}{2F_i} \tag{5.20}$$

where $\frac{\mathrm{FSR}_{s(i)}}{2F_{s(i)}}$ is the half-width at half-maximum of the signal (idler) resonance. We compare Eq. (5.20) to the expression from Eq. (5.19)

$$\Gamma^2 L^2 \propto 1+\left(\frac{2\cdot(\Delta\nu_s+\Delta\nu_i)F_iF_s}{F_i\cdot \mathrm{FSR}_s + F_s\cdot \mathrm{FSR}_i}\right)^2. \tag{5.21}$$

Eq. (5.20) is related to the second term in Eq. (5.21), and corresponds to the detuning in pump frequency or cavity length that doubles the threshold of operation for the particular mode pair. So, comparison can be drawn between various configurations. We take the point where the threshold $\Gamma^2 L^2$ doubles as an indication of the operation range, over which the OPO operates on a single mode-pair. By substituting Eq. (5.7) for the change in signal and idler frequencies, Eq. (5.20) becomes

$$\left|\frac{2}{c}(\Delta L_s \nu_s \mathrm{FSR}_s + \Delta L_i \nu_i \mathrm{FSR}_i)\right| \le \frac{\mathrm{FSR}_s}{2F_s} + \frac{\mathrm{FSR}_i}{2F_i}. \tag{5.22}$$

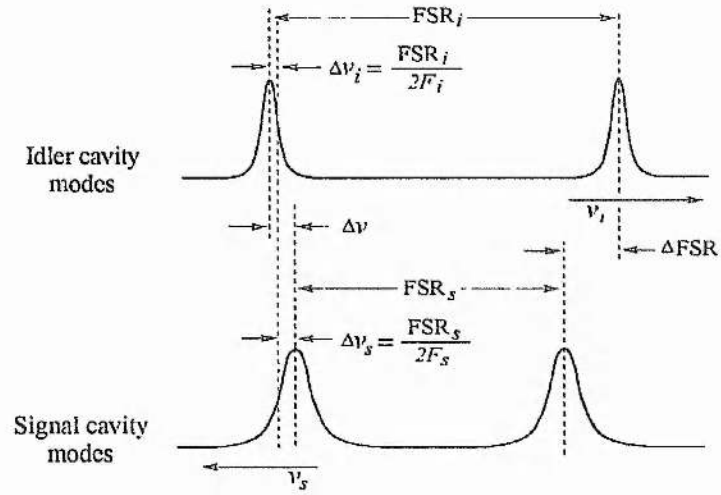

Fig. 5.2.3. Signal-idler resonance diagram, expanded in detail of Fig. 5.5.1, of the requirement for simultaneous resonance of the signal and idler field within DRO. The DRO oscillating frequencies divide the frequency mismatch $\Delta\nu$ into the components $\Delta\nu_S$ and $\Delta\nu_i$. $\mathrm{FSR}_{s(i)}/2F_{s(i)}$ is the half width at half maximum of the signal(idler) resonance.

For a single-cavity OPO within which the signal and idler fields are resonant in the same cavity, the stability in cavity length required to maintain the output on a particular mode-pair is

$$|\Delta L_{stab}| \le \frac{\lambda_p}{4}\left(\frac{1}{F_s} + \frac{1}{F_i}\right). \tag{5.23}$$

Similarly, the pump frequency stability requirement to maintain the output on a particular mode-pair within a single-cavity DRO is

$$\left|\Delta\nu_{p-stab}\right| \le \frac{\mathrm{FSR}}{2}\left(\frac{1}{F_s}+\frac{1}{F_i}\right) \tag{5.24}$$

When the difference in the FSRs of the signal and idler fields is small, for example, in the case of type-I phase-matching near frequency-degeneracy, the cavity-length and the pump-frequency stability requirements [Eq. (5.10) to (5.12)] to prevent a mode-hop become more stringent than the stability requirements to hold a mode-pair above threshold [Eq. (5.23) and (5.24)]. As a result, under detuning of either the cavity-length or the pump-frequency, the output of a type-I near-degenerate OPO will mode-hop between different signal and idler mode-pairs while still remaining above threshold. Under these conditions, the stability requirements needed to maintain the output of the OPO on a single-mode-pair are dictated by Eq. (5.11) and (5.12). Generally, pump source and DRO resonator with conditions like (5.23) and (5.24) do not necessarily guarantee that the resonator can operate on a single mode pair. They only ensure the resonate is "on" which means that there is (or are) mode pair(s) on resonantor. To ensure that a DRO operates on a single mode pair, conditions of mode-hop, cluster-jump, and the resonant stability should be considered together. Among them, the tightest condition is the requirements for pump laser and DRO resonator to operate on single mode pair.

As stated, the above equations have been derived ignoring the influence of dispersion. If the dispersion term is large then it can significantly alter the calculation of ΔFSR which in turn influences the calculated cavity length or pump frequency detuning required to cause a hop to the adjacent mode pair. As an alternative to the approximate analytical expressions, a computer model based on Eq. (5.19) has been developed to calculate the threshold pump power for all possible signal and idler mode-pairs under different combinations of the cavity-length, the pump-frequency, and the phase-matching

temperature [9]. In particular, the pump power threshold can be calculated for each individual mode-pair as a function of the cavity-length detuning.

D. Continuous Frequency Tuning

As analysed, the tuning behaviour of DRO is discrete in nature. However, it is possible to extend the continuous tuning range by synchronously adjusting two or three parameters. Adjusting two parameters simultaneously permits single-mode-pair oscillation condition to be constantly maintained in a fixed phase-matching range. Adjusting three parameters simultaneously permits single-mode-pair condition to be maintained along the phase-matching curve, and tuning is limited only by the extent to which the parameters can be changed. We discuss the continuous tuning of DRO via the adjustments of pump frequency and cavity length.

From Eq. (5.7) and the indication of Fig. 5.2.1, to reach the same frequency mismatch of a signal-idler mode pair, the pump frequency detuning and the cavity length detuning are approximately linearly related. When an equal amount of frequency mismatch is introduced by the two factors,

$$\Delta\nu_p = \Delta\nu_s + \Delta\nu_i \approx \frac{2\Delta L_s \nu_s \mathrm{FSR}_s}{c} + \frac{2\Delta L_i \nu_i \mathrm{FSR}_i}{c} \qquad (5.25)$$

the requirement of constantly maintaining the double resonance condition is achieved. This equation indicates that even when using a somewhat unstable pump source, the double-resonance condition for the signal and idler fields can be maintained by suitable control of the length of the signal and/or idler cavity or vice-versa. Further, the double resonance condition could be maintained by systematic tuning of one variable while keeping the other continuously matched. This is the basis of continuous tunability of DRO. Theoretically, the continuous tuning range is limited only by the pump frequency tuning range. In a single-cavity oscillator, Eq. (5.25) can be reduced to

$$\Delta\nu_p \approx \left(\frac{FSR}{\lambda_p/2}\right)\cdot\Delta L. \tag{5.26}$$

Eq. (5.26) represents a relationship between the perturbation of pump frequency or cavity length and the required correction of the other in order to maintain the simultaneous resonance of the signal and idler fields. Therefore, even within a single cavity OPO, smooth frequency tuning can be obtained by changing the cavity-length while controlling simultaneously the pump-frequency to maintain the single-mode-pair oscillating condition, or vice-versa. In addition, coarse frequency tuning can be obtained by changing the phase matching condition.

5.3 Cavity Design and Considerations

As discussed before, the double resonance condition of DRO leads to a lower threshold than that of SRO. However, it is also the cause of the difficulty of maintaining a high degree of stability, and of the complexity of continuously frequency tuning. In order to achieve stable CW output with continuous tunability from a DRO, important parameters like frequency stability of pump laser, the cavity length control, the quality and phase-matching geometry of nonlinear crystal, and the tuning elements must be considered.

The DRO cavity finesse and free spectral range and the nonlinear crystal phase-matching geometry predominantly determine the stability requirements for pump laser and the DRO cavity for single-axial-mode operation. Consider a single-cavity DRO with output at 1 μm. For a free spectral range of 10 GHz and a finesse of 600, the cold-cavity linewidth is 16.7 MHz. Above threshold the double-resonance condition is satisfied, and the DRO cavity can be thought of as two cavities in series, so that it has a double Lorentzian lineshape. This leads to a DRO cavity linewidth equal to $(2^{1/2}-1)^{1/2}$ times the cold-cavity linewidth, or 11 MHz. The 11 MHz cavity linewidth is equivalent to a 3-dB width of 1 nm in cavity length. In this example the stability requirements can be easily met by the CW DPSSL pump source and current cavity servo techniques.

Various cavity designs have been considered, with high-quality optical materials and stabilised pump laser, for low threshold and widely tunable CW OPO operation. They range from standing wave to ring resonator, from monolithic, semi-monolithic cavity to conventional single-cavity, and dual cavity. These cavity designs have been employed for the CW operation of SRO, DRO, TRO, and even quadruply resonant OPO. However, most of the designs are for CW DROs. The monolithic cavity has excellent mechanical stability. Because the oscillation mode path is enclosed inside a single crystal and the resonant feedback is provided by total-internal-reflection or direct end-surface coating, absorption and scattering losses, both due to multiple surface, are greatly reduced. However, this cavity design requires accurate polishing of the end face and lacks flexibility in changing of mirror coupling coefficients. Moreover, scanning the cavity length can be a problem, and high frequency stability pump laser is usually required. The dual cavity has the advantage of independent control of the two resonant fields to achieved continuous smooth tuning, but the intracavity beam splitter also increases the cavity loss and complexity of alignment. The widely used single-cavity DRO, however, provides the flexibility of changing the cavity free-spectral-range and output coupling coefficient. Although it has less mechanical stability compared with monolithic devices, single-cavity design could be well matched with the pump of free running diode-pumped solid-state lasers.

Frequency tuning of DROs consists of coarse frequency tuning and fine continuous tuning. It may be achieved by varying parameters of phase-matching conditions (angle, temperature or E-field tuning), cavity length (PZT cavity control, temperature, electric-field), and pump frequency. For the application of systematic precision frequency tuning, more than one tuning element is needed to achieve wide-band tuning and continuous smooth tuning. The coarse frequency outputs of the signal and idler frequencies are determined by phase matching range of nonlinear material for a given pump frequency. A wide tuning band can be achieved from the broad phase-matching range of nonlinear crystal. The fine frequency contents of the output depend on the

resonant condition. To achieve continuous smooth tuning, the resonant condition must be constantly maintained. Tuning the pump frequency as an independent tuning element gives the advantage of more freedom of cavity servo control.

In our experiment, the DROs were configured as conventional two mirror cavities shown in Fig. 5.3.1. The output from the frequency doubled Nd:YLF laser (described in Chapter 4) was collimated by a 15-cm focal length lens and subsequently mode-matched into the OPO cavity by lenses of between 10 and 20 cm focal length depending on the DRO configuration. The size of the focus at the centre of the OPO cavity corresponded to a unity confocal parameter at the pump wavelength. Back reflection from the DRO, which otherwise would give rise to laser frequency and intensity instabilities, was suppressed by using a Faraday isolator between the laser and the DRO. Mirrors of 8.5, 10, 15, 20 mm radius of curvature (R.O.C) with reflectivity of 99.9% and 99.5% for the degenerate signal/idler wavelength were used in the experiments. The mirror reflectivity of 55% at the 523 nm resulted in an enhancement of the pump field, reducing the oscillation threshold and providing an indication of alignment and mode-matching of the pump light into the OPO cavity. The cavity mirror spacing was set to give a near optimal unity confocal parameter for signal and idler. These two mirrors were held in *Photon Control* mirror mounts and subsequently attached to a single aluminium block base, while the rear mirror was also mounted on a piezoelectric transducer (PZT) for scanning and stabilising the cavity length.

For the OPO based on KTP, the crystal was 6.0 mm long, and cut for propagation with $\theta = 90^{o}$, $\phi = 37^{o}$ to allow type-II phase-matched degenerate parametric oscillation. Both end faces of the crystal were antireflection coated at pump and degenerate sub-harmonic wavelengths. The crystal was mounted on a galvanometer to allow angle-tuning.

For the OPO based on LBO, the crystal was 20 mm long and cut for propagation parallel to the x-axis to allow degenerate type-I noncritical phase-matching at certain temperature. It was likewise AR-coated at pump and degenerate sub-harmonic

wavelengths. The LBO crystal was mounted inside a temperature-controlled oven to allow the phase-matching temperature to be adjusted.

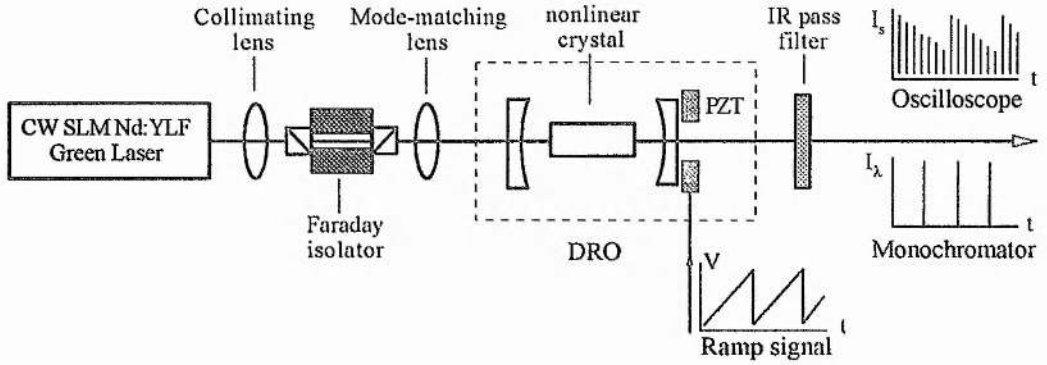

Fig. 5.3.1. Schematic representation of experimental arrangement of the CW doubly resonant OPO based on KTP and LBO.

All optical components were attached to the same aluminium block, so that the cavity length was less susceptible to vibrations. This design also had the flexibility of permitting change to input and output mirrors. Absorption and scattering losses at multiple surfaces were minimised with a low-loss optical coating so that a low threshold could be obtained.

5.4 Experimental Observations in CW Pumped LBO OPO

A. Experimental Conditions

A single cavity DRO based on the noncritical phase-matched LBO described in § 5.3 was used in the experimental observations. The oven/thermocouple combination used to control the temperature of the LBO crystal in this work was calibrated by recording the single-pass frequency doubling efficiency of 1047 nm light from the pump laser, while the temperature was scanned. Optimum frequency doubling was observed for a measured temperature of 166.3 °C. This temperature was in good agreement with the OPO degeneracy operation temperature. When the DRO was configured as a high finesse cavity, the minimum oscillation threshold in LBO was 30 mW at degeneracy, with the

threshold rising slowly as the device was temperature tuned away from degeneracy and hence away from the optimal mirror reflectivity and crystal coating. Throughout the experiments the DRO was pumped at a CW power over 5 times the oscillation threshold. The output of the DRO was tuned by temperature and PZT scan of the cavity. For tuning studies, the cavity length was repetitively scanned when the temperature was stabilised at a few phase-matching temperature set points. A scanning monochromator was used for wavelength measurements. Since the DRO resonator had a weak pump enhancement, the DRO repetitively gave output as the cavity length was swept. The spectra of such output was then analysed by the monochromator. The tuning characteristics of the OPO output were also investigated by monitoring both the transmitted green pump light and the infrared OPO output, while scanning the OPO cavity length over a range of half the pump wavelength. A schematic representation of the experimental set up is shown in Fig. 5.3.1.

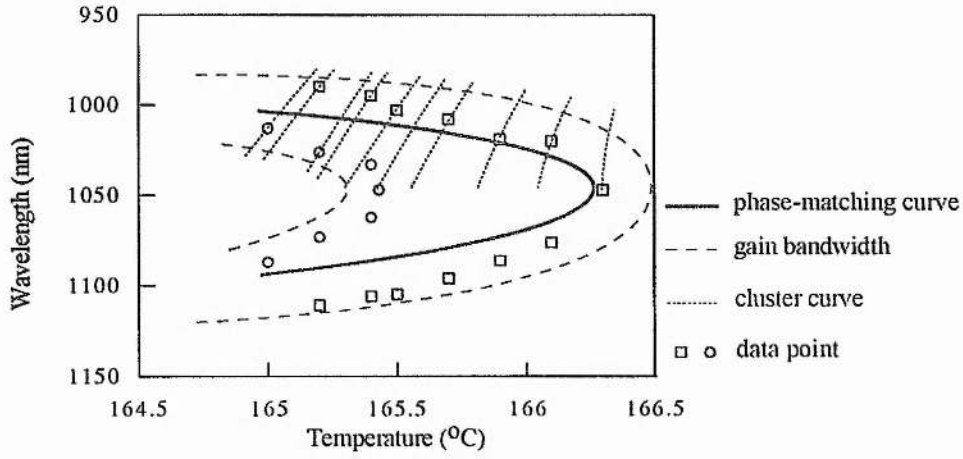

Fig. 5.4.1. The experimentally observed temperature tuning range for the OPO based on LBO, pumped at 523 nm.

The experimentally measured tuning range extended from 990 nm to 1100 nm for a temperature range of 1.3 °C as shown in Fig. 5.4.1. However, the potential tuning range of this crystal orientation, when given appropriate mirrors and crystal coating bandwidths, extends much wider.

B. Axial Mode-Hop Tuning and Cluster Tuning

The tuning of the LBO DRO involves the resonant mode pair jump back and forth between cluster curves as well as mode hops along the cluster curves. By varying the phase-matching temperature, signal-idler wavelengths data were collected. As shown in Fig. 5.4.1, the output wavelengths of around 1.047 μm represent the phase-matching tuning curve at or near degeneracy and also indicate the gain bandwidth and cluster curve. At certain phase-matching temperature, adjacent cluster jump occurs which corresponds to as large as 40 nm discontinuous frequency change in the signal or the idler output. With the cavity length scanning at any fixed temperature, the observed signal spectrum could be varied from 2 nm up to 10 nm depending on the cavity length scanning range, phase-matching condition, and pump power. When the DRO output is monitored on oscilloscope, continuous operation of the OPO is observed in the region of the pump transmission maxima, i.e. when the pump is resonant, as shown in Fig. 5.4.2. However, it is clear from Fig. 5.4.2 that the output is subject to rapid modulation. These modulations result from the OPO output repeatedly hopping to mode pairs with lower oscillation threshold as the pump frequency and the cavity length fluctuate. For a 24 mm cavity length, the mode hops are observed at intervals of a fraction of a nanometer at near degeneracy. Each adjacent mode-hop corresponds to a change in the signal and idler frequencies of one FSR of the DRO cavity, which in this case, is approximately 4.17 GHz. The oscillation does not, however, necessarily hop to an adjacent mode pair since any fluctuation in nanometer range might correspond to several mode hop lengths. Based on the dispersion rate of LBO, the difference in free spectral range of signal idler cavity is in the magnitude of kHz at exact frequency degeneracy. Thus, any kHz pump frequency change or 0.001 nm cavity fluctuation promotes a mode hop. However, such critical requirements on the pump source and DRO itself relax rapidly with the signal and idler wavelength separating from the degeneracy point.

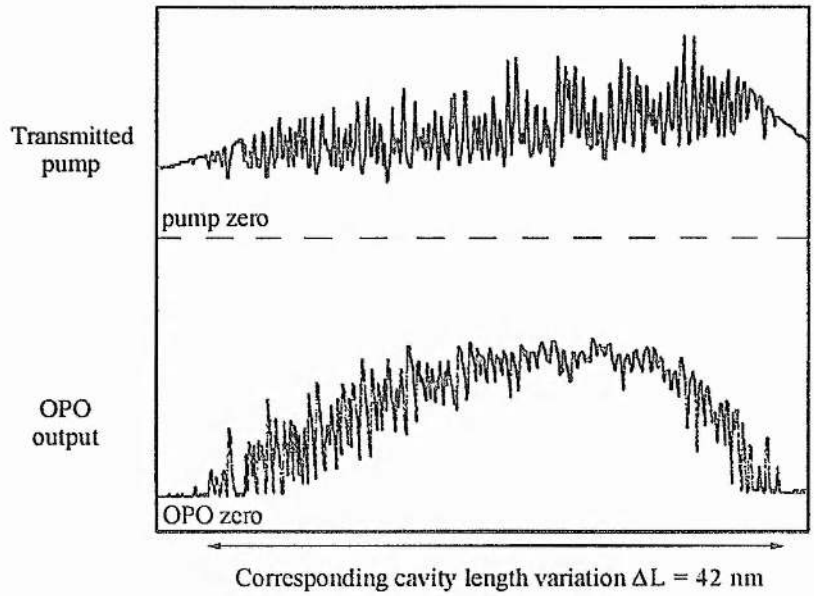

Fig. 5.4.2. The experimentally observed typical mode-hop behaviour for the near degenerate, type-I phase matched OPO based on LBO. Crystal length = 20 mm; Cavity length = 24 mm; Pump wavelength = 523.5 nm.

We have used both the simple expressions developed in § 5.2 and the OPO threshold model to gain some understanding of the mode-hop behaviour in this device. It may be shown, using expressions (5.11), (5.12), (5.23), and (5.24), that, for an OPO cavity of length of 24 nm and with round trip losses of 1% (implying a cavity finesse of 600) the critical values of cavity length and pump frequency stability for mode-hop-free operation and sustained mode pair oscillation are as follows:

$$\Delta L_{hop} = 0.14\text{nm}$$

$$\Delta \nu_{hop} = 2.3\text{MHz}$$

$$\Delta L_{stab} = 0.43\text{nm}$$

$$\Delta \nu_{p-stab} = 7\text{MHz}$$

Here, we have assumed operation away from exact degeneracy, at a signal wavelength of 1027 nm. Fig. 5.4.3 is the calculated mode-hop operation within a single cluster when cavity or pump frequency fluctuation is engaged. The operating condition is the same as described above. The overlap of the threshold minima of successive mode-pair parabolas

ensures that, for most pump rate above threshold, the OPO will remain operational. Therefore, between successive mode-hops, the OPO will be subject to an amplitude modulation which is dependent on the width of the minima curve (as defined by the cavity finesses) and the proximity of these curves (as defined by the free spectral ranges). It is indicated from Fig. 5.4.3 that in order to maintain the operation on a single signal-idler frequency mode-pair, the pump frequency must be stabilised to within 2.3 MHz and the cavity length must be stabilised to within 0.14 nm. Such requirements essentially depend on the mismatch of FSRs and cavity finesses, thus, they change rapidly with the tuning of signal and idler frequencies away from degeneracy.

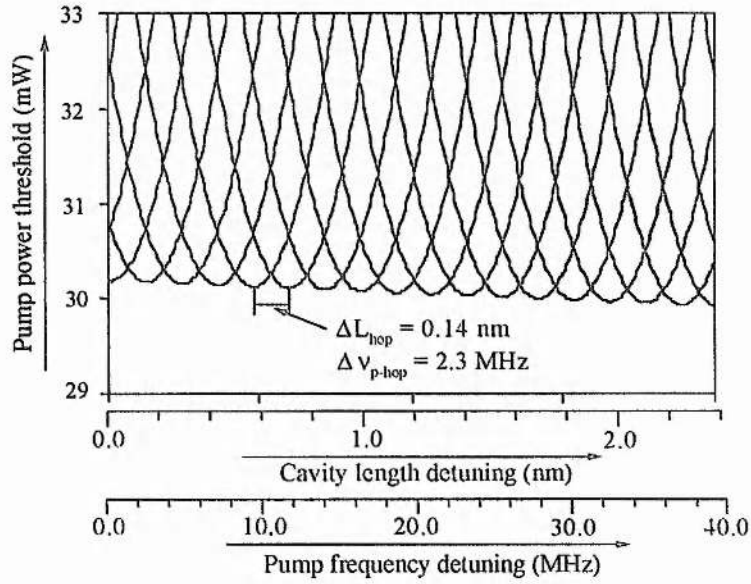

Fig. 5.4.3. Calculated mode-hop operation within a single cluster of a near degenerate, type-I phase-matched OPO based on LBO. Cavity length = 24 mm. Pump wavelength = 523 nm.

Four typical PZT cavity length scanning traces with different output modulations are shown in Fig. 5.4.4, in which the signal-idler frequencies are gradually tuning away from degeneracy operation in (a), (b), (c), (d) cases, respectively. In Fig. 5.4.4 (a), the phase-matching temperature is approximately at degeneracy. Small amplitude modulation is illustrated. At exact degenerate operation cavity length, the direction of the detuning can turn the DRO "on" to the mode-hops (right detuning) or turn the DRO "off" to the none-

resonant zone (left detuning). This is a direct result of the refractive index dispersion of nonlinear material. From the "off" side of illustrated trace, it is also indicated that there is not any cluster jump at degeneracy. As the OPO operation is tuned away from degeneracy, the modulation on the DRO output becomes progressively strong. This is largely due to the fact that the required detuning quantity for mode hop increases rapidly, and further, the cluster jump is likely to join in to modulate the DRO output. Such a modulated OPO output trace due to the mode-hops as well as the cluster jump is typically shown in Fig. 5.4.4 (d).

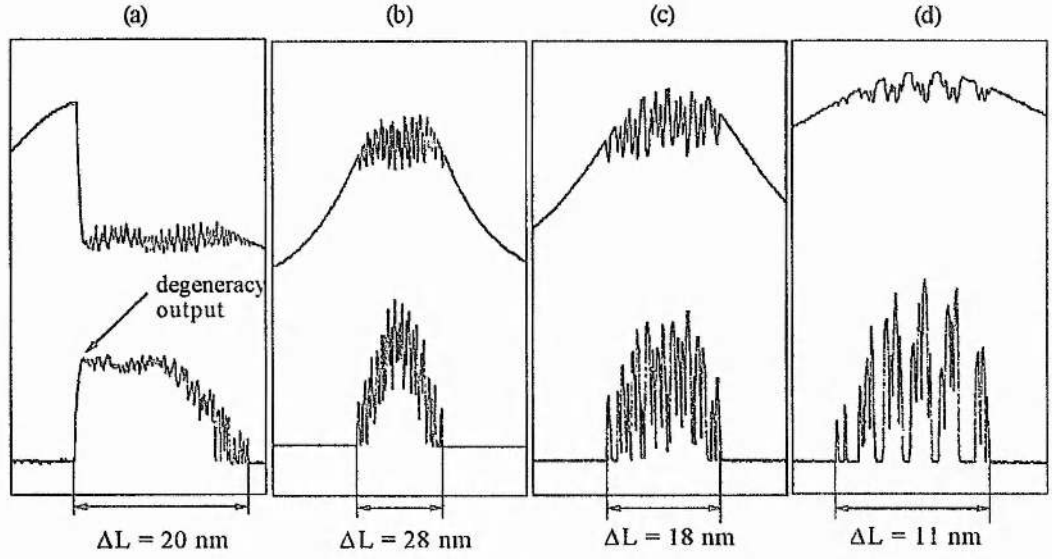

Fig. 5.4.4. The experimentally observed mode-hop and cluster jump behaviour in type-I LBO OPO. The upper trace and the lower trace represent the transmitted pump field and the OPO output for signal and idler frequencies respectively. They are plotted vi the cavity length detuning. The output are gradually away from degeneracy in (a), (b), (c), (d) respectively. ΔL is the corresponding cavity length variation.

When examining with a monochromator, OPO output is observed on two separate widely-spaced wavelength pairs at certain temperatures, as indicated by the tuning curve in Fig. 5.4.1. In fact, if the OPO output is monitored after transmission by the monochromator, groups of output peaks corresponding to a particular wavelength pair may be isolated as in Fig. 5.4.5. These separate wavelength pairs correspond to oscillation on distinct clusters of mode pairs, which are separated in wavelength by up to 40 nm.

The occurrence of cluster-hopping allows for a very small change in cavity length resulting in a very large change in the output wavelength of the device.

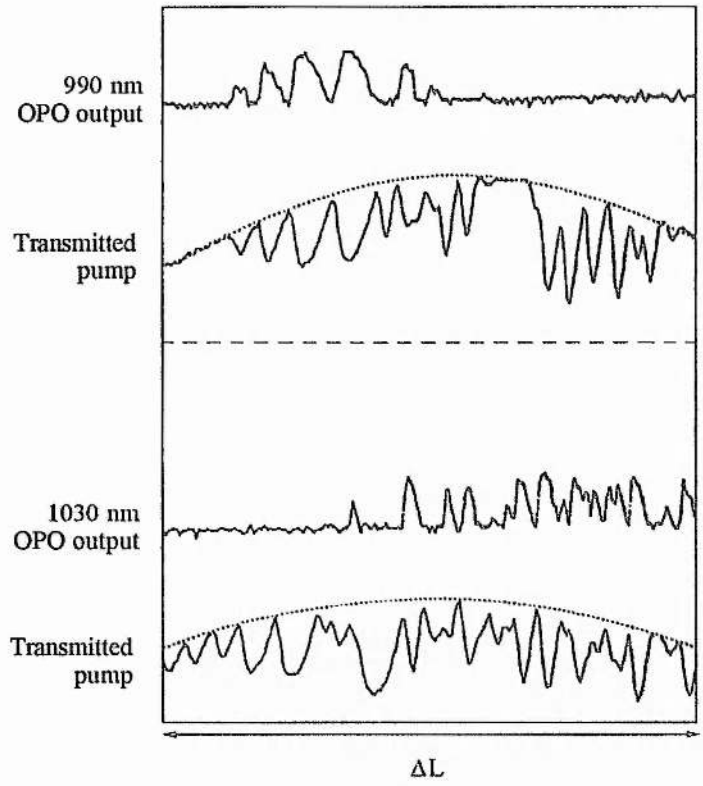

Fig. 5.4.5.

The experimentally observed two-cluster behaviour of a near degenerate, type-I phase matched LBO OPO. The illustrated two clusters are separated by 40 nm in spectrum. As the cavity length is scanned, distinct mode-hops exist along each cluster. Crystal length = 20 mm; Cavity length = 24 mm; Pump wavelength = 523 nm; The corresponding cavity length variation ΔL = 12 nm.

Clearly, the experimental results imply that the device is liable to mode hop well before the variation in cavity length or pump frequency increases the threshold significantly on a particular mode pair. Threshold calculations (Fig. 5.4.3) predict an increase in threshold of less than 1% with cavity length change of a few nanometers. Hence, it may be expected that the device will operate continuously but will be subject to modulation caused by mode hops due to pump and cavity fluctuation. Over a wider range of cavity length change ($\Delta L > \lambda_p/2$), the envelope of minimum threshold follows a different cluster of mode pairs. For a typical cavity scan range of 1 μm, it may thus be expected that the OPO will be subject to both the small frequency variations due to adjacent mode hops and the large frequency variations due to cluster hops.

5.5 Experimental Observations in CW Pumped KTP OPO

A. Experimental Conditions

As described in § 5.3, the KTP DRO was composed of two mirrors and a 3 x 3 x 5.5 (mm) hydrothermally grown KTP crystal. Highly reflective OPO mirrors with radius of curvatures of 8.5, 10, and 20 mm were used in the experiments. The minimum oscillation threshold observed was 6 mW when we used two 8.5 mm R.O.C mirrors and operated the DRO at degeneracy. When the OPO was operated away from frequency degeneracy the oscillation threshold increased. On the other hand, the mismatch of the unity confocal parameter for the pump and the cavity also increased the DRO oscillation threshold. Therefore, the oscillation threshold varied with the experimental conditions. Typically, with $\nu_d \approx 500\text{GHz}$, the DRO had a threshold of 36 mW. The output of the KTP DRO were tuned by crystal angle rotating and the cavity length PZT scan. Angle-tuning of the KTP crystal over an internal angular range of 4° resulted in an OPO tuning range extending from 1020 to 1070 nm (Fig. 5.5.1).

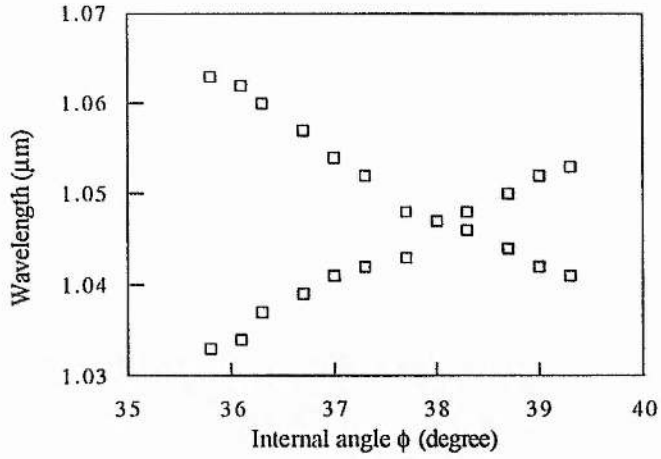

Fig. 5.5.1. The experimentally observed angle tuning range for the OPO based on KTP, pumped at 523 nm

This tuning range was primarily limited by the increasing reflection loss on the crystal surfaces when the cavity mode was away from normal incidence. A tuning range in this plane of around 200 nm should be possible given appropriate crystal coating at this pump

wavelength. Similar arrangement as LBO DRO experiment was set up for the frequency tuning studies.

B. Axial Mode-Hop Tuning and Cluster Tuning

The OPO spectral output as a function of cavity length or pump frequency detuning is observed to be much less random in character than that of the LBO device. Two distinct modes of operation have been observed. Fig. 5.5.2 illustrates the typical mode hop behaviour in type-II DRO when we pump the DRO over 4 ~ 5 times oscillation threshold and scan the cavity length with PZT-attached output mirror.

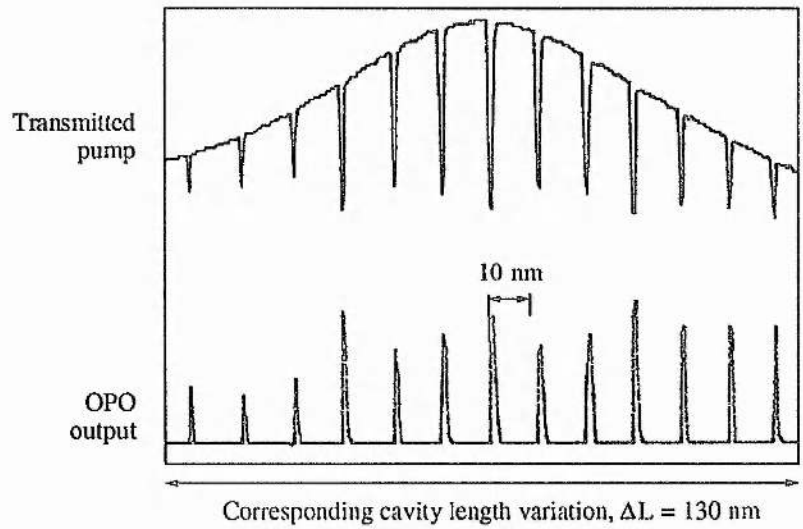

Fig. 5.5.2. PZT cavity-length scanning trace of single-cavity KTP DRO output. Cavity length = 8 mm. Pump power is ~ 5 times the oscillation threshold.

At certain PZT positions, the double-resonance condition is satisfied, and signal and idler outputs are observed over a PZT scanning distance of ~ 1 nm. As shown in the figure, each such output peak occurs at a cavity length variation of 10 nm. These peaks correspond to a series of signal-idler resonance mode pairs within a single cluster. As we detune the DRO cavity length continuously, the mode hop occurs in series that the signal frequency of an adjacent mode pair increases by one free spectral range while the idler frequency decreases by one, or vice versa. However, the phase-matching range (or parametric gain range) is limited at a fixed crystal angle setting. As the cavity length

further detunes, mode hop may come to the edge of parametric gain curve. Therefore, a second cluster may come in from the other edge of the gain curve to continue such mode hops. Fig. 5.5.3 shows a complete picture of mode-hops in different clusters as the cavity length detunes over a range of 420 nm.

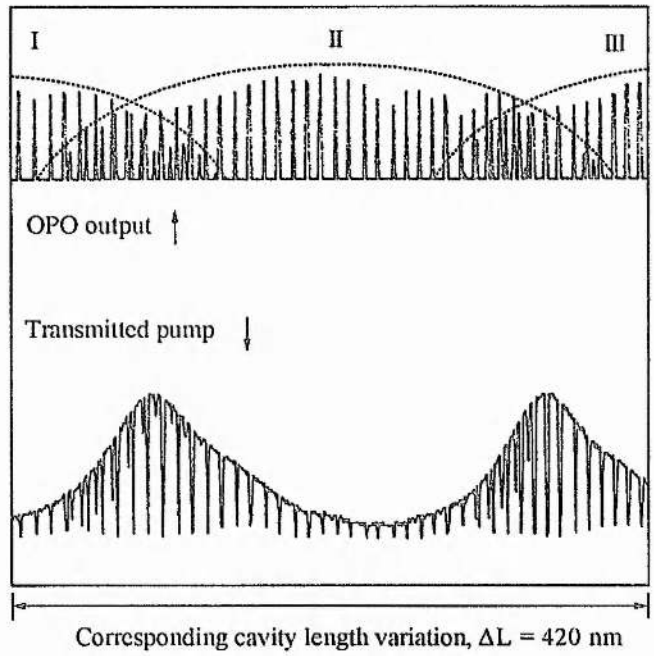

Fig. 5.5.3. The experimentally observed mode-hop and cluster jump behaviour for a near degenerate, type-II phase matched OPO based on KTP. Cavity length = 10 mm. Threshold = 36 mW. Pump power = 240 mW. The dashed envelope lines and I, II, and III represent the different clusters.

The experimental conditions for above operation are as follows: cavity length = 10 mm; OPO mirrors of 8.5 mm and 10 mm R.O.C are used; oscillation threshold = 36 mW; pump power = 240 mW. In the figure, three clusters of mode hops are illustrated as I, II, and III envelope curves, respectively. Single cluster adjacent mode hop corresponds to a discontinuous frequency change of ~ 10 GHz in the output and can be induced by the variation of 10 nm in cavity length or ~ 420 MHz in pump frequency. Adjacent cluster jump corresponds to a discontinuous frequency change of ~ 250 GHz (0.7 nm) in the output and the region at dual cluster operation can be induced by the variation of ~ 2 - 5 nm in cavity length or ~ 100 MHz in pump frequency. The centre wavelength of the

range of these signal modes is resolved as 1046.6 nm which corresponds to the modes under the top of the envelope curves of I, II, or III clusters. In the overlap region of I-II and II-III, the signal modes of the two clusters are at 1045.9 nm and 1047.4 nm, respectively, which is at the edge of the parametric gain curve. In addition, comparing the amplitude of OPO output with pump transmission, efficient OPO conversion does not occur at the pump transmission maxima, on the contrary, they occurs at the non-resonant region where the pump power is estimated to be 4 times the oscillation threshold. Such behaviour is in good agreement with the theoretical prediction [9].

The wavelengths of the two clusters are resolved by using a monochromator. As shown in Fig. 5.5.4 , when the monochromator transmission wavelength is centred at 1047.9 nm with a 0.5 nm transmission width, the main cluster modes are transmitted. However, when the transmission wavelength is centred at 1048.9 nm the second cluster modes can be seen while the main cluster modes are extinct. Therefore, the discontinuous frequency change of mode hop and cluster jump can be measured by comparing the spectral output in a particular cavity length range. Similar experimental conditions as Fig. 5.5.3 measurement are used in Fig. 5.5.4 experiment.

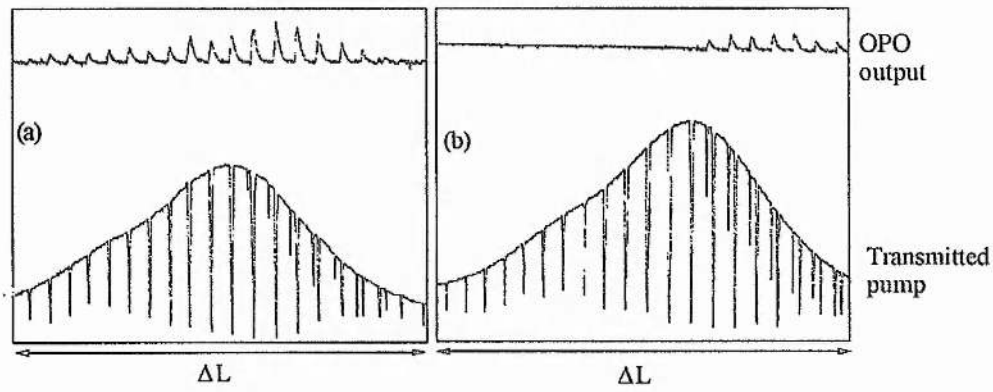

Fig. 5.5.4. The experimentally observed two clusters operation behaviour, measured through monochromator, in a near degenerate, type-II phase matched KTP OPO. The main cluster resolved is at 1047.9 nm in (a), the second cluster is at 1048.9 nm in (b). The corresponding cavity length variation ΔL = 187 nm. Cavity length = 10 mm. Pump power is ~ 5 times the oscillation threshold.

For higher pump power levels, more cluster may come in. Instead of overlapping in a small cavity length variation region, they completely overlap with each other. Fig. 5.5.5 shows a typical pattern of DRO mode tuning behaviour when the device is pumped at ten times the oscillation threshold. While the main group of the peaks remain the same as that in Fig. 5.5.2, a few other groups of peaks have occupied the interval positions periodically. These groups of mode pairs correspond to tuning clusters in the phase-matching range, and have different threshold levels. In fact, for sufficiently high pump power levels, a condition may be approached where output are continuously obtained, although heavily modulated by mode and cluster hops. In above example, each adjacent mode hop corresponds to a discontinuous frequency change of ~ 10 GHz (one FSR) in output while each adjacent cluster jump corresponds to a frequency change of around 1 ~ 2 nm. Thus, more complexity in tuning characteristics and difficulty in single mode pair operation are introduced.

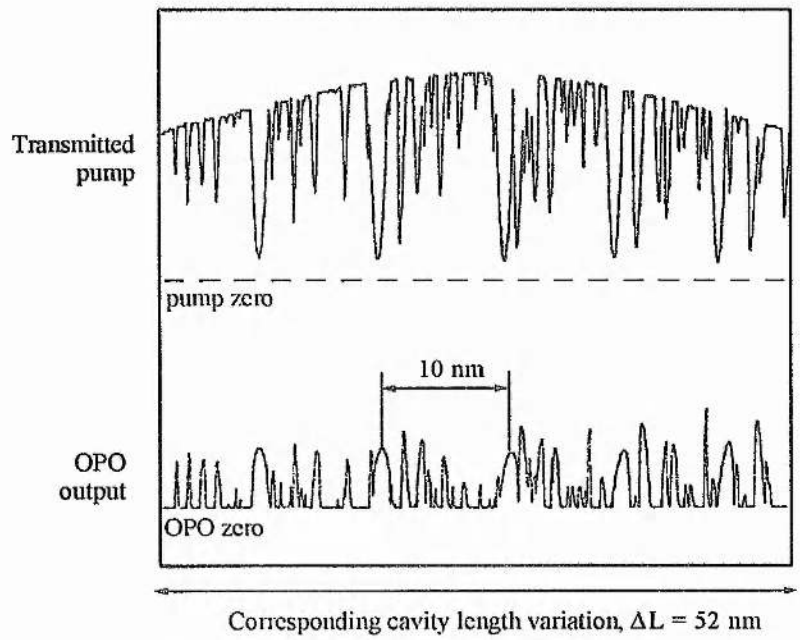

Fig. 5.5.5. The experimentally observed mode-hop and cluster jump behaviour for a near degenerate, type-II phase matched OPO based on KTP. The adjacent mode-hop corresponds to a FSR (11.2 GHz) discontinuous frequency change; the adjacent cluster jump corresponds to about 1 nm discontinuous frequency change. Cavity length = 8 mm. Pump power is ~ 10 times the oscillation thershold.

The tuning behaviour of type-II phase-matched DRO has been analysed in § 5.2 and also can be qualitatively predicted by a computer model developed in St. Andrews [9]. In the case of a type-II phase-matched KTP OPO, where there is a finite difference between the free spectral ranges of the signal and idler at degeneracy, the mode-hop spacings are much larger than that in type-I phase-matching. At the same time, the widths of the threshold-cavity length curves for particular mode pairs are unchanged from those for type-I phase-matching for similar parameter values. On closer examination of the calculated threshold curves (Fig. 5.5.6), it is clear that a relatively small change in the absolute cavity length may result in a large frequency change in the relative minimum thresholds of mode pairs from different clusters.

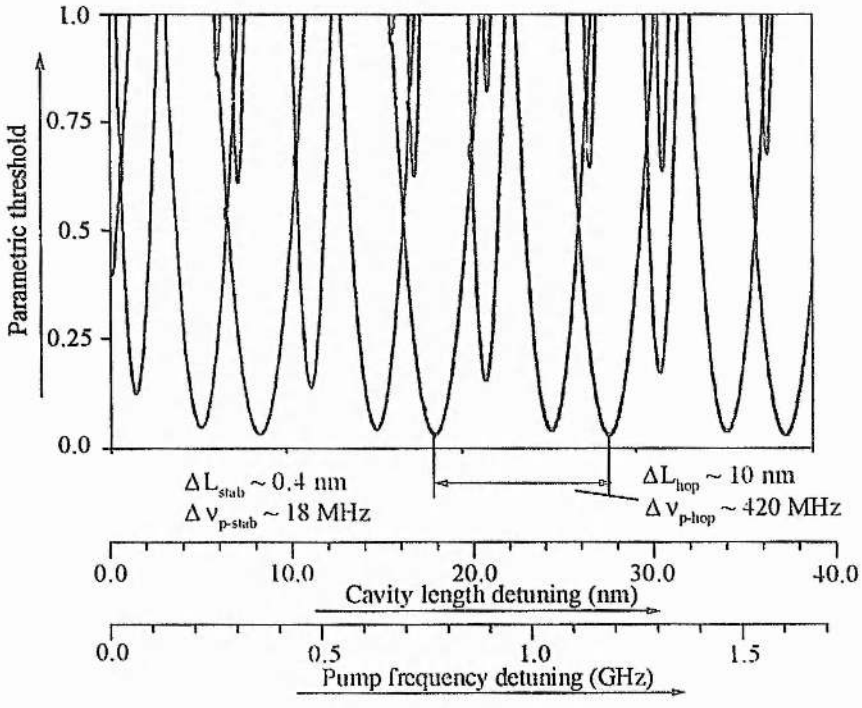

Fig. 5.5.6. Calculated mode-hop and cluster jump threshold of a type-II phase-matched DRO based on KTP at near frequency degeneratcy. Cavity length = 9 mm. Pump wavelength = 523.5 nm

For example, in the overlap region of I-II or II-III of Fig. 5.5.3, the minimum thresholds of adjacent clusters are approximately equal, while a shift of 150 nm to the top of the cluster

curve introduces a factor of 2 between these values. Hence, for different cavity length starting values and pump power levels, it is possible to obtain either systematic discrete tuning through adjacent mode pairs within one cluster, or tuning with hops between various mode pairs in various different clusters. The clusters in KTP at degeneracy have been measured to be spaced by ~ 1 nm, in agreement with theory. The transition between these two regimes of relative cluster threshold has also been recorded during a cavity length scan of around half a pump wavelength. Fig. 5.5.6 shows oscillation on interleaved clusters of mode pairs, with minimum thresholds of the two clusters comparable in value at the centre of the scan.

The stability requirements calculated for a KTP OPO based on a 5.5 mm crystal and a 9 mm length cavity of finesse 600 are as follows:

$$\Delta L_{hop} = 9.8\text{nm}$$
$$\Delta \nu_{p-hop} = 419\text{MHz}$$
$$\Delta L_{stab} = 0.4\text{nm}$$
$$\Delta \nu_{p-stab} = 18\text{MHz}$$

It may be seen that although the single-mode-pair stability requirements are of the same order of magnitude in KTP and LBO given the different cavity lengths, the mode-hop stability limits are two orders of magnitude greater in KTP. Hence, the KTP device is much less prone to frequency shifts due to fluctuation in pump frequency and OPO cavity length, and consequently displays much more regular operating characteristics.

For many applications it is desirable to maintain the output of the OPO to a single signal and idler mode-pair. As discussed previously, slight perturbations in either the pump frequency or the OPO cavity length will usually result in the OPO output hopping to another mode pair and consequently the output frequencies of the signal and idler fields changing discontinuously.

For the OPO based on KTP, the requirement is to maintain a particular mode-pair above threshold and for our experimental configurations this corresponds to a cavity

length stability of ~ 0.4 nm and a pump frequency stability of ~ 18 MHz. However, for the OPO based on LBO, the almost identical free spectral ranges for signal and idler fields results in a system in which the stability requirements to prevent a mode hop are more stringent than that required to maintain a particular mode pair above threshold. The exact detuning required to cause a mode hop depends critically on the mismatch in the free spectral ranges and hence on the exact detuning away from degeneracy. For near degenerate operation the stability requirements are calculated to be as little as 100 pm in cavity length or 800 kHz in pump frequency. Hence, for single mode, near-degenerate operation in a single cavity DRO, it is preferable to use a type-II phase matched geometry.

5.6 Experimental Conditions for Extended Continuous Tuning

In addition to the discrete coarse frequency tuning, continuous tuning of the DRO can be realised by synchronously adjusting two or three parameters. Any permutation of electric field, angle, temperature, pump frequency or cavity length can be used for these three parameters. The relationship between the tuning parameters is determined by the single mode-pair oscillation condition. That is, as one tuning variable change, the change in another parameter must keep the resonator locking on the same single mode-pair oscillation.

For a fixed pump frequency, continuous tuning in single cavity DRO can be obtained by utilising the temperature and electro-optic properties of nonlinear crystal in the tuning processes so as to satisfy the single mode pair condition dynamically. Lee and Wong [6] have temperature tuned a servo-locked DRO continuously over a range of ~ 0.25 GHz. They have also demonstrated E-field tuning over ~ 40 MHz for precision tuning when a particular signal-idler mode pair is locked on resonance. However, due to the small tuning rate of the applied variables, the continuous tuning range is limited below GHz-level. In dual cavity, while the signal and the idler cavity length detune, the change in the

signal frequency can be equal in magnitude, and opposite in sign, to the change in the idler frequency, i.e.

$$\Delta\nu_s = -\Delta\nu_i. \tag{5.27}$$

The relation between ΔL_s and ΔL_i to provide smooth tuning from the dual-cavity oscillator can be expressed as

$$\Delta L_s = -\Delta L_i \cdot \frac{\nu_i \cdot \mathrm{FSR}_i}{\nu_s \cdot \mathrm{FSR}_s}. \tag{5.28}$$

Therefore, in addition to allowing for relaxed stability requirements on the pump frequency and the OPO cavity length, dual-cavity offers the possibility for continuous frequency tuning of the OPO outputs with fixed pump frequency. This may be provided by altering the two cavity lengths simultaneously to satisfy Eq. (5.28). Such type of device, first demonstrated by Colville et al. [8], has been tuned over 0.4 GHz which is limited by the pump enhancement factor. Lee and Wong [10] have also scanned the output frequency over a range of 0.6 GHz by using the same dual cavity approach. Theoretically, the continuous tuning range in dual cavity is only limited by the phase matching range. However, in practice, the dual cavity approach suffers set backs of the complexity of alignment and the difficulty of operating a low loss beam splitter.

The use of pump frequency tuning as an independent tuning element enables the energy conservation condition to be independent of the restriction of signal and idler resonant conditions. The frequency mismatch of the signal and the idler resonant mode can be easily corrected by changing either the cavity length or the pump frequency. Thus, while one variable is continuously tuned, the other variable can be accordingly adjusted to keep the single cavity DRO on single mode pair oscillation condition. Obviously, the tuning range of such an approach is only limited by the tuning variables and the phase-matching range. In addition, this method of tuning has the inherent advantage of simple

device alignment and should be more easily applied to parallel polarisation type-I OPOs since the only variable need to control is the cavity length. Eq. (5.26) describes the relationship between the pump frequency tuning rate and the DRO cavity length tuning rate for maintaining a continuous tuning operation. One parameter can be changed arbitrarily, but the other parameters must be changed in a prescribed manner which is determined by Eq. (5.26). Suppose the DRO starts from oscillation with optimum phase matching and coincidence of the modes that satisfy the conservation-of-energy condition, any change in either of the parameters tends to break the energy conservation condition. However, simultaneously changing both variables in a compensational way will maintain the particular mode pair oscillating over the continuous frequency coverage. The tuning rate of this method is of the same order as the pump or equal to $2\mathrm{FSR}/\lambda_p$ when considering the cavity length detuning. In addition to the two parameter tuning, the third parameter could be introduced to simultaneously keep the optimum phase matching condition. So the limited and fixed phase matching range will be further extended. Therefore, continuous frequency coverage can be obtained with an incremental series of continuous frequency sweeps, and also the continuous tuning device with a wide tunability becomes possible.

From the experimental analysis in § 5.4 and § 5.5, type-II phase-matched single cavity DRO has the advantage of low stability requirements and favourable tuning characteristics. Specifically, considering the KTP DRO described in § 5.5, the preliminary requirement for stable single mode pair operation is the stability requirement on pump frequency and cavity length, i.e. $\Delta\nu_{p-stab} = 18MHz$, $\Delta L_{stab} = 0.4nm$. These requirements can be easily met by the diode-pumped Nd:YLF laser and the three-element DRO cavity. However, when operating the KTP DRO without any servo control on pump frequency or cavity length, the OPO output are slowly varied between "on" and "off" due to the random drifting of the pump frequency and cavity length. Therefore, servo control is necessary for amplitude stable OPO operation.

When the pump frequency is fixed, typical mode pair can resonate in a cavity length detuning range of 0.4 nm (as illustrated in Fig. 5.5.2) with relatively stable amplitude output. A cavity length servo control loop, thus, can be set up to lock the DRO resonating on the particular mode pair. Any change in dis-satisfying the resonant condition induced by the fluctuation or drift of pump frequency will decrease the intensity of the OPO output significantly. Through the photodetector and the servo control loop, cavity length can be synchronously readjusted and the resonant condition can be recovered. When continuously tuning the pump frequency, the cavity length continuously sweeps in an addition to above cavity length servo adjustment. Over the range of pump tuning the signal and the idler frequency could track the pump frequency change as much as $\nu_p/2$, respectively.

The level of DRO pump power not only determines the conversion efficiency but also affects the continuous frequency tuning. From the experimental results in § 5.5, the optimum OPO conversion efficiency has been observed at the pump power of ~ 4 - 5 times oscillating threshold. With the pump power further increasing, the conversion efficiency decreases due to the up-conversion processes. On the other hand, higher pump power also enables the mode in higher lever threshold clusters to oscillate. Since these modes may locate, in cavity length, very near to the oscillating mode-pair of the main cluster, cluster jump can be induced especially in the frequency tuning processes. It is suggested that the optimum pump power should be set and sustained at 4 - 5 times the oscillation threshold level. However, if pump power is increased then the output coupling need to be increased the maintain 4 ~5 times threshold.

5.7 Continuous Tuning of KTP OPO

Based on the previous experimental results, we utilise the single cavity type-II phase matched KTP DRO in stable single mode pair operation and continuous frequency tuning operation. By using a "side of fringe" locking technique to control the length of the OPO cavity, and hence to maintain the doubly resonate condition, we have demonstrated stable

continuous-wave single mode pair operation in the KTP DRO. Further, as the pump laser is continuously tuned over a range of 9 GHz, the PZT servo control enables the cavity length to remain locked to a single signal-idler mode pair resonant, resulting in 4.5 GHz continuous tuning in the signal and the idler output.

Fig. 5.7.1 schematically shows the diagram of the servo-control feedback loop and the three-element DRO resonator. The servo-control feedback method employed is analogous to side-of-fringe locking. The setting of DRO cavity length is detuned slightly off from a power maximum while the infrared output of the OPO is monitored on a fast photodiode. The output of the photodiode is subtracted from a voltage reference to give an error signal. The error signal is integrated to give a control voltage and after amplification is used to drive the piezo-electric transducer to control the cavity length. In this way, the cavity length is adjusted continuously to hold the OPO output power constant, and to maintain the OPO operating on the same single frequency mode-pair. It is obvious that this servo locking technique maintains a constant OPO output amplitude instead of controlling the output frequency. Thus, to achieve frequency stability of the OPO output, one of the output (e.g. the signal frequency) would have to be locked to a stable external etalon or to an external frequency reference. The unity-gain bandwidth of the feedback loop is limited by the response time of the piezoelectric transducer (PZT) to approximately 100's of Hz. The travel range of the PZT element can be as long as 6 μm at 400 V applied DC voltage, which provides tens of GHz tuning capability.

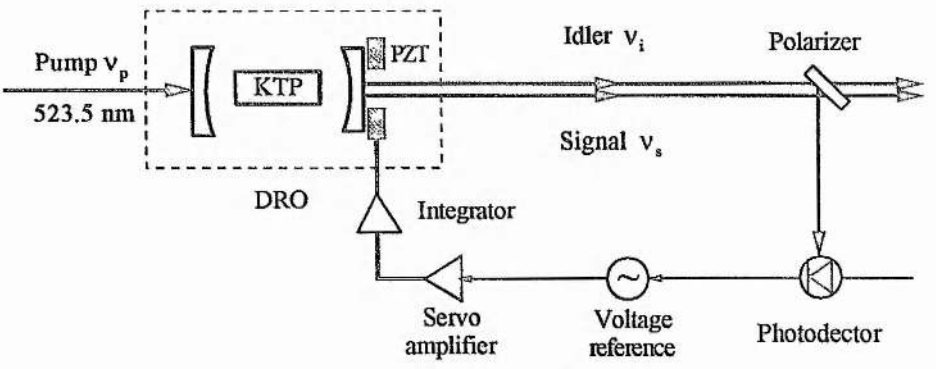

Fig. 5.7.1. Block diagram of the servo-control feedback loop to maintain the DRO cavity resonant on a single signal-idler mode-pair.

CW output of the KTP DRO can be obtained for several tens of seconds at a time under free-running conditions. However, under the servo-locked conditions, stable output without any mode hopping can be maintained for over 1 hr, limited only by accidental perturbations such as pump laser mode hop. The signal-idler output residual intensity noise is ~ 10 - 20% peak-to-peak at mains (100 Hz) related frequency. Due to the narrow unity-gain bandwidth of the feedback loop, environmental acoustic vibrations can also cause a strong intensity modulation. In addition, since the servo loop is an intensity stabilisation feedback loop for low frequencies, the high frequency noise caused by residual frequency jitter of the pump source is also an amplitude noise factor. The locked single cavity has been measured to produce 20 mW of infrared output for 200 mW input pump power when a 0.5% output coupler is used as the OPO front mirror. This can clearly be optimised through improved impedance matching and appropriate output coupling. The spectral output of the OPO has been analysed on a scanning plane-plane interferometer. The single mode pair operation has been confirmed by verying the free spectral range of the interferometer from 10 GHz to 300 GHz. Since any mode hop in the KTP OPO corresponds to a frequency change of ~ 10 GHz, multi-mode-pair operation should be, otherwise, recognised. Fig. 5.7.2 shows an interferometer scan of slightly more than one interferometer free spectral range. The transmission peaks illustrate the single mode-pair operation.

With angle tuning and PZT scanning, together with our intensity servo, we are able to operate the CW DRO stably with discrete but systematic frequency tuning over ~ 10 THz, with the signal frequency change from 286.5 THz to 291.9 THz and the idler frequency change from 286.5 THz to 281.2 THz. Our experimental observations show that the spectral band at a fixed phase-match angle is ~ 200 GHz. Therefore, at each crystal angle setting, it is possible to discontinuously tune the DRO over such a range by PZT scanning at a tuning rate of ~ 10 GHz / 10 nm and with 10 GHz intervals. In addition, by dividing the 4° angle tuning range into ~ 50 divisions, we shall be able to cover the whole 10 THz spectral range in steps of 10 GHz with the OPO output.

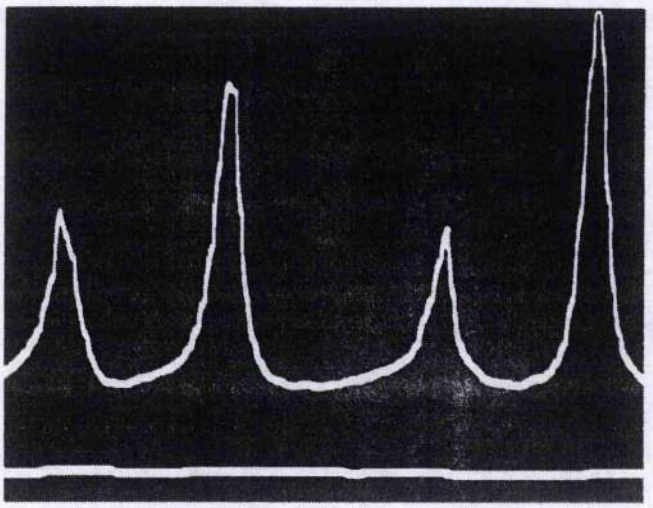

Fig. 5.7.2. The single signal-idler mode pair output from KTP DRO, as monitored on a scanning plane-parallel interferometer of free spectral range of 300 GHz. The higher peaks are idler, the lower peaks are signal. The difference is attributed to the wavelength dependence of interferometer finesse.

As described in Chapter 4, the frequency-doubled diode-pumped Nd:YLF laser can provide up to 1-W single frequency radiation at 573 THz with 9 GHz continuous tunability. This frequency tuning range is achieved by piezo-electric scanning the laser cavity length up to 6 μm (12 times the free spectral range length), and also limited by the potential mode hop for further cavity length tuning. However, extended tuning is possible by simultaneously optimising the gain of the laser mode.

As the pump frequency is continuously tuned over a range of 9 GHz with the PZT voltage manual control, it is observed on a 10 GHz FSR interferometer that the signal and the idler output could track the laser pump tuning by as much as 4.5 GHz without a mode hop. Fig. 5.7.3 shows the OPO output intensity change while we scan the cavity length and thus tune the laser frequency. In practice, such a continuous tuning can occur on any locked mode pair in the phase matching range. Thus, a larger tuning range could be obtained by unlocking to intensity servo first, changing the cavity length of ~ 10 nm to pick up the adjacent mode pair oscillation, and then relocking the intensity servo to repeat the pump frequency scanning. Different tuning behaviour exists between the pump tuning and the mode hop tuning; pump tuning tunes the sum of the signal and

the idler frequencies $\Delta\nu_s + \Delta\nu_i$, so $\Delta\nu_s$ and $\Delta\nu_i$ increase or decrease together; mode hop tuning tunes the signal and the idler resonant modes at a fixed $\Delta\nu_s + \Delta\nu_i$ condition, so that the change of the signal and the idler is equal in amount but opposite in sign.

Table 5.1 summarises the discrete and the continuous frequency tuning parameters employed in the experimental KTP DRO device. Based on the tuning ranges and tuning scales, they can be further categorised into coarse and fine frequency tuning. However, in order to tune the DRO systematically and to achieve a complete coverage on the possible spectral range, it is necessary to incorporate these tuning parameters together in spectral steps. First, from the degeneracy phase matching angle, we can tune the crystal in continuous angle steps where each step corresponds to a 200 GHz spectral width change. In each of these angle steps, a series of mode hops provide another set of low level spectral steps with 10 GHz interval to cover the 200 GHz phase matching spectral width. Finally, by unlocking and relocking the intensity between these mode hop spectral steps, continuous pump tuning can cover the spectral range at and below GHz level.

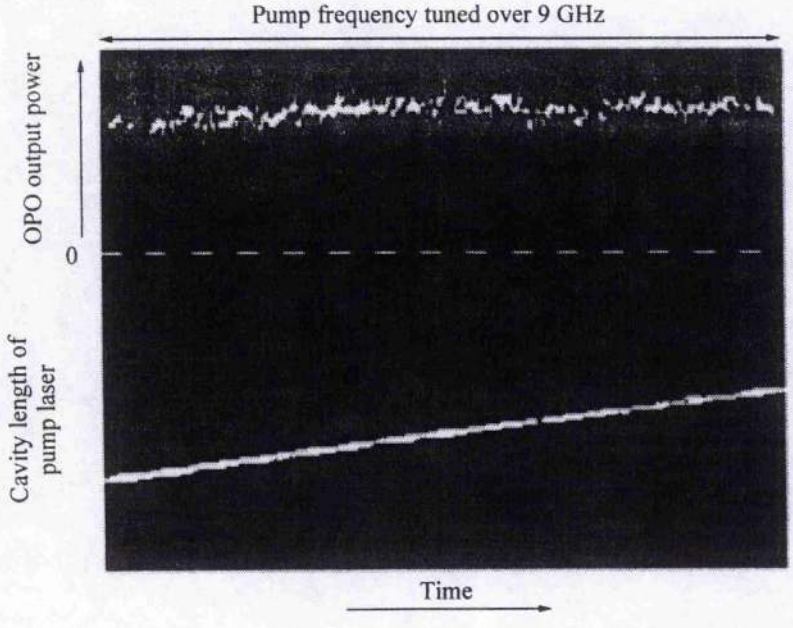

Fig. 5.7.3. Servo-locked OPO output intensity (top trace) measured on a photodiode as the laser is tuned over a range of 9 GHz. The ramp voltage applied to the piezo element of the pump laser is shown in the bottom trace.

Table 5.1. Tuning ranges and coefficients of signal and idler frequencies in KTP DRO

Parameter	*Mode*	*Range*	*Coefficient*
Angle	Discrete	~ 10 THz	2.5 THz / degree
PZT	Discrete	~ 200 GHz	~ 10 GHz / 10 nm
Pump tuning	Continuous	4.5 GHz	1.43 MHz / nm (pump cavity tuning)

5.8 Conclusions

In this chapter, the frequency tuning behaviour of type-I LBO OPO and type-II KTP OPO have been investigated, both theoretically and experimentally. Evidence from both sources indicates that for single mode-pair operation near frequency degeneracy, type-II phase-matching geometry, such as in KTP DRO, is superior to type-I phase-matched geometry in respects of stability requirements and tuning properties. By using side-of-fringe intensity locking technique, we have demonstrated stable CW single mode pair operation in a KTP DRO pumped by a frequency-doubled, diode-pumped Nd:YLF laser. Further, as the pump frequency is continuously tuned over a range of 9 GHz, the signal and the idler output track the pump tuning by as much as 4.5 GHz without a mode hop. Such an all-solid-state device is a promising source for the generation of continuously and widely tunable, highly coherent optical radiation.

An understanding of DRO tuning is important for controlled stable operation. We have derived simple equations to describe the mode hop and cluster jump conditions and to calculate the stability requirements on pump frequency and cavity length for single-mode-pair operation. Good agreement has been observed between the experimental results and theoretical prediction. On the other hand, the results of the calculation will be useful for DRO design optimisation. In single cavity DRO, since independent control of the signal and the idler cavity is restricted, pump frequency tuning is necessary for reaching

any arbitrary frequency in the OPO operating range. As discussed, a systematic tuning with complete continuous tuning coverage could be realised by multiple parameter tuning.

The DRO should find application not only in the generation of stable fixed-frequency radiation but also in generation of stable continuously tunable radiation. Through pump frequency tuning, as demonstrated, high-resolution DRO tuning will be possible over incremental frequency ranges for spectroscopy applications.

References

[1] R. Graham and H. Haken, "The quantum-fluctuations of the optical parametric oscillator. I", *Z. Phys.*, vol. 210, pp. 276-302, 1968.

[2] C. D. Nabors, S. T. Yang, T. Day, and R. L. Byer, "Coherence properties of a doubly resonant monolithic optical parametric oscillator", *J. Opt. Soc. Am. B*, vol. 7, pp. 815-820, 1991.

[3] J. Falk, "Instabilities in the doubly resonant parametric oscillator: a theoretical analysis", *IEEE. J. Quant. Eletron.* vol. 7, pp. 230-25, 1971.

[4] R. C. Eckardt, C. D. Nabors, W. J. Kozlovsky, and R. L. Byer, "Optical parametric oscillator frequency tuning and control", *J. Opt. Soc. Am. B*, vol. 8, pp. 646-667, 1991.

[5] T. Debuisschert, A. Sizmann, E. Ciacobino, and C. Fabre, "Type-II continuous-wave optical parametric oscillators: oscillation and frequency-tuning characteristics", *J. Opt. Soc. Am. B*, vol. 10, pp. 1668-1680, 1993.

[6] D. Lee and N. C. Wong, "Stabilisation and tuning of doubly resonant optical parametric oscillator", *J. Opt. Soc. Am. B*, vol. 10, pp. 1659-1667, 1993.

[7] C. D. Nabors, R. C. Eckrdt, W. J. Kozlovsky, and R. L. Byer, "Efficient, single-axial-mode operation of a monolithic MgO:$LiNbO_3$ optical parametric oscillator", Opt. Lett., vol. 14, pp. 1134-1136, 1989.

[8] F. G. Colville, M. J. Padgett, and M. H. Dunn, "Continuous-wave, dual-cavity, doubly-resonant optical parametric oscillator", *App. Phys. Lett.*, vol. 64, pp. 1490-1492, 1994.

[9] M. J. Padgett, F. G. Colville, and M. H. Dunn, "Mode selection in doubly resonant optical parametric oscillators", *IEEE J. Quant. Electron.*, vol. 30, 1994.

[10] D. Lee and N. C. Wong, "Tuning characteristics of a CW dual-cavity KTP optical parametric oscillator", *CLEO'95* paper CWE5

Chapter 6

GENERAL CONCLUSIONS

The practical realisation of diode-pumped solid-state lasers represents a major technological advance in the evolution of lasers, enabling the development of very efficient, compact devices with greatly improved reliability. The advantages of diode-pumped lasers are also exhibited in the special properties which open up new applications that have been previously impossible or impractical with conventional laser sources. One such application is in the efficient transfer of the highly coherent properties of the laser output into a wide range of the optical spectrum via nonlinear frequency conversion techniques such as second harmonic generation and optical parametric oscillation. Since such nonlinear frequency conversion processes require light sources with high spectral brightness and high stability, and these can be efficiently provided by diode-pumped lasers, hence efficient frequency conversion can be attained.

In this thesis, the design, construction and development of a diode-pumped Nd:YLF laser and its frequency conversion has been presented. The work has ranged from the initial investigation of the characteristics of the diode-end-pumping configuration, through all the steps of efficient cavity design, to the construction of an intracavity-frequency-doubled single-frequency green laser. By using the green laser as a pump source, the performance of continuous-wave single-cavity doubly resonant OPOs have been studied. Continuous smooth tuning of a signal-idler mode-pair over as much as 4.5 GHz in the 900 nm - 1100 nm output wavelength range has been demonstrated in a KTP OPO.

The folded cavity design has proved to be an optimum design where a few factors have been compromised in achieving efficient intracavity second harmonic generation. Firstly, it produces a large elliptical cross-section cavity mode in the gain medium which can be made to overlap efficiently with the cross-section of the diode laser pump profile;

and at the other end of the cavity, it produces a tightly focused circular mode waist suitable for the doubling crystal. Hence, the laser can efficiently extracts the available pump energy into a green laser output. Secondly, the influence on the laser performance of the thermal distortion in the gain medium is greatly reduced by this cavity design. In addition, by slightly translating the cavity mirrors, the thermal lensing induced cavity mode change can be compensated. Finally, the arrangement of the two dichroic mirrors used in the cavity can effectively combine the SHG outputs generated in two directions into a single uni-directional output. One disadvantage of the laser design, however, is that the diode pump power is still not fully utilised because of the poor spatial mode overlap between the pump and the laser. Recent developments in diode array coupling techniques for end-pumping such as microlens array coupling, waveguide coupling and efficient fibre coupling have made it possible for diode arrays to provide smaller and circular pump beam profiles. With the improvement of the pump beam by these techniques in future work, higher laser efficiency is expected.

Large amplitude fluctuations in the SHG output are often associated with the multimode operation of intracavity-frequency-doubled lasers. A direct method of eliminating the noise is to use a single-frequency laser. In this work the single-frequency operation of the frequency-doubled Nd:YLF laser is achieved by using a novel intracavity birefringent filter formed by a Brewster plate and the KTP doubling crystal. The birefringent filter plays an important role in the doubling process. Being a doubling crystal, KTP can efficiently convert the fundamental wave into the second harmonic wave hence acting as a nonlinear output coupler. On the other hand, since type-II phase-matching geometry is used, the birefringence of the KTP crystal also introduces a phase shift between the extraordinary and ordinary ray components for each oscillating mode. In section § 4.4, the polarisation-wavelength dependence behaviour was analysed. As a result, the combination of the Brewster plate and the KTP performs the function of a longitudinal-mode selector. The single-frequency operation of the laser was found to be crucially dependent on the performance of this birefringent filter, while the intracavity

uncoated etalon served to reinforce the SLM operation. However, the birefringence of the KTP crystal is temperature sensitive. Hence any temperature perturbation or small refractive index change in KTP may cause mode hopping or unstable operation of the laser which is accompanied with the dramatic output power change. The SHG output power drift and the mode hop which have been encountered in the experiment are believed to be a consequence of the perturbations of the KTP crystal birefringence. By stabilising the temperature of the KTP crystal and the cavity, the laser output stability has greatly improved. However, in order to achieve good long-term stable operation, further cavity parameter control are required. The birefringent mode selection technique can be enhanced by using a temperature stabilised high quality KTP crystal and a multiple Brewster plate. In addition, electro-optic control of the KTP crystal which leads to a modification of the birefringence properties can also be used in a feedback servo-loop to stabilise the laser operation. These improvements will the key factors that need to be addressed for reliable long-term laser performance and further power scaling of such devices.

The doubly resonant single cavity optical parametric oscillator was used to frequency down-convert the continuous-wave green radiation into tunable infrared radiation. Experimental investigations of the frequency tuning behaviour and stability requirements for both type-I and type-II geometry doubly resonant OPOs have been carried out. Since the type-II KTP DRO exhibits significant advantage over type-I LBO OPO in the respects of tuning and stability for single-mode-pair operation, it was utilised in a stable near-degenerate OPO operation. By using the side-of-fringe intensity locking technique, we have demonstrated stable CW single-mode-pair operation. Further, as the pump frequency was continuously tuned over a range of 9 GHz, the signal and idler output were observed to track the pump tuning by as much as 4.5 GHz without mode hopping. Systematic frequency tuning in the KTP DRO requires to be examined in detail in future experiments. Such multiple parameter frequency tuning can combine the wide range discrete tuning and the precision continuous tuning in the same device, and lead to a broadly tunable, highly stable, DRO-based CW radiation source.

Theoretical modelling and analyses of the end-pumped Nd:YLF laser and its intracavity frequency-doubling have been carried out in the thesis. The rate equation approach in section § 2.9 is generally applicable to four-level laser systems where the spatial variation of both the pump beam and the cavity mode are considered. The threshold and the slope efficiency of such system have been derived. In the analysis, it has been shown that in the homogenous gain medium with a strong spatial hole burning effect and energy diffusion, the expected longitudinal modes are separated with a few cavity mode spacing which rely on the spatial distribution of the laser gain. This prediction has been confirmed in the experiments in chapter 3. The efficiency analysis of intracavity SHG has been given in § 4.3. Two important factors for the design of efficient CW intracavity SHG are to minimise the internal loss and to optimise the nonlinear coupling. The short- and long-term instability problems encountered in the intracavity frequency-doubling process have also been discussed in detail. It is generally believed that the green noise problem is the direct result of the efficient sum-frequency coupling of cavity modes in the laser operation. The rate equation approximation of the frequency-doubled laser in section § 4.4 analysed the origin of this instability. These equations also reveal the conditions for the stable operation. In addition to the short-term noise, the conditions of maintaining long-term stability have also been discussed. A Jones-Vector analysis of the Nd:YLF laser cavity in § 4.4 was used to illustrate the mode selection mechanism of the birefringent filter. However, the calculation of the multimode oscillation threshold needs to be completed in future modelling.

The theoretical investigations on the tuning behaviour of type-I and type-II doubly resonant OPO and the stability requirements for single mode-pair operation have been presented in section § 5.2. By analysing type-I and type-II phase matched DRO, we have illustrated both the mode-hop and cluster-hop behaviour of the DRO output. From the analysis it has been concluded that type-II geometries are superior when compared to type-I in the respect of its stability requirements and tuning properties for near-degenerate operation. For single-mode-pair output, a pump frequency stability of a few

MHz and sub-nanometer control of cavity length are required for type-II geometry while much high requirements are imposed on the type-I. Such analysis has given a basic understanding of the tuning behaviour in doubly resonant OPOs and provided a theoretical criteria for the design of the continuously tunable doubly resonant OPO device with a single-mode-pair output.

The experimental work in this thesis has demonstrated that the combination of diode-pumped solid-state lasers and nonlinear frequency conversion techniques represent an efficient class of all-solid-state devices. These devices can efficiently convert the laser frequency into other discrete frequencies or tunable output while maintaining frequency stability and narrow linewidth. The compactness, longevity and other desirable properties of diode-pumped lasers have been shown to be inherent in these devices. The wide tuning range and continuous tunability stand as a major advantage compared to conventional lasers emitting at discrete wavelengths. Following on from the experiment observations in this thesis, a few investigations and improvements can be highlighted fro further research. (1) The laser efficiency can be greatly improved by changing the end-pump coupling configuration into microlens array coupling geometry. (2) The pump drift problem and the frequency instability need to be further investigated. (3) Power scaling of the single-frequency green laser can be carried out if the effect of the birefringent filter is further improved. (4) The continuous tuning range of the green laser can be extended through multiple parameter tuning. (5) Frequency jitter and long-term drift need to be reduced. (6) By using different angle-cut nonlinear crystals the wavelength diversity of the OPO can be further extended. (7) Continuous systematic tuning of the KTP OPO may cover the full phase matching range if multiple parameter tuning in the OPO and a widely continuous tunable laser are utilised.

The availability of these continuous-wave all-solid-state devices will find applications in many research, scientific and industrial areas such as coherent optical communications, LIDAR remote sensing, optical frequency standard, optical storage, and medical uses. To date the diode-pumped Nd:YLF laser has been used in an optical

computer system [1]. The 1-W single-frequency green laser is being developed and commercialised by Edinburgh Instruments Ltd for various scientific and industrial uses such as optical interferometry in car designs [2]. The continuous tunable KTP OPO will also find many applications in high resolution spectroscopy.

References

[1] Kathy Kincade, "Scotland's investment in optoelectrons pays off", *Laser Focus World*, pp. 50-51, March, 1995.

[2] J. Jones, J. Valera, C. Bockberry, and D. Tower, "Laser measure up for the car industry", *Physics World*, pp. 33-38, May, 1995.

Appendix I

Laser Diode-Pumped Intracavity Frequency-Doubled Nd:YLF Laser

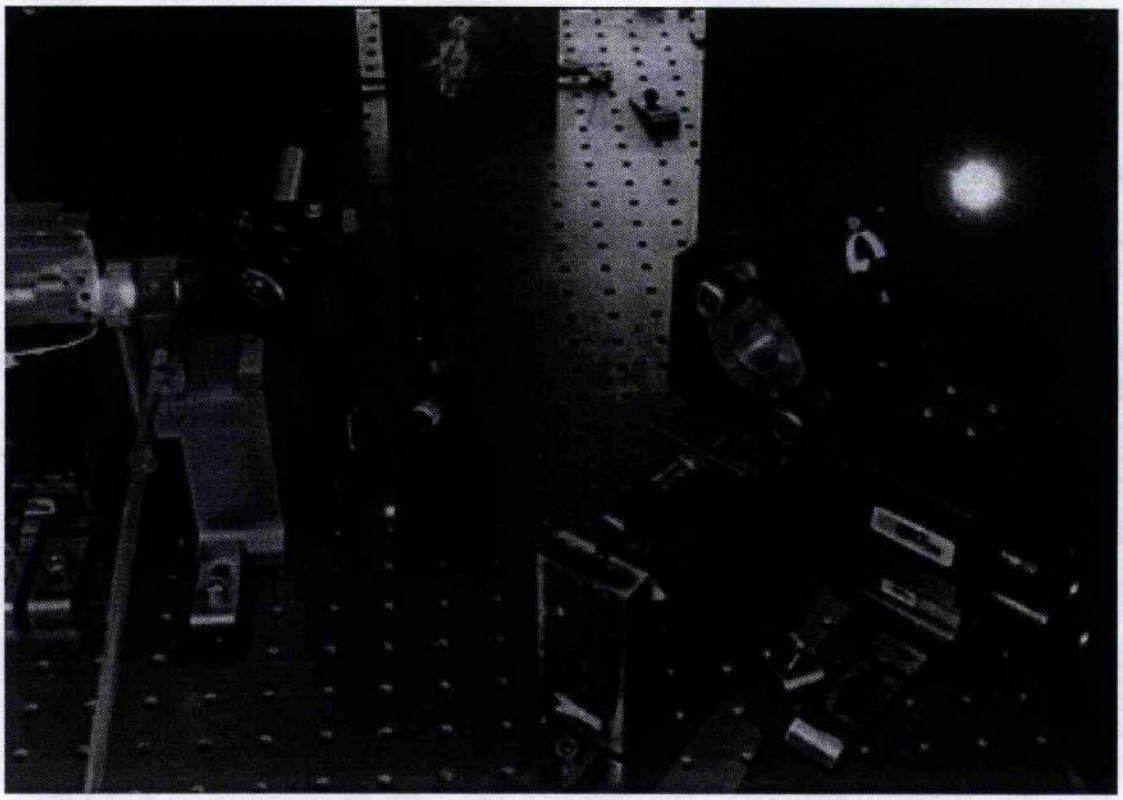

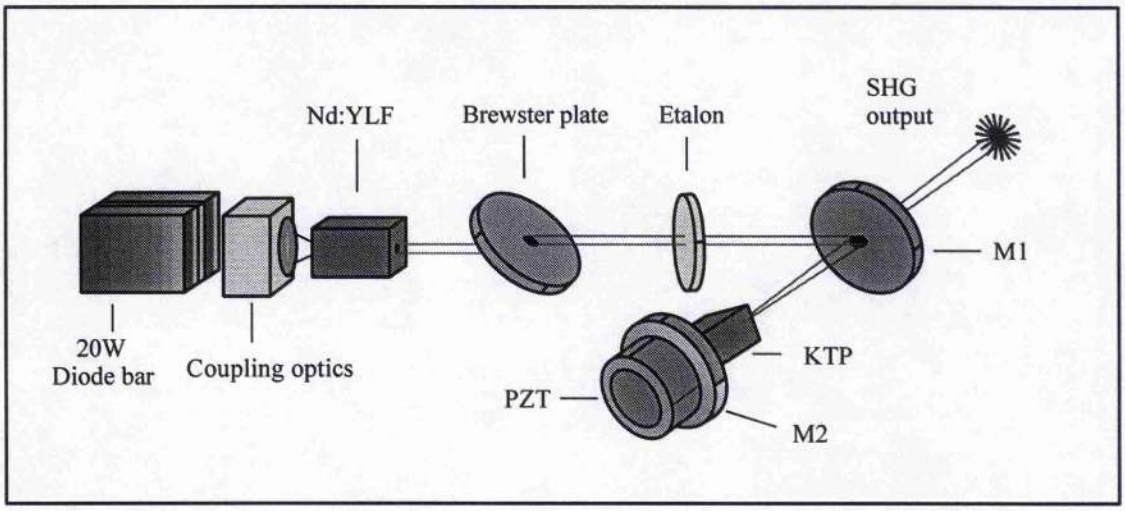

Appendix II All-Solid-State Continuous-Wave KTP Optical Parametric Oscillator

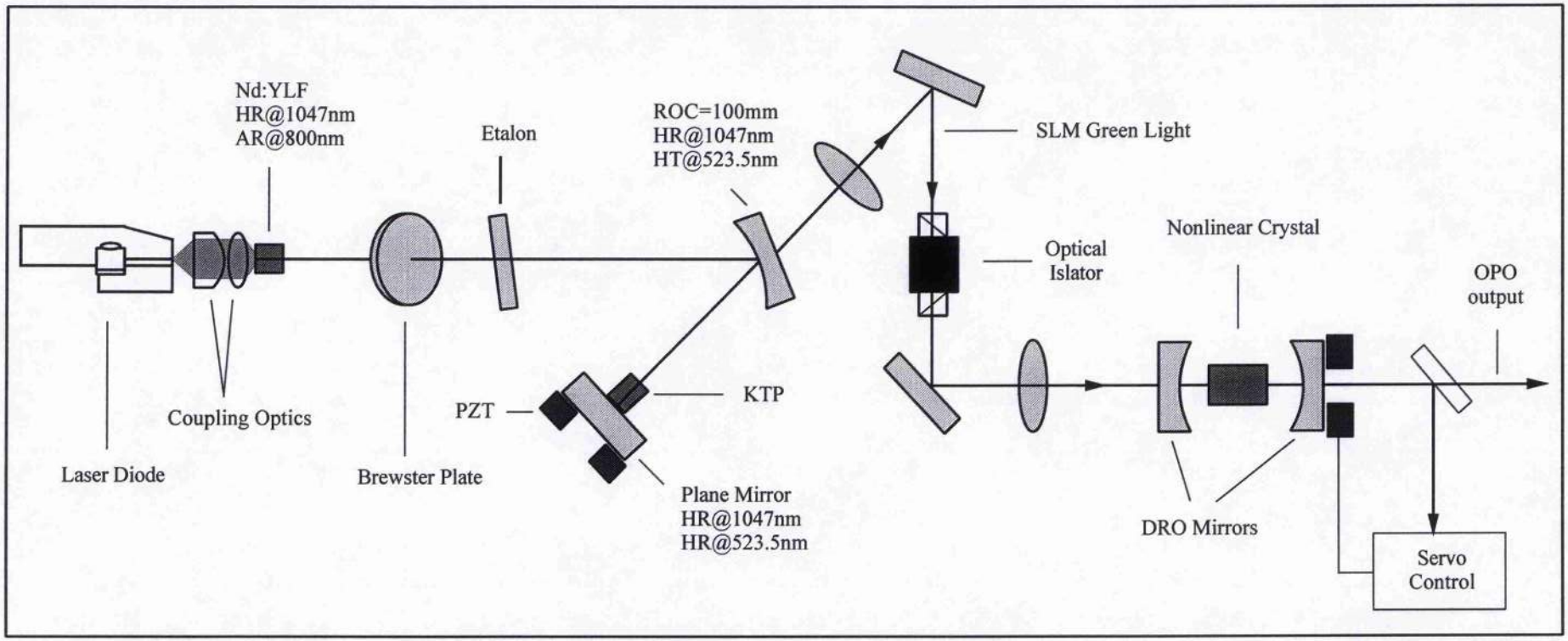

Appendix III Publications and Conference Proceedings

1. "Continuous-wave parametric oscillation in lithium triborate", F. G. Colville, A. J. Henderson, M. J. Padgett, J. Zhang and M. H. Dunn, *Opt. Lett.*, Vol. 18, 205 (1993).

2. "Continuous-wave parametric oscillator pumped in the ultraviolet", F. G. Colville, A. J. Henderson, M. J. Padgett, J. Zhang and M. H. Dunn, *Opt. Lett.*, Vol. 18, 1065 (1993).

3. "Continuous-wave parametric oscillator pumped in the ultraviolet", F. G. Colville, A. J. Henderson, M. J. Padgett, J. Zhang and M. H. Dunn, in Conference on Laser and Electro-Optics, OSA 1993 *Tech. Digest Series*, paper CPD15.

4. "Continuous-wave lithium triborate optical parametric oscillators", F. G. Colville, A. J. Henderson, M. J. Padgett, J. Zhang and M. H. Dunn, *Technical Digest of Papers,* at the Eleventh UK National Quantum Electron. Conf., paper 4.

5. "All-solid-state continuous wave optical parametric oscillators in KTP and LBO", A. J. Henderson, J. Zhang, M. H. Dunn, in Conference on Laser and Electro-Optics, OSA 1994 *Tech. Digest Series*, paper CTuK18.

6. "Doubly resonant optical parametric oscillators: tuning behaviour and stability requirements", A. J. Henderson, M. J. Padgett, J. Zhang, F. G. Colville, and M. H. Dunn, *Opt. Commun.*, Vol. 119, pp. 256-264, (1995).

7. "Multigigahertz tuning of single-frequency output from a CW single cavity optical parametric oscillator", A. J. Henderson, M. J. Padgett, J. Zhang, W. Sibbett, and M. H. Dunn, in Conference on Laser and Electro-Optics, OSA 1995 *Tech. Digest Series,* paper CFG4.

8. "Continuous frequency tuning of a CW optical parametric oscillator through tuning of its pump source", A. J. Henderson, M. J. Padgett, J. Zhang, W. Sibbett, and M. H. Dunn, *Opt. Lett.*, Vol. 20, 1029 (1995).